Ground-based Remote Sensing of Aerosol Properties Using the Emission FTS in Ny-Ålesund, Spitsbergen (78°N)

Dissertation

Zur Erlangung des akademischen Grades
Doktor der Naturwissenschaften (Dr. rer. nat.)
im
Fachbereich Physik und Elektrotechnik
der
Universität Bremen

Denghui Ji

Eingereicht am: 03. September 2024
Datum des Kolloquiums: 04.December 2024

1. Gutachter: Prof. Dr. Justus Notholt
2. Gutachter: Prof. Dr. Hartmut Bösch

Abstract

Arctic amplification, the rapid warming of the Arctic compared to the global average, remains partially understood. Key processes include temperature feedback, surface albedo feedback, and cloud and water vapor feedback, with aerosols playing a critical role. Since 2019, a Fourier-Transform Infrared Spectrometer (FTS) at the AWIPEV research base in Ny-Ålesund, Spitsbergen, has been used to measure aerosol components. An algorithm based on the Line-by-Line Radiative Transfer Model and DIScrete Ordinate Radiative Transfer model (LBLDIS) was developed for retrieving aerosol composition.

In order to show this measurement technique in details, a case study for an aerosol-only case is presented with data from the 10^{th} of June 2020. In the aerosol-only case, the retrieval results show that sulfate ($\tau_{900cm^{-1}}$=0.007 $\pm$ 0.0027) is the dominant aerosol during the whole day, followed by dust ($\tau_{900cm^{-1}}$=0.0039 $\pm$ 0.0029) and black carbon ($\tau_{900cm^{-1}}$=0.0017 $\pm$ 0.0007). Sea salt ($\tau_{900cm^{-1}}$=0.0012 $\pm$ 0.0002), which has the weakest emission ability in the infrared waveband, shows the lowest AOD value. Such proportions of sulfate, dust and BC also show good agreement with MERRA-2 reanalysis data. Additionally, the comparison with a sun-photometer (AERONET) shows the daily variation of aerosol AOD retrieved from FTS to be similar with that of the sun-photometer. Based on this retrieval method, long time period observations dataset using FTS is retrieved and presented in this study.

Based on the observed data, the infrared radiation effects of different aerosol composition are analyzed. The results show that the hygroscopic aerosols, such as sea salt and sulfate, have a warming effect in the Arctic during winter. These aerosols absorb atmospheric water vapor, leading to wet growth, increased size, and enhanced longwave downward radiation emission, defined as the Aerosol Infrared Radiation Effect (ARE). Observations of aerosols, especially their composition, are challenging during the Arctic winter. We use an emission Fourier Transform Spectrometer to measure aerosol composition. Observations show that the ARE of dry aerosols is limited to about 1.45 ± 2.00 Wm^{-2}. Wet growth significantly increases the ARE of aerosols. During winter, at relative humidity levels between 60% and 80%, wet aerosols exhibit the ARE approximately 10 times greater than dry aerosols. When relative humidity exceeds 80%, the effect can be up to 50 times higher (30 - 100 Wm^{-2}). Sea salt aerosols in Ny-Ålesund demonstrate high effect values, while non-hygroscopic aerosols like black carbon and dust show consistently low values. Reanalysis data indicates increased water vapor and sea salt aerosol optical depth in Ny-Ålesund after 2000, correlating with significant positive temperature anomalies in this area. Besides, wet aerosols can remain activated even in dry environments, continuously contributing high effects, thereby expanding the area affected by aerosol-induced warming. This warming effect may exacerbate Arctic warming, acting as a positive feedback mechanism.

Additionally, the rapid Arctic warming, which is occurring faster than in other regions, leads to a meandering atmospheric circulation pattern. Recently, a new pathway for African dust transport to the Arctic has been identified. This study provides a detailed description of the Rapid Pathway (RP) and investigates the temporal variation of African dust influx into the Arctic via this route. Using GEOS-Chem model simulations, we demonstrate the RP's enhanced efficiency in accelerating African dust transport to the Arctic within approximately one week, compared to other pathways. Our analysis reveals a significant shift in African dust transport routes after 2000, with a marked increase in dust transport through the central North Atlantic (RP region), particularly in March and April. ERA5 wind field data reveal significant positive anomalies in poleward winds over the North Atlantic in March and April after 2000, facilitating northward dust transport via the RP region. In contrast, negative wind anomalies over Europe suggest a diminished role for the European pathway in Arctic dust transport.

Acknowledgements

I extend my sincere gratitude to Prof. Dr. Justus Notholt for providing me with the opportunity to pursue my PhD within his research group at the University of Bremen. Under his guidance, the research environment proved immensely supportive, and his willingness to share academic insights and offer constructive feedback greatly facilitated my growth throughout the entire research process. I am deeply appreciative of his continuous support and invaluable input into this thesis.

Special thanks are due to Dr. Mathias Palm for his dedicated supervision throughout my PhD journey. From the project's inception, Mathias provided essential guidance and invested considerable effort into its development. Our joint expedition to Ny-Ålesund, the northernmost observatory on Earth, not only provided invaluable hands-on experience but also deepened my understanding of FTS hardware and software. I am grateful for his meticulous review of my work and ongoing mentorship.

I express my appreciation to Dr. Christoph Ritter for his insightful explanations on ground-based polarization Lidar and aerosol property retrieval. Despite being in separate institutions, his guidance and assistance, particularly in aerosol-related matters, proved invaluable.

I am indebted to Philipp Richter for his crucial assistance during the initial phases of my PhD, especially in constructing the inversion model.

The progress of my thesis owes much to the enriching discussions with my colleagues at IUP. I extend my heartfelt thanks to Matthias Buschmann, Thorsten Warneke, Lukas Heizmann, Alexandra Klemme, Jamal Makkor, Christof Petri, Winfried Markert, and Jonas Hachmeister for their contributions and support.

My deepest gratitude goes to my family and friends, whose unwavering encouragement and support were instrumental throughout my PhD journey. Their understanding and patience during moments of stress and frustration were invaluable, and their presence remains the greatest source of strength and motivation.

Especially, I extend my profound gratitude to my wife, Dr. Xiaoyu Sun, whose unwavering support and love have been my anchor throughout this journey. Without her selfless dedication and unwavering belief in me, completing my studies would have been unimaginable.

Finally, I gratefully acknowledge the funding by the Deutsche Forschungsgemeinschaft (DFG, German Research Foundation) –Project nummer 268020496 – TRR 172 , within the Transregional Collaborative Research Center "ArctiC Amplification: Climate Relevant Atmospheric and SurfaCe Processes, and Feedback Mechanisms ($(AC)^3$)", in sub-project E02: Ny-Ålesund Column Thermodynamic Structure, Clouds, Aerosols, Trace Gases and Radiative Effects. I thank the AWI Bremerhaven and the AWI Potsdam for logistical support on the AWIPEV research base and the station personnel for on-site support. I thank the senate of Bremen for partial funding of this work.

Contents

List of Figures

List of Tables

List of Abbreviations

AA	Arctic Amplification
AERONET	AErosol RObotic NETwork
AOD	Aerosol Optical Depth
ARE	Aerosol Infrared Radiation Effect
AR	Atmospheric River
AW	Atmospheric Window
BC	Black Carbon
BSRN	Baseline Surface Radiation Network
CCN	Cloud Condensation Nuclei
CR	Color Ratio
ERA5	ECMWF Reanalysis v5
FTS	Fourier Transform Spectrometer
GHGs	GreenHouse Gases
IN	Ice Nuclei
LWD	Longwave Downward Radiation
MERRA-2	Modern-Era Retrospective analysis for Research and Applications version 2
NAO	North Atlantic Oscillation
RH	Relative Humidity
RP	Rapid Pathway
SSW	Sudden Stratospheric Warming
VOCs	Volatile Organic Compounds

Chapter 1

Introduction

Global warming, a consequence of climate change driven by human activities such as burning fossil fuels and deforestation, has profound impacts on various regions worldwide, including the Arctic. The Arctic, being particularly sensitive to climate change, experiences amplified warming compared to other parts of the Earth. This phenomenon is known as Arctic Amplification (Wendisch et al., 2017). To unravel the causes and impacts of rapid Arctic warming, numerous studies have concentrated on key processes driving Arctic amplification. These include temperature feedback mechanisms (Bony et al., 2006; Soden and Held, 2006), surface albedo feedback (Graversen, Langen, and Mauritsen, 2014), and the roles of cloud and water vapor feedback in the Arctic (Taylor et al., 2013; Philipp, Stengel, and Ahrens, 2020). As a result, the Arctic experiences unprecedented changes, including diminishing sea ice extent, thawing permafrost, and altering ecosystems. These changes not only affect the regional biodiversity and indigenous communities but also have global implications, such as rising sea levels and increasing extreme weather events (Hansen et al., 2014; Walsh et al., 2020). Aerosols have a significant impact on the climate system. They can influence cloud formation, alter precipitation patterns, and affect regional and global climate by modifying the energy budget of the atmosphere. Their role in cloud nucleation and modification affects cloud properties, such as lifespan and reflectivity, further influencing the Earth's energy balance.

Understanding aerosol radiative properties is crucial for climate scientists and policymakers as aerosols can either exacerbate or mitigate the effects of global warming. Accurate modeling and measurement of aerosol properties and their interactions with radiation are essential to better comprehend their impact on climate and to formulate effective strategies for mitigating climate change. Therefore, in this study, we will focus on the climatic effects of aerosols in the Arctic, including a new method of aerosol composition measurement, aerosol infrared radiation, and a new pathway for aerosol transport to the Arctic.

1.1 Climate Changes in the Arctic

The Arctic region is experiencing profound and rapid changes due to climate change (Barber et al., 2008; Wendisch et al., 2017; Box et al., 2019; Vincent, 2020). These changes involve all aspects of the environment, and some of the major climate changes observed in the Arctic include:

- Increasing temperatures: The Arctic is warming at about twice the global average rate (Serreze and Barry, 2011; Wendisch et al., 2017; Previdi, Smith, and Polvani, 2021). This rapid warming is causing widespread melting of glaciers, ice caps and permafrost throughout the region.
- Declining sea ice: The extent and thickness of Arctic sea ice has declined dramatically over the past several decades (Wang et al., 2020). The minimum extent of summer sea ice has reached an all-time low (Gascard, Zhang, and Rafizadeh, 2019).
- Permafrost thawing: Permafrost is thawing in the Arctic due to warming temperatures (Barber et al., 2008). Thawing permafrost has a wide range of impacts, including release of stored greenhouse gases (methane and carbon dioxide) (Knoblauch et al., 2018).
- Changes in ecosystems: A warming climate is altering Arctic ecosystems, affecting vegetation patterns, animal habitats, and migration routes (Descamps et al., 2017).

1.2 The significance of aerosols to climate

Aerosols play an important role in influencing the Earth's climate by interacting with radiation, clouds, and atmospheric processes. The impact of aerosols on climate can be either cooling or warming, depending on the different characteristics, composition, and concentration of aerosols. Different aerosols have different effects on the atmosphere, which include:

1. Direct radiative effects: Aerosols interact directly with solar and terrestrial radiation. Some aerosols scatter incoming solar radiation back into space, contributing to cooling by reflecting sunlight away from the Earth's surface. Conversely, some aerosols (e.g., black carbon) absorb sunlight, causing localized warming.
2. Indirect effects on clouds: Aerosols can act as cloud condensation nuclei (CCN) or ice nuclei (IN), forming cloud droplets or ice crystals. (1) An increased amount of aerosols may increase the cloud condensation nuclei (CCN) number concentration and lead to more, but smaller, cloud droplets for fixed liquid water content. This increases the albedo of the cloud, resulting in enhanced reflection and a cooling effect, termed the cloud albedo effect (Twomey, 1977). (2) Smaller drops require longer growth times to reach sizes at which they easily fall as precipitation. This effect, called the cloud lifetime effect, may enhance the cloud cover and thus impose an additional cooling effect (Albrecht, 1989).
3. Semi-direct aerosol effect: Absorbing aerosols also have the potential to modify cloud properties, without directly acting as CCN and IN, by (1) heating the air surrounding them while reducing the amount of solar radiation reaching the ground, which stabilizes the atmosphere and diminishes the convection and thus the potential for cloud formation, (2) increasing the atmospheric temperature, which reduces the relative humidity, inhibits cloud formation, and enhances evaporation of existing clouds.

Aerosols are short-lived, from several days to several weeks depending on spatial distributions. They may have different effects on different regions. Aerosols can have a significant impact on climate patterns by influencing atmospheric circulation, precipitation, and temperature distributions. This is due to the complex interactions between aerosols and the climate system, such as influencing the surface energy balance, altering atmospheric stability, and affecting precipitation processes. These interactions add to the complexity of the Earth's climate system.

Understanding the role of aerosols in climate is essential for accurate modeling and prediction of future climate change. However, the exact extent of aerosol impacts on climate remains uncertain due to the diversity of aerosol types, complex interactions with clouds, and the challenge of quantifying aerosol properties and distribution. Therefore, there is a need for improved observations, advanced modeling techniques, and continued research to better characterize aerosol properties, sources, transportation, and their impacts on the Arctic and global climate.

1.3 Challenges in Aerosol Composition Observations

Currently, the main parameter for aerosol observation is the aerosol optical depth (AOD). It is an important parameter to quantify the amount of aerosols in the atmosphere and to provide information about aerosol concentrations and their effect on light attenuation. The main modes of observation of aerosol optical depth are ground-based measurements (e.g., solar photometry, AERONET; LiDAR), satellite measurements (e.g., MODIS, MISR, and CALIOP), and airborne measurements.

Satellite instruments can provide measurements of large areas but are not very suitable in the Arctic due to the frequent existence of clouds and snow/ice on the surface, which make the measurements challenging (Lee et al., 2021). The in-situ measurements provide much more accurate measurements but are often limited to the planetary boundary layer, have limited coverage, and are sparse in time. Ground-based remote sensing provides measurements with a similar measurement geometry to satellites which are not confined to a particular altitude, unlike in-situ measurements. They provide time series measurements from the surface and have a similar viewing geometry as the satellite.

Measurements of aerosols in the Arctic face several challenges due to the unique environmental conditions and characteristics of the region:

- Cloud cover: The Arctic is often covered by clouds, especially during certain seasons. Clouds can obstruct satellite observations, limiting the availability of cloud-free data needed for accurate aerosol retrievals. This hinders the consistency and frequency of satellite aerosol measurements.
- Polar night: Optical measurements (e.g., solar photometers) that rely on solar radiation are limited during the polar night (winter).
- Surface reflectance and Brightness: The ice and snow cover prevalent in the Arctic is highly reflective at all wavelengths, making it difficult to distinguish between surface reflectance and aerosol signals. Complex algorithms and data processing techniques are required to obtain accurate aerosol characterization in bright surfaces.
- Low solar angle: Near the poles, the sunlight strikes the Earth's surface at a low solar angle. It affects the accuracy of aerosol retrievals because it affects the

interaction of light with aerosols, which affects the signal observed by satellite sensors.

1.4 Scientific Motivations

Aerosol influences the Arctic climate by aerosol-cloud interactions (Fan et al., 2016) and aerosol-surface interactions (Donth et al., 2020). For example, Black Carbon (BC) deposits on snow and ice, lowering the surface albedo (Ming et al., 2009; Bond et al., 2013) and thus warming the surface. Dust aerosols, when present in layers over high albedo surfaces and/or deposited to the snow, will warm the atmosphere (Krinner, Boucher, and Balkanski, 2006). Sulfate aerosols, organic matter, and sea salt cool the Arctic by scattering light back to space and by modifying the micro-physics of liquid clouds (Schmeisser et al., 2018). Besides, dust, ammonium sulfate and sea salt increase the cloud albedo by increasing ice crystal concentrations (Wagner et al., 2018).

In recent decades, mainly in-situ measurements of aerosols were performed in the Arctic. Most reports show that the aerosol composition is changing. Koch et al. (2011) and Ren et al. (2020) found that sulfate and BC are decreasing compared to the last century. Several projects in $(AC)^3$ (ArctiC Amplification: Climate relevant Atmospheric and surfaCe processes and feedback mechanisms) also focus on BC concentration measurements (Kodros et al., 2018; Zanatta et al., 2018) and reveal the annual cycle of BC in the Arctic, higher in spring and lower in early summer (Schulz et al., 2019). Shaw (1995), Francis et al. (2018), Francis et al. (2019) found that dust can be transported over long distances into the Arctic and plays an important role in Arctic haze. In recent years, the area of open water in the Arctic has become larger, and the sea surface temperature has increased. This leads to a local increase in the emission of sea salt (Domine et al., 2004; Struthers et al., 2011; May et al., 2016). Thus, during the Arctic Amplification, the aerosol composition in the Arctic also changes.

Hence, a combination of different measurement methods is necessary to provide a complete picture of aerosols in the Arctic. For aerosol composition measurement, the Fourier Transform spectrometer (FTS) is a possible instrument. A FTS (NYAEM-FTS) for measuring down-welling emission in the thermal infrared was installed in Ny-Ålesund (79 °N, 12 °E) in summer 2019. In this study, we want to answer three main scientific motivations:

1. Develop measurement and retrieval techniques to retrieve aerosol composition information.

2. If water is uptaken, how much do the differences in aerosol composition affect the infrared radiation effects?

3. Will aerosol transport pathways to the Arctic change with climate change?

1.5 Outline

The main results of this thesis are divided into three parts. The first part covers the algorithm for aerosol composition retrieval using FTS, which has been published (Ji et al., 2023) and is detailed in Chapter 3 and 4 (Methods in Sec.3.3, and results in

Sec.4.1). The second part addresses the infrared radiation effects of aerosols when water is uptaken, submitted to "Atmospheric Chemistry and Physics", with main content also in Chapters 3 and 4 (Methods in Sec.3.5, and results in Sec.4.2). The final part discusses new rapid pathway for aerosol transport to the Arctic, currently being prepared for publication, and is presented in Chapters 3 and 4 (Methods in Sec.3.6, and results in Sec.4.3).

In summary, Chapter 2 gives the background knowledge of the research in this study. Chapter 3 presents the methodology as well as the data used in the study. Chapter 4 gives the main results and analysis. A summary and outlook of this study is provided in the last chapter.

Chapter 2

Scientific background

The main purpose of this chapter is to introduce background knowledge on the study of Arctic aerosols. In the first section, we introduce the global atmospheric circulation system, including the Hadley, Ferrell, and polar cells. Polar climates are an important part of the global climate, and in the Sec.2.2 we describe polar climate systems, such as the Arctic dome, polar vortex and polar jet stream. The main focus of this study is on polar aerosols. The commonly mentioned physical and chemical characteristics of atmospheric aerosols are given in Sec.2.3. Atmospheric aerosol compositions are complex and variable, and their respective climatic characteristics should not be the same, and the climatic characteristics of different aerosol compositions are given in Sec.2.4. Finally, the radiative properties of aerosols and the radiative transfer models and Mie scattering codes required for the study are presented.

2.1 Atmospheric Circulation

Atmospheric circulation refers to the large-scale movement of air around the Earth, driven by the unequal heating of the planet's surface by the sun. This global circulation pattern plays an important role in redistributing heat, moisture, and energy across the atmosphere, influencing weather patterns, climate, and the Earth's overall climate system (Stevenson, 2019). Key components and processes of atmospheric circulation include:

1. Solar Radiation: The sun heats the Earth unevenly due to variations in the angle of sunlight striking different parts of the globe(Lang, 2013). The equator receives more direct sunlight, leading to warmer temperatures, while the poles receive less direct sunlight, resulting in cooler temperatures.

2. Hadley Cells (Hadley, 1735), Ferrel Cells (Fairbridge, 2005), and Polar Cells: these are the three primary cells that form the basis of the global atmospheric circulation. Warm air rises near the equator in the form of moist air, creating low-pressure regions. As this air moves towards the poles, it cools and sinks, creating high-pressure regions.

3. Trade Winds and Westerlies: surface winds are influenced by the atmospheric circulation cells, resulting in distinct wind patterns. Trade winds blow towards the equator from the northeast in the Northern Hemisphere and the southeast

in the Southern Hemisphere. Westerlies, found between 30 and 60 degrees latitude, blow from the west to the east.

4. Jet Streams: these high-altitude, fast-flowing air currents in the upper atmosphere influence weather patterns and the movement of storms. The polar and subtropical jet streams are meandering rivers of air that encircle the globe at high altitudes, affecting weather systems and air travel routes (Rodda, Harlander, and Vincze, 2022).

5. Coriolis Effect: the rotation of the Earth causes moving air masses to be deflected to the right in the Northern Hemisphere and the left in the Southern Hemisphere. This effect influences the direction of winds and the formation of large-scale wind patterns (Graney, 2011).

Figure 2.1 presents the atmospheric circulation cells and global wind systems. In the Arctic, the troposphere is in the sinking branch of the polar cell, thus generating polar high pressure, or "Arctic dome" as it will be described later in Section 2.2.1. At the top of the convection process, this corresponds to the region of convergence of the air currents, or polar vortex, as it will be described later in Section 2.2.2. From the meridian profile of circulation (Fig.2.1 right), there is a layer of higher wind speeds near the height of the polar front, a region we call the Arctic Jet Streams. These basic atmospheric circulations are important background information for the study of polar climate.

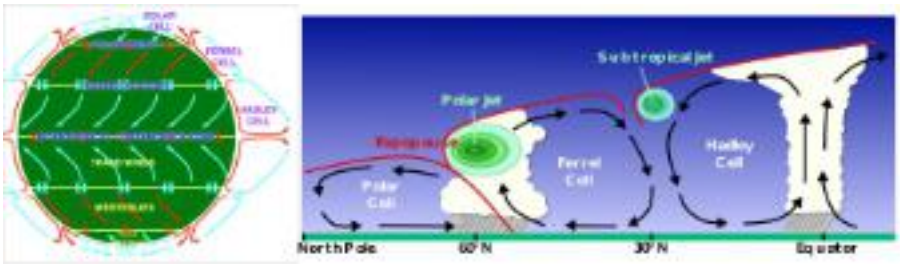

FIGURE 2.1: (left) Atmospheric circulation cells and global wind-systems. Source: https://upload.wikimedia.org/wikipedia/commons/c/cd/AtmosphCirc2.png; (right) Cross section of the subtropical and polar jet streams by latitude. Source: http://www.srh.noaa.gov/jetstream//global/images/jetstream3.jpg.

2.2 Arctic Atmospheric Circulation

2.2.1 Arctic Dome

The term "polar dome" in Earth sciences refers to a specific atmospheric phenomenon found in polar regions like the Arctic (Bozem et al., 2019) and the Antarctic. These polar regions experience high-pressure systems or dome-shaped regions of elevated atmospheric pressure. Polar domes are a result of radiative cooling during polar winter nights. As surface temperatures drop, they cool the nearby air, creating high-pressure systems. These stable atmospheric conditions limit cloud formation. Polar

domes are associated with extreme cold air and are significant in studies of polar climate, weather, and atmospheric dynamics.

2.2.2 Polar Vortex

The polar vortex is a large area of cold air and low pressure that surrounds the Earth's poles (Read, 2011). Although it always remains near the poles, it weakens in the summer and strengthens in the winter. The term refers to the counterclockwise flow of air that helps keep cold air contained around the poles and manifests itself in two distinct phenomena: the stratospheric polar vortex and the tropospheric polar vortex.

The stratospheric polar vortex is a high-speed cyclone with an altitude range of about 15 to 50 kilometers. The intensity of the polar vortex reaches its peak in winter, and it is formed in autumn when temperatures in the Arctic drop rapidly at the onset of the polar night. The increased temperature difference between the polar regions and the tropics fuels strong winds, and the Coriolis effect induces whirlpools. A sudden stratospheric warming (SSW) is an event that occurs when the stratospheric vortex breaks down during winter/spring.

The tropospheric polar vortex is usually defined as a region outside the tropospheric jet stream, from the surface to an altitude of about 10 to 15 kilometers, in the 40°N to 50°N region. Unlike the stratospheric vortex, the tropospheric vortex persists throughout the year. However, similar to the stratospheric vortex, the tropospheric vortex reaches its maximum intensity in the extreme cold of winter.

2.2.3 Arctic Jet Stream

The definition of the jet stream is given in Section. 2.1. One factor that contributes to the creation of a concentrated polar jet is the undercutting of sub-tropical air masses by the dense polar air masses at the polar front. In the free troposphere, the lack of friction leaves the air free to respond to the steep pressure gradient over the poles. This creates a planetary wind circulation with a strong Coriolis deflection, and can therefore be considered "quasi-geostrophic" (Fandry and Leslie, 1984). The polar frontal jet stream is closely related to the process of frontal formation in the mid-latitudes since the acceleration/deceleration of the jet stream gives rise to low-pressure/high-pressure zones, respectively, which lead to the formation of cyclones and anticyclones along the polar fronts in a relatively narrow region.

The polar vortex and polar jet stream are interconnected components of the polar atmospheric circulation and they influence each other's behavior. When the stratospheric polar vortex weakens or becomes disrupted (as in the case of Sudden Stratospheric Warming events), it can lead to changes in the jet stream's behavior (Dimdore-Miles et al., 2022; Lim et al., 2021; Lee, Polvani, and Guan, 2022). A weakened stratospheric polar vortex can allow colder air to move southward, altering the temperature contrast between polar and mid-latitude regions and influencing the strength and position of the polar jet stream.

Both the polar vortex and polar jet stream are integral parts of the larger atmospheric circulation system. Changes in one component can influence another component in the atmosphere, affecting weather patterns and atmospheric dynamics not only in the polar regions but also in mid-latitude regions.

Additionally, seasonal changes and weather patterns can influence the interactions between the polar vortex and polar jet stream, as shown in Fig.2.2. When the Arctic polar vortex is especially strong and stable (left globe), it encourages the polar jet stream, down in the troposphere, to shift northward. The coldest polar air stays in the Arctic. When the vortex weakens, shifts, or splits (right globe), the polar jet stream often becomes extremely wavy, allowing warm air to flood into the Arctic and polar air to sink down into the mid-latitudes.

In summary, while the polar vortex and polar jet stream exist at different altitudes within the atmosphere, they are interconnected components of the Earth's circulation system. Changes in one system can impact the behavior of another one, influencing weather patterns, air mass movements, and temperature distributions in the polar regions and further in mid-latitude regions. Understanding their interactions is crucial for the study of climate change and comprehending broader climate dynamics on a regional and global scale.

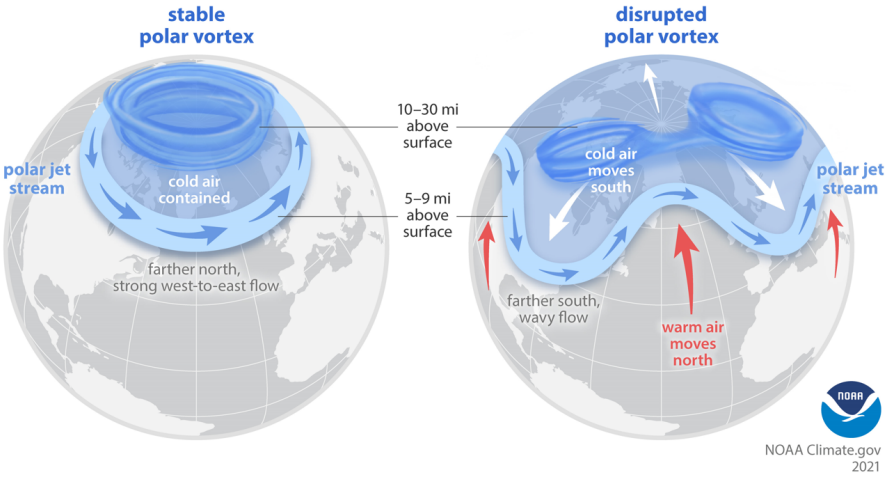

FIGURE 2.2: The schematic diagram of Polar vortex and polar jet stream under two different situations. NOAA Climate.gov graphic, adapted from original by NOAA.gov. Figure from:https://www.climate.gov/news-features/understanding-climate/understanding-arctic-polar-vortex

2.2.4 Sudden Stratospheric Warming

Sudden stratospheric warming (SSW) events are rapid and dramatic temperature increases (up to increases of about 50 °C) in the stratosphere, occurring primarily during the winter months in the polar regions (Butler et al., 2017). These events are characterized by a reversal of the typical westerly winds in the stratosphere to easterly winds. SSW events can have significant impacts on weather patterns in the troposphere, including disruptions to the polar vortex and changes in the strength and position of the jet stream (Charlton and Polvani, 2007).

During a typical northern hemisphere winter, multiple minor warming events take place, with a major event occurring approximately every two years. One factor contributing to major stratospheric warmings in the Northern hemisphere is the influence of orography and temperature contrasts between land and sea, which generate long Rossby waves (with wavenumbers of 1 or 2) in the troposphere. These

waves propagate upwards into the stratosphere and dissipate there, leading to a deceleration of the westerly winds and causing warming in the Arctic (Eliassen, 1961).

SSW events are often associated with changes in the structure and dynamics of the polar vortex, a large-scale circulation pattern centered near the poles. During an SSW event, the polar vortex can weaken or split, leading to disruptions in the circulation of cold polar air. The easterly winds progress down through the atmosphere, often leading to a weakening of the tropospheric westerly winds, resulting in dramatic reductions in temperature in Northern Europe (King et al., 2019).

2.2.5 North Atlantic Oscillation

The North Atlantic Oscillation (NAO) Index is a measure of the atmospheric pressure difference between the Icelandic Low and the Azores High in the North Atlantic Ocean (Hurrell et al., 2003). It is a prominent climatic phenomenon that significantly influences weather patterns in the North Atlantic region and beyond. The NAO Index is characterized by two phases: positive and negative, as shwon in Fig.2.3.

During the positive phase, there is a stronger pressure gradient between the Icelandic Low and the Azores High, resulting in stronger westerly winds across the North Atlantic. This typically leads to milder and wetter conditions in northern Europe and cooler conditions in southern Europe. Conversely, during the negative phase, the pressure gradient weakens, leading to weaker westerly winds and altered weather patterns across the North Atlantic region. The NAO Index plays a crucial role in modulating weather extremes, such as storms, heatwaves, and cold outbreaks, particularly in Europe and North America (Ning and Bradley, 2015; Francis and Skific, 2015; Vavrus et al., 2017).

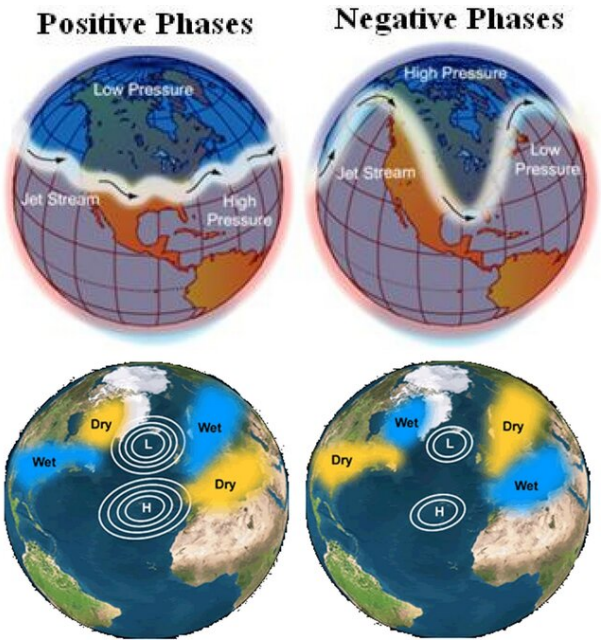

FIGURE 2.3: Positive and negative phases of the NAO(Source Institue of Geography, Berny, 2017, Figure from Hosseini, Kashki, and Karami (2022)

2.3 Atmospheric Aerosol

Aerosol is defined as a suspension system of solid or liquid particles in the atmosphere (Hinds and Zhu, 2022). The size of aerosol particles is usually between 0.01 and 10 µm (Mészáros and Vissy, 1974; Hussein et al., 2004; Gralton et al., 2011). Meteorologists usually refer them as particle matter - PM2.5 or PM10, depending on their size (Hartog et al., 2005; Pateraki et al., 2012). Aerosols in the atmosphere have several important environmental effects. They effect climate both directly (by scattering and absorbing radiation) (Rap et al., 2013; Yu and Huang, 2023) and indirectly (by serving as nuclei for cloud formation) (Lohmann and Feichter, 2005; Haywood and Boucher, 2000).

In the Arctic, aerosol events first attracted people's attention due to the phenomenon named "Arctic haze". Arctic haze was first noticed in 1750 at the beginning of the Industrial Revolution (Candelone et al., 1995). Smog is seasonal dependence, peaking in late winter and spring. In 1972, Glenn Edmond Shaw attributed the smog to trans-boundary anthropogenic pollution, with the Arctic receiving pollutants from sources several thousand miles away.

2.3.1 Sources and Sinks of Aerosols

Atmospheric aerosols originate from the condensation of gases and the wind on the Earth's surface. According to the aerodynamic diameter, it can be divided into TSP, PM10 and PM2.5 which refers to particles with aerodynamic diameter <= 100 mm, 10 mm and 2.5 mm, respectively. Aerosols come from a variety of sources, as presented in Fig.2.4. The majority of particles are generated from surface emissions. Primary aerosols are directly emitted (Tomasi and Lupi, 2017), with smaller ones forming as hot gases rapidly condense into particles before exiting smokestacks or tailpipes. Secondary aerosols result from gaseous emissions chemically converting into aerosol particles, some becoming cloud condensation nuclei (CCN) (Sun and Ariya, 2006; Tomasi and Lupi, 2017).

Aerosol originates from both natural and anthropogenic sources. Natural sources include sea spray, volcanoes, forests, forest fires, and the conversion of naturally occurring gases like sulfur dioxide (SO_2) and some Volatile organic compounds (VOCs). Anthropogenic sources includes industry, power plants, agricultural burning, transportation, and conversion of anthropogenic gases like $SO_2$and various other emissions.

Aerosols are removed from the atmosphere through dry and wet deposition. Dry deposition is the settlement of particulate matter by gravity or by collision with an object. Two mechanisms govern dry deposition: one involves particle settlement due to gravity onto surfaces like soil, water, plants, and buildings. The other mechanism involves sub-0.1 µm particles diffusing through Brownian motion and agglomerating into larger particles, either diffusing to the ground or eliminated by atmospheric turbulence-induced collisions. Dry deposition rate depends on particle size, density, air movement, and viscosity. Wet deposition, caused by rainfall or snowfall, eliminates particulate matter through rain-out and wash-out mechanisms. The classification of deposition methods depends on research objectives and the physical and chemical properties of the aerosols, encompassing six categories: dust, carbon (black carbon and organic carbon), sulfate, nitrate, ammonium salt, and sea salt aerosols, where carbon can be subdivided into black carbon and organic carbon.

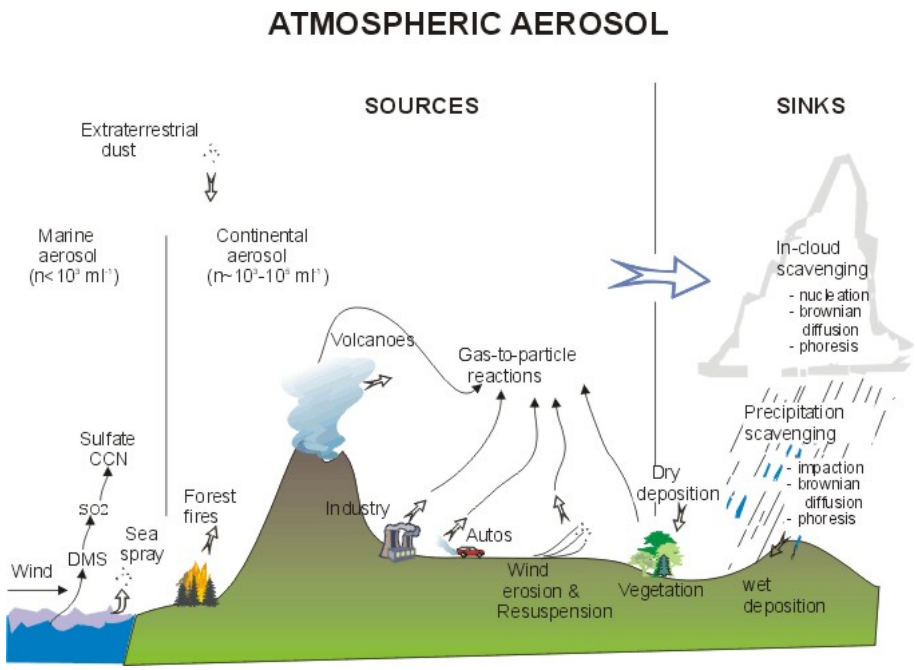

FIGURE 2.4: Sources of Atmospheric Aerosol: forest fires, extra terrestrial dust, continental aerosol, volcanoes, industry, autos, wind erosion and re-suspension, and gas-to-particle reactions. Sinks of Atmospheric Aerosol: in-cloud scavenging (nucleation, bornian diffusion, phoresis) and precipitation scavenging (impaction, brownian diffusion, phoresis). Credit: NOAA, Retrieved from: https://personal.ems.psu.edu/ lno/Meteo437/Aerosol.jpg

2.3.2 Aerosol Size Distribution

For a single particle, its particle size can be determined. However, for the particle groups that exist in the atmosphere, due to differences in their generation processes, the particle sizes are usually distributed within a certain range. As we presented in Fig.2.5, they are categorized into fine and coarse aerosols, with fine aerosols further divided into Aitken mode (diameter < 0.1 µm) and accumulation mode (diameter between 0.1 and 1.0 µm). Therefore, we need aerosol size distribution to describe the size of aerosols.

The Aitken mode, formed through gas-to-particle conversion, comprises particles originating from low-volatility vapors condensing onto surfaces, akin to water vapor. Coarse mode particles result from mechanical processes and include hydrophilic particles that can act as cloud condensation nuclei (CCN) but settle swiftly.

The accumulation mode consists of particles generated through coagulation or gas accumulation on nucleation particles. These particles neither settle rapidly nor coagulate, remaining in the atmosphere for weeks, making them effective CCN. Understanding these modes aids in comprehending how particles form and behave in the atmosphere.

As mentioned before, particles of different sizes originate from various sources, creating a size distribution with peaks that reveal insights into their formation. The diagram (compare 2.5) demonstrates these peaks, indicating higher concentrations of particles at specific sizes, offering valuable information about their creation.

In theory, the distribution function, n, of particle number concentration changing with scale can be defined as:

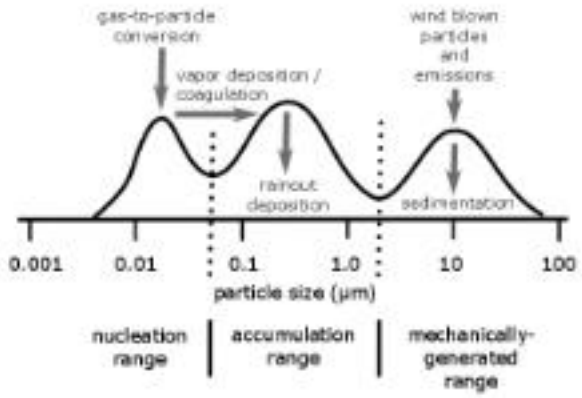

FIGURE 2.5: Typical aerosol size distributions and their sources and sinks. Nucleation range particles quickly grow into accumulation range particles, which fall slowly to the ground and stay a week or two in the atmosphere. The larger particles, called coarse particles, fall to the ground within hours or sometimes days. Gas-to-particle conversion means that the particles start as gases but are converted by reactions to sticky chemicals that form particles. Credit: W. Brune, Retrieved from: https://www.e-education.psu.edu/meteo300/node/671

$$n(D_p) = \frac{dN}{dD_p} \tag{2.1}$$

The number of particles in the range of particle size from D_p to $D_p + dD_p$ per unit volume. Therefore, the total number of particles of various scales within the unit volume is N, that is

$$N = \int_0^\infty n(D_p) d(D_p) \tag{2.2}$$

Because several aerosol properties depend on the aerosol surface, volume, and mass, it is often convenient to express the aerosol size distribution in the form of the surface size distribution ($dS/dD = \pi D^2 dN/dD$) in the approximation of spherical particles, volume distribution ($dV/dD = \frac{\pi}{6} D^3 dN/dD$), and mass distribution ($dM/dD = \rho dV/dD$, where ρ is the aerosol particle density). These represent the distribution of the surface area, volume, and mass of particles per cm^3 of air.

If we focus on the optical properties of aerosols, other size-related parameters frequently used to describe the aerosol size distribution are the (optical) effective radius (R_{eff}), defined as follows:

$$R_{eff} == \frac{\int \pi R^3 \frac{dN}{dD_p} dD_p}{\int \pi R^2 \frac{dN}{dD_p} dD_p} \tag{2.3}$$

2.3.3 Aerosols Wet Growth

In the atmosphere, certain types of dry aerosol particles, e.g. sea salt, and sulfates, can gradually absorb water vapor (Winkler, 1973). This phenomenon is known as

aerosol wet growth and is closely linked to an accompanying increase in longwave downward radiation (LWD) (Mauritsen et al., 2011). Two main factors influence the additional enhancement in LWD during aerosol wet growth, the aerosol composition and surrounding humidity (Peng, Chen, and Tang, 2022). Aerosols that possess the capacity to absorb water vapor are classified as hygroscopic aerosols (Tang and Munkelwitz, 1993). In the wet growth process, the ambient RH plays a vital role since it determines the conditions necessary for aerosol wet growth. Specifically, at a particular RH, the radius of the hygroscopic aerosol increases suddenly, which is known as the deliquescence point (Tang and Munkelwitz, 1993; Winkler, 1973). This is a characteristic of the specific hygroscopic aerosol (Onasch et al., 1999; Cziczo and Abbatt, 1999; Ge, Wexler, and Johnston, 1998; Wise et al., 2007; Cruz and Pandis, 2000; Ansari and Pandis, 1999). In contrast, the transformation of liquid to solid upon dehydration is called efflorescence (Ma et al., 2021; Estillore et al., 2017).

The ability of aerosols to absorb moisture at different RH is called hygroscopicity. It determines phase transitions (deliquescence and efflorescence) of hygroscopic compounds at different RHs (Martin, 2000; Lillard et al., 2009a). A diagram depicting the relationship between salt-water-content relative humidity is given in Fig.2.6. For a given compound, there are differences in the RH values corresponding to the deliquescence and efflorescence points. For example, sodium chloride (NaCl) has a deliquescence point of approximately 75% and a efflorescence point of approximately 46% (Peng, Chen, and Tang, 2022). This means that once NaCl has been activated, i.e. the ambient RH is ever above 75%, it will remain a wet particle until the ambient RH falls below the efflorescence point, i.e. 45%.

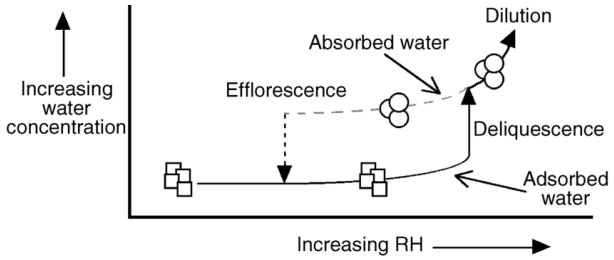

FIGURE 2.6: Diagram depicting the relationship between salt water content, relative humidity, and deliquescence. From Lillard et al. (2009a)

Additionally, the hygroscopic growth of aerosols changes the optical properties of aerosols, thus affecting their radiative effects. Therefore, when studying the effect of aerosol optical properties due to the hygroscopic growth of aerosols, we usually use empirical equations to express the change of aerosol size with atmospheric water vapour as follows Zieger et al. (2013) and Petters and Kreidenweis (2007):

$$\frac{r_{wet}(RH)}{r_{dry}} = \left(1 + \kappa \frac{RH}{1 - RH}\right)^{1/3} \tag{2.4}$$

where κ is the hygroscopic growth parameter of the particles.

2.3.4 Aerosol-Cloud Interaction

Aerosol-cloud interaction refers to the complex interplay between aerosols, tiny particles suspended in the atmosphere, and cloud formation and behavior. Aerosols can serve as cloud condensation nuclei (CCN) or ice nuclei (IN), providing the surfaces on which water vapor condenses or ice crystals form, respectively. This interaction influences cloud properties such as droplet size distribution, cloud albedo, lifetime, and precipitation patterns.

Wegener–Bergeron–Findeisen (WBF) process

In the Arctic, mixed phase cloud is a kind of clouds that is important for energy budget in the Arctic. Mixed-phase clouds represent a three-phase colloidal system consisting of water vapor, ice particles, and supercooled liquid droplets. When coarse aerosol particles exist in mixed clouds, there will be a mechanism like the snow removal process of spreading salt on ice/snow covered roads, consuming the ice water of ice crystals, and growing into small cloud droplets. Here, we start with the saturation vapor pressure over water. The August–Roche–Magnus formula (Alduchov and Eskridge, 1996) provides a very good approximation in the saturation vapor pressure over water:

$$e_s(T) = 6.1094 exp(\frac{17.626T}{T + 243.04}) \tag{2.5}$$

where e_s is in hPa, and T is in degrees Celsius. The saturation vapor pressure over ice that most used is given as follows:

$$e_{s,ice}(T) = 6.1121 exp(\frac{22.578T}{T + 273.86}) \tag{2.6}$$

Figure 2.7 presents the saturation vapor pressure over liquid water and ice as well as their difference with temperature. Therefore, when the ambient vapor pressure falls between the saturation vapor pressure over water and the lower saturation vapor pressure over ice, the sub-saturated environment for liquid water but a supersaturated environment for ice will result in rapid evaporation of liquid water and rapid ice crystal growth through vapor deposition. This is so called Wegener-Bergeron-Findeisen Process (Wegener, 1911; Bergeron, 1935; Findeisen, 1938). Here, the pure water means that there is no solute in the water. During the Bergeron process, the relationship between saturation vapor pressure in the ambient atmosphere with that over pure water and ice can be written as follows:$e_{s,ice} < e_{ambient} < e_{s,purewater}$.

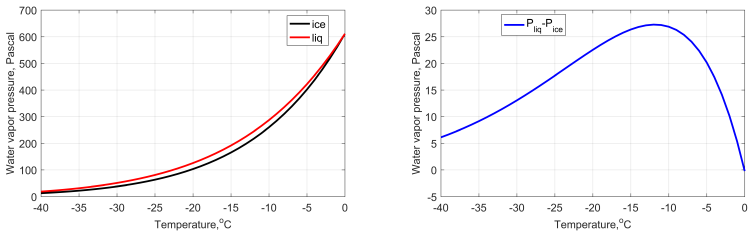

FIGURE 2.7: The saturation vapor pressure over pure water (red) and ice (black) in left, and the difference between water and ice in right.

Köhler theory

When it comes to cloud droplets, saturation vapor pressure over a cloud droplet changes. Two effects should be considered: the Kelvin effect (Thomson, 1872) and Raoult's law (Raoult, 1887; Raoult, 1889). The Kelvin effect describes the change in vapor pressure due to a curved liquid–vapor interface, such as the surface of a droplet. The vapor pressure at a convex curved surface is higher than that at a flat surface. Raoult's law relates the saturation vapor pressure to the solute. The two effects are combined, and this is the main point mentioned in the Köhler theory. Köhler theory describes the process in which water vapor condenses and forms liquid cloud droplets:

$$ln(\frac{p_w(D_p)}{p^0}) = \frac{4M_w\sigma_w}{RT\rho_w D_p} - \frac{6n_s M_w}{\pi\rho_w D_p^3} \tag{2.7}$$

where p_w is the droplet water vapor pressure, p^0 is the corresponding saturation vapor pressure over a flat surface, σ_w is the droplet surface tension, ρ_w is the density of pure water, n_s is the moles of solute, M_w is the molecular weight of water, and D_p is the cloud drop diameter.

The Köhler curve is the visual representation of the Köhler equation. It shows the supersaturation at which the cloud drop is in equilibrium with the environment over a range of droplet diameters. The exact shape of the curve is dependent upon the amount and composition of the solutes present in the atmosphere. The Köhler curves where the solute is sodium chloride are different from when the solute is sodium nitrate or ammonium sulfate.

Figure 2.8 shows three Köhler curves of sodium chloride. Consider (for droplets containing solute with diameter equal to 0.05 micrometers) a point on the graph where the wet diameter is 0.1 micrometers and the supersaturation is 0.35%. Since the relative humidity is above 100%, the droplet will grow until it is in thermodynamic equilibrium. As the droplet grows, it never encounters equilibrium, and thus grows without bound. However, if the supersaturation is only 0.3%, the drop will only grow until about 0.5 micrometers. The supersaturation at which the drop will grow without bound is called the critical supersaturation. The diameter at which the curve peaks is called the critical diameter.

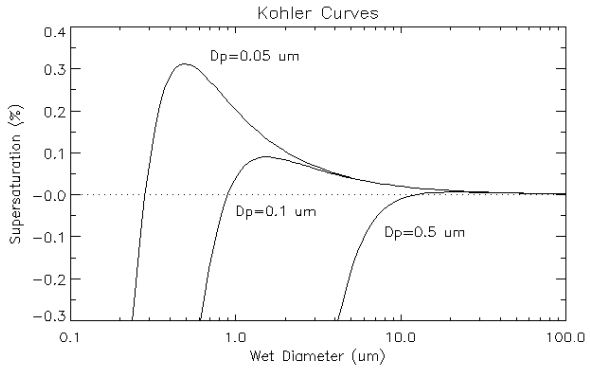

FIGURE 2.8: An example of Kohler curves showing how the critical diameter and supersaturation are dependent upon the amount of solute. It's assumed here that the solute is a perfect sphere of sodium chloride. Figure from: https://commons.wikimedia.org/wiki/File:Kohler_curves.png

2.3.5 Aerosol radiative properties

Aerosols are tiny particles suspended in the Earth's atmosphere, varying in size, composition, and origin. These particles play a crucial role in determining the radiative properties of the atmosphere. Aerosols can interact with solar radiation by scattering and absorbing incoming sunlight, as well as with terrestrial radiation by absorbing and emitting infrared radiation (Li et al., 2022).

Assuming that atmospheric aerosols are spherical particles, to determine how a spherical particle interacts with radiation at a specified wavelength, two parameters must be specified. The first one is the complex index of refraction, n, and the second one is size parameter. The index of refraction is the ratio of the speed of light in a vacuum to the speed of light through the material. The index of refraction depends on wavelength, and consists of a real (n_{re}) and imaginary (n_{im}) component:

$$n = n_{re} + n_{im} \tag{2.8}$$

The imaginary component corresponds to absorption and the real component to scattering.

Scattering of Aerosols

Most light that reaches the human eye is scattered light. Scattering is a physical process by which particles located in the path of an electromagnetic wave continuously extract energy from the incident wave and re-radiate this energy in all directions. In the atmosphere, scattering occurs on a wide range of particle sizes, from gas molecules to aerosols, small water droplets, ice crystals, and large raindrops and hail. The effect of particle size on scattering can be described by a physical term

called the size parameter(compare Equ.2.9). For spherical particles, the size parameter is defined as the ratio of the particle circumference to the incident wavelength:

$$x = 2\pi a/\lambda \tag{2.9}$$

When $x \ll 1$, it is Rayleigh scattering (Boucher, 1998). When $x > 1$ or $x \approx 1$, it is Lorenz-Mie scattering (Lorenz, 1890; Mie, 1908).

Aerosols scatter sunlight by redirecting it in different directions. The extent of scattering depends on the size of the particles and the wavelength of the incoming radiation. As shown in Fig.2.9, Rayleigh scattering occurs when particle sizes are much smaller than the wavelength of light; Whereas Mie scattering happens when the particle size is comparable to the wavelength. The light in Rayleigh scattering is symmetrical backward and forward, while the light in Mie scattering is essentially concentrated in the forward direction (the direction of incident light). Therefore, Mie scattering is characterised by forward scattering.

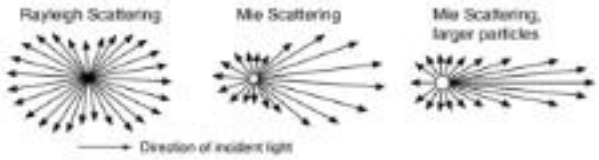

FIGURE 2.9: Schematic diagram of scattered light in Rayleigh scattering and Mie scattering. Figure from: http://hyperphysics.phy-astr.gsu.edu/hbase/atmos/blusky.html.

Usually, scattering can be expressed in terms of the scattering efficiency factor, Q_{sca}, which is defined as the ratio of the scattering cross section, σ_{sca}, of a particle to its geometric cross section,πr^2, (Bellouin and Yu, 2022):

$$Q_{sca} = \frac{\sigma_{sca}}{\pi r^2} \tag{2.10}$$

The scattering cross section,σ_{sca}, is the probability of scattering of radiation at a given wavelength is measured. It gives us an intuitive sense of how much area is blocked out by the target during a scattering event.

When a beam of light is blocked by aerosols in the atmosphere, it is scattered in all directions, and the scattering cross-section gives an indication of how much energy will be scattered. Then we need to know how the scattered light will be distributed in all directions. To describe the angular distribution of the scattered energy, the phase function is defined in radiative transfer theory::

$$\int_0^{2\pi} \int_{-1}^{1} P(\Theta) dcos(\Theta) d\phi = 4\pi \tag{2.11}$$

where Θ is the scattering angle, the angle between the direction of scattered light and the direction of incident light; ϕ is the azimuth angle. The phase function of

Rayleigh scattering is given by:

$$P_{Rayleigh}(\Theta) = \frac{3}{4}(1 + cos^2\Theta) \tag{2.12}$$

While the phase function of Mie scattering is determined by the size parameter, which is often given by numerical calculation.

Absorption of Aerosols

Aerosols can absorb solar radiation, which heats the ambient atmosphere. As we mentioned in Equ.2.8, the imaginary part of the refractive index means the absorption of aerosol. This absorption varies based on the composition of the aerosol particles. For instance, black carbon aerosols tend to absorb sunlight strongly, contributing to atmospheric warming, while other aerosol types may absorb less. Similar with the scattering efficiency, the absorption efficiency can be given as follow:

$$Q_{abs} = \frac{\sigma_{abs}}{\pi r^2} \tag{2.13}$$

where σ_{abs} is the absorption cross section. Then the extinction of radiation is the sum of the absorption and scattering:

$$\begin{aligned} Q_{ext} &= Q_{sca} + Q_{abs} \\ \sigma_{ext} &= \sigma_{sca} + \sigma_{abs} \end{aligned} \tag{2.14}$$

2.4 Climatic effects of Arctic Aerosols

2.4.1 Radiative Forcing of Aerosols

The net effect of aerosols on the Earth's energy balance is described as radiative forcing, as shown in Fig.2.10. It is the difference between the incoming solar radiation absorbed by the Earth and the outgoing longwave radiation emitted by the Earth and its atmosphere. Aerosols can cause both positive and negative radiative forcing, depending on their properties and interactions with radiation. Besides, aerosols have the biggest uncertainty in Fig.2.10a, which motivates us to do more detailed observations of aerosol composition and radiative effects.

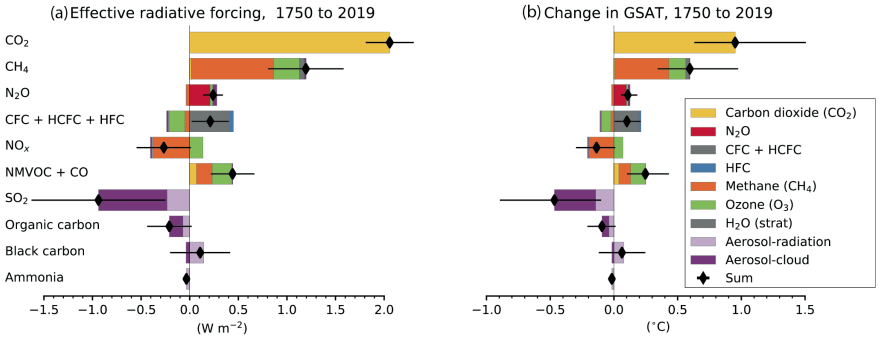

FIGURE 2.10: Contribution to effective radiative forcing (ERF) (a) and global mean surface air temperature (GSAT) change (b) from component emissions between 1750 to 2019 based on CMIP6 models (Thornhill et al., 2021). From IPCC (Climate Change (IPCC), 2023), download from: https://www.ipcc.ch/report/ar6/wg1/downloads/figures/IPCC_AR6_WGI_Figure_6_12.png.

2.4.2 Effects of Aerosol composition in The Arctic

Different types of aerosols have varied effects on the Arctic climate due to their distinct properties and interactions with the environment. Here's an overview of the climate effects of sea salt, sulfate, dust, and black carbon aerosols in the Arctic:

Sea Salt

Sea salt aerosols are primarily generated by the breaking of waves over the ocean surface (Lewis and Schwartz, 2004). In the arctic, the source of sea salt can also come from blowing snow (Frey et al., 2020) and frost flowers (Xu, Russell, and Burrows, 2016) . Usually, they have a cooling effect on the climate due to their ability to increase the number of cloud condensation nuclei (CCN) (Horowitz et al., 2020). In the Arctic, a recently study shows that the sea salt aerosol increases the longwave emissivity of clouds, leading to a calculated surface warming of +2.30 Wm^{-2} under cloudy sky conditions (Gong et al., 2023).

Sulfate

Sulfate aerosols are primarily formed from sulfur dioxide (SO2) emissions, often originating from industrial activities (Hand et al., 2012) and volcanic eruptions (Durant, Bonadonna, and Horwell, 2010). Sulphate aerosols can also come from the oxidation of marine dimethyl sulfide (DMS) (Fung et al., 2022). Generally, they have a cooling effect on the climate by increasing the reflectivity of clouds (albedo effect (Frey, Bender, and Svensson, 2017)) and by directly scattering incoming solar radiation (Kim et al., 2014). A recent model simulation in the Arctic showed that due to sea-ice melting, the simulated aerosol nucleation rate is higher, resulting in an overall increase in cloud droplet number concentration and a large increase in negative cloud radiative forcing. Thus, potential future reductions in sea ice area may lead

to increased cloud albedo and thus negative climate feedbacks on Arctic radiative forcing associated with oceanic DMS emissions (Mahmood et al., 2019).

Dust

Dust aerosols are predominantly generated from natural sources like desert regions and soil disturbances (Kok et al., 2021). Their impact on climate varies, as they can have both warming and cooling effects. Dust particles have a direct warming effect by absorbing solar radiation (Groot Zwaaftink et al., 2016a). However, they also contribute to cloud formation, potentially leading to a cooling effect depending on the type of clouds formed and their properties (Yin et al., 2002; Koehler et al., 2010). Dust aerosols transported to the Arctic from other regions can affect snow and ice albedo (Stone et al., 2007), contributing to localized warming when they settle on reflective surfaces.

Black Carbon

Black carbon (BC) aerosols are fine particles produced by incomplete combustion of fossil fuels, biomass, and biofuels. They have a significant warming effect on the climate by absorbing sunlight. When deposited on snow or ice surfaces, black carbon reduces surface albedo (Ming et al., 2009; Bond et al., 2013), leading to accelerated melting. Black carbon is considered one of the major contributors to Arctic warming, especially when deposited on snow and ice. Its presence contributes to the amplification of Arctic warming by accelerating the melting of ice and snow cover.

Each type of aerosol in the Arctic has a unique influence on the local climate, and their combined effects contribute to the complex and changing Arctic environment. Understanding these effects is crucial for assessing the overall impact of aerosols on Arctic climate dynamics.

2.5 Radiative Transfer Model

2.5.1 Radiative transfer theory

A beam of radiation traveling through a medium will be attenuated by its interaction with matters in this medium. If the radiation intensity I_λ changes to $I_\lambda + dI_\lambda$ after passing through ds thickness in its propagation direction, then there is:

$$dI_\lambda = -k_\lambda \rho I_\lambda ds \tag{2.15}$$

where ρ means the density of the medium, k_λ means mass extinction cross section ($cm^2 \cdot g^{-1}$), λ means the wavelength of the radiation. On the other hand, the intensity of radiation can also be enhanced by emission from the medium at the same wavelength as well as by multiple scattering. Therefore, we define the source function coefficient j_λ so that the intensity increase due to emission and multiple scattering is:

$$dI_\lambda = +j_\lambda \rho ds \tag{2.16}$$

where j_λ has the similar meaning with k_λ in physics. Combining the above two equations, we get

$$dI_\lambda = -k_\lambda \rho I_\lambda ds + j_\lambda \rho ds \tag{2.17}$$

Beer-Bouguer-Lambert Law

If atmospheric emission and multiple scattered radiation are neglected, then the equation can be simplified to:

$$\frac{dI_\lambda}{k_\lambda \rho I_\lambda ds} = -I_\lambda \tag{2.18}$$

Let the incident intensity at $s = 0$ be $I_\lambda(0)$. After passing through the separation distance $s1$, the emergent intensity can be obtained by integrating:

$$I_\lambda(s_1) = I_\lambda(0) exp(-\int_0^{s1} k_\lambda \rho ds) \tag{2.19}$$

Assuming that the medium is uniform, k_λ does not change with s. Therefore, define the path length:

$$u = \int_0^{s1} \rho ds) \tag{2.20}$$

Then, Equ.2.18 can be written as:

$$J_\lambda = B_\lambda(T) \tag{2.21}$$

This is so-called Beer-Bouguer-Lambert Law.

Radiation Transfer Equation

Consider a scattering-free medium in local thermodynamic equilibrium. When a beam of intensity I pass through it, both absorption and emission processes occur simultaneously. This is the transmission of infrared thermal radiation emitted by the earth and the atmosphere. At this time, the source function determined by Equation 2.15 is given by the Planck function:

$$I_\lambda(s_1) = I_\lambda(0) exp(-k_\lambda u) \tag{2.22}$$

Thus, the radiative transfer equation can be written as:

$$\frac{dI_\lambda}{k_\lambda \rho I_\lambda ds} = -I_\lambda + B_\lambda(T) \tag{2.23}$$

To solve the equation, we define the monochromatic optical depth of the medium between two points s and $s1$:

$$\tau_\lambda(s1, s) = \int_s^{s1} k_\lambda \rho ds' \tag{2.24}$$

Using $d\tau_\lambda(s1, s) = -k_\lambda \rho ds$, equation2.22 can be rewrite as:

$$\frac{dI_\lambda(s)}{d\tau_\lambda(s1, s)} = -I_\lambda + B_\lambda(T) \tag{2.25}$$

Multiply equation 2.24 by the factor $exp[-\tau_\lambda(s1, s)]$, then integrating the thickness ds from 0 to $s1$ is the Schwarzschild equation:

$$I_\lambda(s1) = I_\lambda(0)exp[-\tau_\lambda(s1, 0)] + \int_0^{s1} B_\lambda[T(s)]exp[-\tau_\lambda(s1, s)]k_\lambda \rho ds \tag{2.26}$$

2.5.2 Radiative Transfer models

When considering model simulation of downwelling emission from the atmosphere, two radiative transfer models are coupled and used in this case, one is the Line-by-Line Radiative Transfer Model (LBLRTM) (Clough et al., 2005) for the gaseous contribution, another is the DIScrete Ordinate Radiative Transfer model (DISORT) (Stamnes et al., 1988) for calculation of water droplets and aerosol particles. The coupled model based on LBLRTM and DISORT is called LBLDIS (Turner, 2005). The radiative transfer theory will be given in the next section (compare Sec.2.5.1). Using LBLDIS as a forward model, Richter et al. (2022) developed a retrieval algorithm, named as TCWRET, to do cloud parameter retrieval. In this study, we further develop this retrieval algorithm into aerosol composition retrieval. The main difference between the two is the scattering properties look-up table, which will be given in next chapter.

2.5.3 Mie-Code

In this study, sulfate, sea salt, dust, and BC are retrieved using the retrieval algorithm, TCWRET-V2. The complex refractive index database only covers the above-mentioned aerosols in the infrared band because the spectral signature of the other aerosols is too small and it is not possible to retrieve them from the IR spectra. The complex imaginary refractive index of sulfate and dust are based on OPAC/GADA database, BC from Chang and Charalampopoulos (1990), and sea salt from Eldridge and Palik (1997), and Palik (1997).

The aerosol optical properties are calculated using the Lorenz-Mie theory (Mie, 1908). The code for this calculation has been developed by Mishchenko et al. (1999). For aerosol scattering properties calculations, information on the aerosol size distribution as well as their shapes is also needed. In Mie code (Mishchenko et al., 1999), the sphere shape of aerosol with a single-mode log-normal size distribution

of particles is selected. The log-normal function is given as follows:

$$n_N(D) = \frac{N}{\sqrt{2\pi D ln(\sigma_g)}} exp(-\frac{ln^2(D/D_g)}{ln^2(\sigma)}) \tag{2.27}$$

Where N is the total aerosol number concentration D_g is the median diameter, and σ_g is termed geometric standard deviation. In this study, the geometric standard deviation of the size distribution of aerosol is assumed to be 0.2 and the effective radius (R_{eff}) is set from 0.1 to 1 µm. The main reason for setting the upper limit of the R_{eff} to 1 µm is that aerosols in the Arctic region are often below 1 µm, according to the measurements of aerosol size distribution in the Arctic area ((Asmi et al., 2016; Park et al., 2020; Boyer et al., 2022)). In addition, if such constraint is not set to 1 µm, occasionally, the retrieval of fine particles, such as sulfate and BC, will be mathematically increased for a better fit of the spectrum, which is artificial. Because sea salt can be larger than 1 µm, when the retrieved R_{eff} of sea salt is close to 1 µm and sea salt is the dominant aerosol, the database of sea salt is extended to 2.5 µm, and the retrieval is run again.

Chapter 3

Instruments, Data and Methods

In this study, I tried to answer three main scientific questions: How FTS retrieve aerosols composition information; how much the differences in aerosol composition affect the polar radiation budget; whether the pathways of aerosol transport to the Arctic change with climate change. First of all, we will give a introduction about the observatory site: Ny-Ålesund. Since the main instrument is the Emission Fourier Transform Infrared Spectrometer (FTS), Sec.3.2 gives the basic information about FTS. Sec.3.3 presents the emission FTS retrieval algorithm developed in this study. After obtaining the results of the aerosol composition, in Sec.3.5 the infrared radiation effects are given for aerosols of different composition. Finally, based on the Geos-Chem model simulation, we use dust as a kind of aerosol tracer to show the variation in the pathways of aerosols to the polar regions in Sec.3.6.

3.1 Site description

Ny-Ålesund (79 °N, 12 °E), Svalbard, is located in the North Atlantic atmospheric transport gateway to the Arctic (compare Fig.3.1). Ny-Ålesund experiences a distinctly polar climate due to its high latitude within the Arctic Circle. The meteorological characteristics of Ny-Ålesund are influenced by its extreme northerly location, resulting in specific weather patterns and climatic conditions:

1. Low Temperatures: Ny-Ålesund has cold temperatures, especially during winter. Average winter temperatures can plummet well below freezing, reaching lows of around -20°C to -30°C (-4°F to -22°F). Even during the relatively milder summer months, temperatures tend to remain cool, rarely exceeding 5°C (41°F).

2. Polar Night and Midnight Sun: The town experiences polar night and polar day due to its high latitude. From mid-November to late January, Ny-Ålesund encounters the polar night, where the sun remains below the horizon, resulting in continuous darkness. Conversely, from late April to mid-August, the area enjoys the polar day, with 24 hours of sunlight.

3. Strong Winds: Ny-Ålesund is susceptible to strong winds, which can significantly impact the local weather conditions. These winds, sometimes accompanied by snowfall, contribute to the challenging climate.

4. Precipitation: Precipitation in Ny-Ålesund primarily occurs as snow throughout most of the year. While total annual precipitation levels are relatively low, snowfall can occur even during the summer months, contributing to the persistent snow cover in the region from November to June.

5. Fog and Low Clouds: Fog and low-lying clouds are common occurrences in Ny-Ålesund, particularly during certain times of the year. These atmospheric conditions can reduce visibility and affect transportation and outdoor activities.

6. Ice Conditions: The surrounding waters and nearby glaciers significantly influence the local climate. Sea ice and icebergs are common in the vicinity, impacting maritime activities and influencing the local weather patterns.

The extreme meteorological conditions in Ny-Ålesund present unique challenges and opportunities for scientific research and exploration in various fields, particularly those related to climate, atmospheric studies, glaciology, and environmental sciences. These conditions make Ny-Ålesund an ideal location for studying the impacts of climate change on the Arctic region and its ecosystems. The AWIPEV[1] research base is part of the village Ny-Ålesund, jointly operated by AWI Potsdam[2] and IPEV institute[3]. The AWI Potsdam operates an extensive suite of instruments, some of which are a very useful complement to the NYAEM-FTS (section 3.2.2), including an aerosol Lidar instrument (section 3.3.4) and a sun-photometer. The geographical location of NY is given in Fig.3.1 .

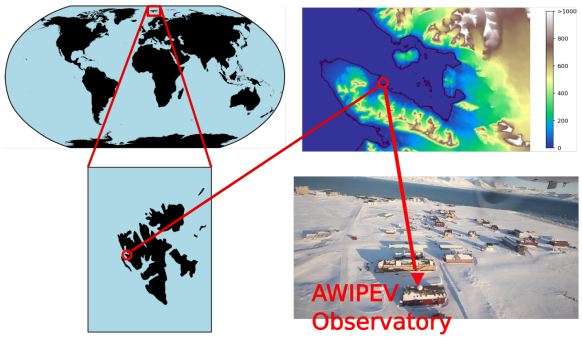

FIGURE 3.1: The location of Ny-Ålesund.

3.2 Fourier-transform infrared spectroscopy

Infrared (IR) spectroscopy is one of the commonly used spectroscopic techniques in qualitative and quantitative analysis in analytical laboratories. In atmospheric sciences, we can also use solar radiation and atmospheric radiation as radiation sources for IR spectroscopic studies, such as the well-known TCCON (Wunch et al., 2011) and NDACC (De Mazière et al., 2018) observation networks. The three main regions of infrared spectroscopic studies are the near-infrared 14000-4000 cm^{-1} , the mid-infrared 4000-400 cm^{-1} and the far-infrared 400-10 cm^{-1}.

[1] www.awipev.eu
[2] Alfred Wegener Institut; www.awi.de
[3] Polar Institute Paul Emile Victor; www.ipev.fr

3.2.1 The principle of the FTS

The first infrared spectrometer was built in 1835 and it quickly became an important tool for chemical characterisation. It used a dispersive design in which infrared light was split into different frequencies (wavelengths) and each frequency was detected sequentially (Theophanides, 2012). In the late 1960s, the development of Fourier Transform Infrared (FTS) spectroscopy led to a breakthrough in infrared spectroscopy. FTIR spectrometers can measure all frequencies simultaneously, which greatly accelerates acquisition time and improves signal-to-noise ratio and wavelength accuracy.

The FTIR spectrometer is based on a double-beam interferometer originally designed by Michelson in 1891(Michelson, 1891). The interferometer schematic in an FTIR spectrometer is given in Fig.3.2. It works by splitting the beam into two paths using a beamsplitter, with one path being reflected by a fixed mirror, and the other path being reflected by a moving mirror. After a path difference is created, the two beams recombine at the beamsplitter, resulting in interference. As the distance travelled by the second beam changes due to the moving mirror, the resulting infrared light has a different frequency distribution. The signal at the detector is recorded as a time-domain interferogram, which is then Fourier transformed to the frequency domain to obtain an infrared spectrum (Davis, Abrams, and Brault, 2001). The beamsplitter is a plate made of a partially reflecting and partially transmitting material. For example, Calcium Fluoride (CaF_2) and potassium bromide (KBr) are the base material, while the coating, e.g. Ge does the beam splitting and the partial reflection.

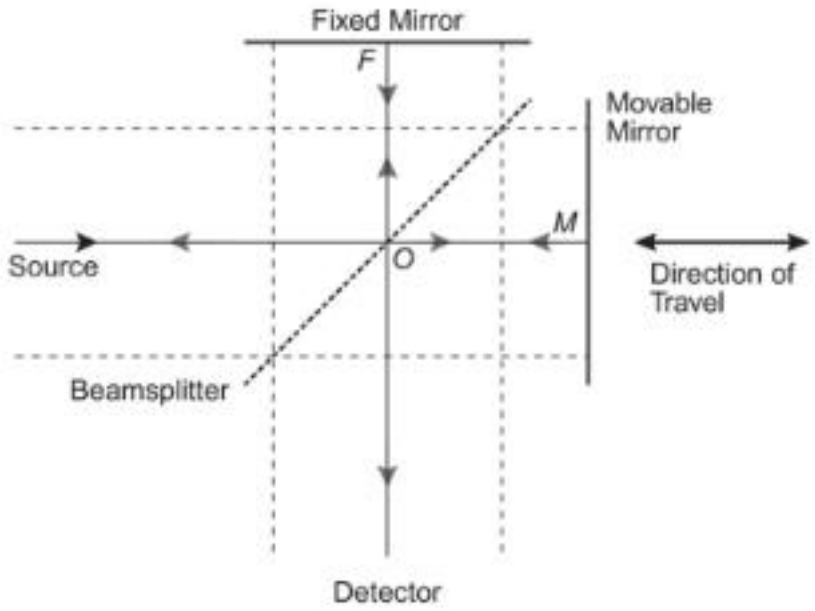

FIGURE 3.2: Interferometer schematic in an FTIR spectrometer.

Mathematically, for a non-periodic function $f(x)$ expanded into a Fourier integral the real form is:

$$f(x) = \int_{-\infty}^{\infty} [A(a)cos(ax) + B(a)sin(ax)]da \tag{3.1}$$

where $A(a) = \frac{1}{\pi}\int_{-\infty}^{\infty} f(x)cos(ax)dx$ and $B(a) = \frac{1}{\pi}\int_{-\infty}^{\infty} f(x)sin(ax)dx$ are called the Fourier transforms of $f(x)$. In addition, the Fourier transform convolution theorem should be mentioned here: If

$$f(x) = \int_{-\infty}^{\infty} f_1(x-t)f_2(t)dt \tag{3.2}$$

then $f(x)$ is the convolution of f_1 and f_2, written as $f = f_1 * f_2$. Convolution has such a relationship:

$$F\{f_1 * f_2\} = \frac{1}{2\pi}F\{f_1\} * F\{f_2\} \tag{3.3}$$

The Fourier transform, F of the multiplication of f_1 and f_2 is equal to $\frac{1}{2\pi}$ times the convolution of the Fourier transforms of f_1 and f_2 respectively, which is the Fourier convolution theorem.

As shown in Fig.3.2, when light from a monochromatic light source passes through the beamsplitter, it is divided into two equal parts and directed to a fixed mirror and a movable mirror. When the movable mirror is moved to a position such that the optical lengths of the two reflected beams are equal, then the two beams of light arriving at the detector will be the same, and hence constructive interference. Moving the moving mirror a quarter of a wavelength further will cause the two beams of light to be 180° out of phase, thus being destructive interference. For each successive quarter-wavelength movement of the moving mirror, the optical range of the two beams of light corresponding to the interferometer changes to one-half wavelength. Thus due to the principle of coherence of light, the interferogram produced by the interferometer will be a signal whose intensity changes to the form of a cosine, which can be written as:

$$I(s) = 2I(\tilde{v_0})[1 + cos(2\pi\tilde{v_0}s)] \tag{3.4}$$

where $I(s)$ is the intensity of the interferogram as a function of the optical path difference s, $\tilde{v_0}$ is the wave number of the incident monochromatic light, and $2I(\tilde{v_0})$ is the intensity of the incident light. For a multicolour light source, the interferogram $I(s)$ is a combination of the intensities of the signals generated for each frequency in the included spectrum, as follows:

$$I(s) = 2\int_0^{\infty} I(\tilde{v_0})[1 + cos(2\pi\tilde{v_0}s)]d\tilde{v} \tag{3.5}$$

The second part of the right-hand side of the equation actually expresses the characteristics of the interferogram and is thus called the interferogram function $F(s)$:

$$F(s) = 2\int_0^{\infty} I(\tilde{v_0})cos(2\pi\tilde{v_0}s)d\tilde{v} \tag{3.6}$$

By means of the Fourier transform we mentioned before, this leads to the familiar infrared spectrum $I(\tilde{\nu})$:

$$I(\tilde{\nu}) = 2\int_0^\infty F(s)cos(2\pi\tilde{\nu}_0 s)ds \tag{3.7}$$

The resolution of FTIR, $\Delta\tilde{\nu}$, is related to the maximum optical path difference,s_{max} , as follows:

$$\Delta\tilde{\nu} = \pm\frac{1}{2s_{max}} \tag{3.8}$$

For FTIR, the larger the maximum optical path difference, the higher the resolution of the instrument.

FTIR is extensively utilized in atmospheric studies, including the analysis of solar or lunar absorption and emission spectra, as well as the measurement of samples using lamps within the instrument. In lamp measurements, FTIR instruments employ artificial light sources to irradiate samples, allowing researchers to analyze the absorption or emission spectra of various materials. This technique enables the characterization of molecular structures, identification of chemical compounds, and determination of sample composition. In solar absorption studies, FTIR instruments are deployed to observe the attenuation of solar radiation as it passes through the Earth's atmosphere. By analyzing the absorption features in the solar spectrum, researchers can identify and quantify various atmospheric constituents, including greenhouse gases like carbon dioxide, methane, and ozone. Similarly, lunar absorption measurements involve analyzing the infrared radiation emitted by the Moon, which allows scientists to do atmospheric composition observation during the night. Besides, FTIR instruments are also employed in emission spectroscopy to study the thermal radiation emitted by the Earth's surface and atmosphere. By measuring the outgoing longwave radiation, researchers can infer temperature profiles, detect trace gases, and investigate radiative transfer processes. In this study, FTS is used in aerosol observation.

3.2.2 Emission FTS

The NYAEM-FTS consists of a Bruker Vertex 80 Fourier Transform Spectrometer, a SR800 blackbody and an automatically operated hutch which shields the instrument from the environment (compare Fig. 3.3 for a schematics of the setup). NYAEM-FTS is incorporated into the AWIPEV Observatory, a building which is operated and maintained by the AWI Potsdam as part of the AWIPEV research station. It is situated in a temperature stabilized laboratory.

The Bruker VERTEX 80 instrument is a table top instrument. In the version used here, the instrument has a resolution up to 0.08 cm^{-1} and an adjustable field of view in the range of 3.3 mrad to 22 mrad. The field of view is defined by the aperture inside the instrument. The beamsplitter is a KBr beamsplitter and the detector is an extended MCT detector with a sensitivity range 400 - 2500 cm^{-1}. The detector is cooled with liquid nitrogen and equipped with an automatic filling apparatus to ensure continuous operation without operator assistance. The instrument is purged with dry air to protect the parts which are hydroscopic. The laboratory is temperature regulated to stay within the range 21 - 25 $^\circ C$ maximum. There is no focal point outside the instrument, the parallel beam has a diameter of 4 cm and a maximum

divergence of 22 mrad. Thus, the probed area is circular with a diameter of about 880 m at 20 km altitude. The mirror selecting the emission source is the first optical part of the setup, hence the optical path is identical for the black-body source and the sky. Parts of the line-of-sight are within and nearby the laboratory, which explains the strong emission lines in the example spectrum (see Fig.4.1 in waveband 650 - 750 cm^{-1}) because of the high temperature in the first meters of the line of sight. The instrument is operated automatically and appended with a mirror to choose a target, the SR800 black-body or the atmosphere. The SR800 can be adjusted between 0 to 120 $^{\circ}C$ and holds the temperature within 0.1 K and is used as a black-body radiator. The surface is homogeneous to about 0.1 K. Additionally a cavity black-body radiator IR563 can be used for calibration purposes. The SR800 Black-body is operated by the acquisition software and measured regularly every few minutes.15Additionally two self-build black-body radiators are used for the continuous operation, which are itself calibrated frequently using the SR800 and IR563 black-bodies.

In order to protect the instrument from the harsh conditions in the Arctic, a automatic hutch has been build and will open the view to the atmosphere if conditions permit. Permitable is no precipitations, no snow drift and wind speeds of less than 15 m/s.

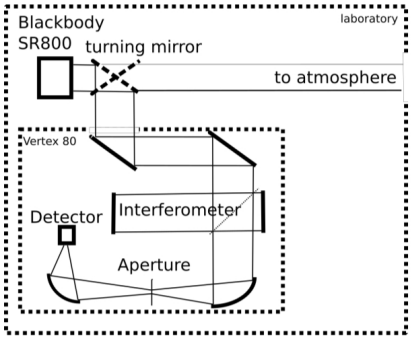

FIGURE 3.3: Schematics of the optical setup of the NYAEM-FTS spectrometer. Thew dashed line denotes the enclosure of the FT spectrometer and the enclosure of the laboratory.

Total power calibration

The black-body targets are used to perform a frequent total power calibration. For regular measurements a cold and a hot black-body, B_C and B_H, 20 $^{\circ}C$ and 100 $^{\circ}C$, respectively, are measured for calibration purposes. Since the emissivity of blackbody in real, α, is usually below 1, it means that the radiation of the blackbody is a mixture of the blackbody radiation and the temperature of the container, which is assumed to be blackbody radiation (Richter et al., 2022). The radiation by the emission FTS is the sum of the radiation of the radiator plus a term which takes into account the

temperature of the environment:

$$B = \alpha B(T_{BB}) + (1 - \alpha)B(T_{lab}) \tag{3.9}$$

Where T_{BB} is the temperature of blackbody, and T_{lab} is the temperature of container. According to Revercomb et al. (1988), the total power calibration is calculated via:

$$S = \frac{\alpha(B_H - B_C)}{\mathcal{F}(I_H - I_C)}\mathcal{F}(I_A - I_C) + \underbrace{\alpha B(T_c) + (1 - \alpha)B(T_{lab})}_{offset} \tag{3.10}$$

where S is the final spectrum, $B_{H,C}$ are theoretically calculated Planck curves of the hot and cold black-body. According to Richter et al. (2022), the assumption that the laboratory radiation is blackbody radiation can thus be relaxed to the assumption that the laboratory radiation is stable during one measurement sequence, which lasts only a few minutes. If one of the black-bodies is at the temperature of the laboratory, the offset term can be assumed a Planck-curve at laboratory temperature. $I_{H,C,A}$ are the interferograms of the measurements of the hot and cold black-body and the atmosphere, respectively. $\mathcal{F}$ denotes the Fourier-transform. The reason for using the Fourier transform of the differences of the interregnums is to mitigate the phase distortion due to parts of the spectrometer which radiate in the thermal infrared. The problem has been elaborated on by Revercomb et al. (1988). Revercomb et al. (1988) used the fact, that contributions from the instrument are the same regardless of the input level and vary very slowly compared the variation of the atmosphere, especially in a temperature stabilized environment. Using the difference of the interferograms those constant and slowly varying contribution are also removed. An example for a calibrated spectrum in clear sky conditions is in Fig.4.1. The raw data, i.e. the interferograms of the separate sources, are permanently stored at the Universität Bremen. The total power calibration can therefore be performed again, if necessary.

3.3 Retrieval Algorithm of Emission FTS

The retrieval algorithms, TCWRET-V1 and TCWRET-V2, are based on TCWRET developed by Richter et al. (2022). TCWRET-V1 is used for cloud parameter retrieval while TCWRET-V2 is modified for aerosol retrieval. The main difference between the two is the scattering properties look-up table. The forward model of the retrieval program TCWRET is the radiative transfer model LBLDIS (Richter et al., 2022) which consists of the clear sky radiative transfer model LBLRTM (Clough et al., 2005) and the scattering code DISORT (Stamnes et al., 1988) . The coupled model LBLDIS is used in several retrieval algorithms, such as MIXCRA (Turner, 2005), CLARRA (Rowe, Neshyba, and Walden, 2013), and TCWRET (Richter et al., 2022). Note that these retrieval algorithms share the same forward models. The differences are the particular implementation, e.g. of the scattering.

In this paper, TCWRET-V1 means TCWRET with cloud databases, while TCWRET-V2 (Ji et al., 2023) means TCWRET with aerosol databases. The algorithm reliability, or how well the method can precisely retrieve aerosol information, has been tested

in section 4.1.2. In the Sec. 3.3.2, the aerosol scattering properties look-up tables and artificial spectra simulated using a forward model are described in detail.

The retrieval method adopted in the modified TCWRET for the aerosol case is an optimal estimation method (Rodgers, 2000), the relationship between a measured emission spectrum $\boldsymbol{y}$ and unknown aerosol state $\boldsymbol{x}$ can be described by a simple mathematical model, as follows:

$$\boldsymbol{y} = \boldsymbol{F}(\boldsymbol{x}) + \boldsymbol{\varepsilon} \tag{3.11}$$

where $\boldsymbol{F}(\boldsymbol{x})$ is the forward model and $\boldsymbol{\varepsilon}$ is the error of observation. According to Rodgers (2000), the solution of the inverse problem is the state $\boldsymbol{x}$ minimizing a cost function $\boldsymbol{\xi^2}(\boldsymbol{x})$ usually defined as:

$$\boldsymbol{\xi^2}(\boldsymbol{x}) = [\boldsymbol{y} - \boldsymbol{F}(\boldsymbol{x})]^T \mathbf{S}_y^{-1} [\boldsymbol{y} - \boldsymbol{F}(\boldsymbol{x})] + [\boldsymbol{x}_a - \boldsymbol{x}] \mathbf{S}_a^{-1} [\boldsymbol{x}_a - \boldsymbol{x}] \tag{3.12}$$

where $\mathbf{S}_y^{-1}$ is the inverse measurement error covariance matrix, containing the variances of the spectral radiance; $\boldsymbol{x}_a$ is the a priori; $\mathbf{S}_a^{-1}$ is the inverse error of the a priori covariance matrix $\boldsymbol{x}_a$; The state vector $\boldsymbol{x}$ in modified TCWRET is defined as follows:$\boldsymbol{x} = (\tau_{seasalt}, \tau_{sulfate}, \tau_{dust}, \tau_{BC}, r_{seasalt}, r_{sulfate}, r_{dust}, r_{BC})$,$\tau$ means AOD of aerosols, and r means R_{eff} of aerosols.

Since the forward model is a non-linear function, an iterative method is needed to minimize the cost function $\boldsymbol{\xi^2}(\boldsymbol{x})$, given as follow:

$$\boldsymbol{x}_{n+1} = \boldsymbol{x}_n + \Delta x \tag{3.13}$$

Here $\boldsymbol{x}_n$ and $\boldsymbol{x}_{n+1}$ are the aerosol parameters of the n^{th} and $(n+1)^{th}$ step, and $\mathbf{s}_n$ is the modification of the aerosol parameters during the $n-th$ iteration. For weak non-linear problems, the Gauss-Newton (GN) method can be successfully applied, while in significant non-linear situations, the GN method is not guaranteed to decrease the cost function, therefore the method of steepest descent could be used. The Levenberg-Marquardt method (Marquardt, 1963; Lourakis et al., 2005) modification combines both methods by starting with the deepest descent method far away from the minimum and using the GN method near the minimum (Ceccherini and Ridolfi, 2010). At each iteration, a damping factor μ is adjusted in such a way that if the step results in a decrease in the cost-function, the damping factor μ is decreased, bringing the next step closer to the GN step. If the step causes the cost function to increase, the iteration is repeated with a higher damping factor μ, resulting in a step closer to the gradient descent direction. The adjustment vector $\mathbf{s}_n$ could be determined by the governing equation, as follows:

$$(\mathbf{K}_n^T \mathbf{S}_y^{-1} \mathbf{K}_n + \mathbf{S}_a^{-1} + \mu^2 \mathbf{S}_a^{-1}) \mathbf{s}_n = \mathbf{K}_n^T \mathbf{S}_y^{-1} [\boldsymbol{y} - \boldsymbol{F}(\boldsymbol{x}_n)] + \mathbf{S}_a^{-1} \cdot (\boldsymbol{x}_a - \boldsymbol{x}_n) \tag{3.14}$$

$\mathbf{K} = (\frac{\partial \boldsymbol{F}(\boldsymbol{x}_i)_n}{\partial \boldsymbol{x}_i})$is the jacobian matrix, i means parameters in the state vactor; $\mathbf{S}_y^{-1} = diag(\sigma_i^{-1})$ is the inverse measurement error covariance matrix, containing

TABLE 3.1: Micro-windows used in TCWRET to retrieve the micro-physical aerosol or cloud parameters (Richter et al., 2022).

Interval (cm^{-1})
558.5 - 562.0
571.0 - 574.0
785.9 - 790.7
809.5 - 813.5
815.3 - 824.4
828.3 - 834.6
842.8 - 848.1
860.1 - 864.0
872.2 - 877.5
891.9 - 895.8
898.2 - 905.8
929.6 - 939.7
959.9 - 964.3
985.0 - 991.5
1092.2 - 1098.1
1113.3 - 1116.6
1124.4 - 1132.6
1142.2 - 1148.0
1155.2 - 1163.4

the variances of the spectral radiance; $\boldsymbol{x}_a$ is the a priori; $\mathbf{S}_a^{-1}$ is the inverse error of the a priori covariance matrix $\boldsymbol{x}_a$; $\mu^2 \cdot \mathbf{S}_a^{-1}$ is the Levenberg-Marquardt (LM) term, as we mentioned before. $\boldsymbol{F}(\boldsymbol{x}_i)$ is the calculated spectral radiance and $\boldsymbol{y}$ is the measured spectral radiance.

The iteration is said to have converged, if the cost function $\boldsymbol{\xi^2}$ does not change anymore, i.e. the change in the cost function $\boldsymbol{\xi}$ is below a threshold. This threshold is set 0.001 in this study, i.e. the iteration has converged if

$$\frac{\boldsymbol{\xi}^2(\boldsymbol{x}_{n+1}) - \boldsymbol{\xi}^2(\boldsymbol{x}_{n+1})}{\boldsymbol{\xi}^2(\boldsymbol{x}_n)} < 0.001 \tag{3.15}$$

Besides, the selection of the inversion window is based on three main criteria: a) Sensitivity to aerosol signals; b) Insensitivity to trace gases; c) Avoidance of regions with a few gas absorption lines. Considering these factors, we ultimately selected specific bands for aerosol inversion. The micro-windows selected in aerosol retrieval is presented in Tab.3.1.

3.3.1 Averaging Kernels

The averaging kernels are a useful diagnostic tool to characterize the solution of the retrieval. In TCWRET, averaging kernels are calculated via

$$\mathbf{A} = \frac{\partial \boldsymbol{x}_r}{\partial \boldsymbol{x}} = \frac{\partial \boldsymbol{x}_r}{\partial \boldsymbol{y}} \frac{\partial \boldsymbol{y}}{\partial \boldsymbol{x}} = \mathbf{T}_r \cdot \mathbf{K}_r \tag{3.16}$$

where $\boldsymbol{x}_r$ is the retrieved state vector; $\boldsymbol{x}$ is the true value of state vector; $\mathbf{T}_r$ is the final transfer matrix $\mathbf{T}$ and $\mathbf{K}_r$ is the final jacobian matrix. According to Ceccherini and Ridolfi (2010), the final transfer matrix could be calculated as follows:

$$\begin{cases} \mathbf{T}_0 = \mathbf{0} \\ \mathbf{T}_{n+1} = \mathbf{G}_n + (\mathbf{I} - \mathbf{G}_n\mathbf{K}_n - \mathbf{M}_n\mathbf{S}_a^{-1})\mathbf{T}_n \\ \mathbf{G}_n = \mathbf{M}_n\mathbf{K}_n^T\mathbf{S}_y^{-1} \\ \mathbf{M}_n = (\mathbf{K}_n^T\mathbf{S}_y^{-1}\mathbf{K}_n + \mathbf{S}_a^{-1} + \mu^2\mathbf{D}_n)^{-1} \end{cases} \tag{3.17}$$

where $\mathbf{0}$ is a zero matrix and $\mathbf{I}$ is an identity matrix, other quantities are described before. The matrices $\mathbf{K}_n$ are calculated in Eq. 3.14. The calculation of the transfer matrix is performed in parallel to the minimisation. An example of averaging kernels is given as follows:

$$\boldsymbol{A} = \begin{array}{c} \begin{array}{cccccccc} \tau_{SS} & \tau_{SO4} & \tau_{Dust} & \tau_{BC} & Reff_{SS} & Reff_{SO4} & Reff_{Dust} & Reff_{BC} \end{array} \\ \begin{pmatrix} 0.280 & -0.099 & 0.264 & 0.232 & 0.093 & -0.046 & 0.014 & 0.073 \\ -0.057 & 0.940 & 0.047 & 0.042 & -0.067 & 0.057 & 0.026 & 0.020 \\ 0.006 & 0.006 & 0.585 & 0.036 & -0.007 & -0.040 & 0.151 & -0.022 \\ 0.172 & 0.178 & 0.163 & 0.171 & 0.030 & -0.011 & 0.023 & 0.065 \\ 0.248 & -0.134 & 0.268 & 0.250 & 0.112 & -0.042 & 0.075 & 0.063 \\ 0.000 & 0.000 & 0.000 & 0.000 & 0.000 & 0.000 & 0.000 & 0.000 \\ 0.012 & 0.025 & 1.354 & 0.102 & -0.023 & -0.075 & 0.414 & -0.051 \\ 0.149 & 0.177 & 0.195 & 0.190 & 0.045 & -0.014 & 0.062 & 0.061 \end{pmatrix} \end{array} \begin{array}{c} \tau_{SS} \\ \tau_{SO4} \\ \tau_{Dust} \\ \tau_{BC} \\ Reff_{SS} \\ Reff_{SO4} \\ Reff_{Dust} \\ Reff_{BC} \end{array}$$

The averaging kernels belong to the retrieved result, because they include much information about the retrieval results, e.g. how much influence is exerted by the a priori and how independent the retrieved quantities are from each other. On the diagonal elements one finds the derivatives of each element in the retrieved state vector with respect to its corresponding element in the true state vector. From the averaging kernel (refer to the example $\boldsymbol{A}$ above), the AOD of sulfate is the parameter least dependent on a priori information, followed by the AOD of dust and sea salt. Except for dust, all other aerosol size information is difficult to be retrieved. Besides, the information in each row or column suggests that there is very little connection between the parameters and that they are all independent of each other, supporting the finding of the low correlation in sec. 3.4.

3.3.2 Dry Aerosol Scattering Properties Look-up Tables

In this study, sulfate, sea salt, dust, and BC are retrieved using the retrieval algorithm, TCWRET-V2. The complex refractive index database only covers the above mentioned aerosols in the infrared band because the spectral signature of the other aerosols is too small and it is not possible to retrieve them from the IR spectra. The complex imaginary refractive index of sulfate and dust are based on OPAC/GADA database, BC from Chang and Charalampopoulos (1990), and sea salt from Eldridge and Palik (1997), and Palik (1997) (compare Fig. 3.4).

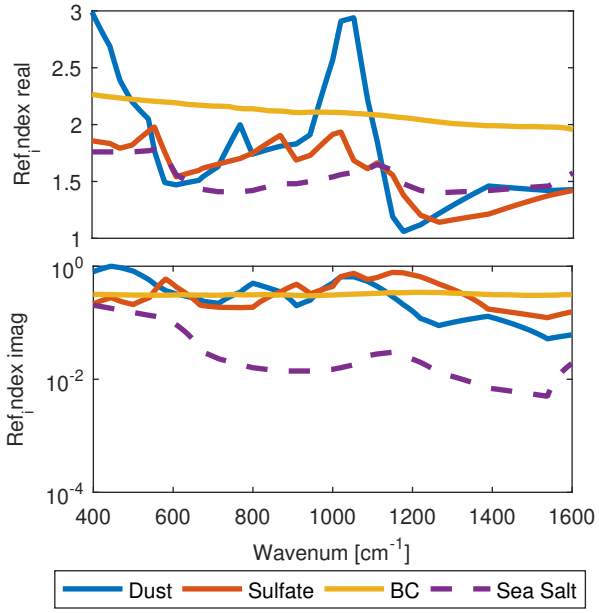

FIGURE 3.4: The complex refractive index of dust, sulfate, BC, and sea salt. The complex imaginary refractive index of sulfate and dust are based on OPAC/GADA database, BC from Chang and Charalampopoulos (1990), sea salt from Eldridge and Palik (1997), and Palik (1997). Those data have been downloaded from: http://eodg.atm.ox.ac.uk/ARIA/.

The aerosol optical properties are calculated using the Lorenz-Mie theory. The code for this calculation has been developed by Mishchenko et al. (1999). For aerosol scattering properties calculations, information on the aerosol size distribution as well as their shapes is also needed. In Mie code (Mishchenko et al., 1999), the sphere shape of aerosol with a single-mode log-normal size distribution of particles is selected. The aerosol size distribution in this study is given as follows:

$$n_N(D) = \frac{N}{\sqrt{2\pi D ln(\sigma_g)}} exp(-\frac{ln^2(D/D_g)}{ln^2(\sigma)}) \tag{3.18}$$

Where N is the total aerosol number concentration D_g is the median diameter, and σ_g is termed geometric standard deviation. In this study, the geometric standard deviation of size distribution of aerosol is assumed to be 0.2 and the effective radius (R_{eff}) is set from 0.1 to 1 µm. The main reason for setting the upper limit of the R_{eff} to 1 µm is that aerosols in the Arctic region are often below 1 µm, according to the measurements of aerosol size distribution in the Arctic area ((Asmi et al., 2016; Park et al., 2020; Boyer et al., 2022)). In addition, if such constraint is not set to 1 µm, occasionally, the retrieval of fine particles, such as sulfate and BC, will be mathematically increased for a better fit of the spectrum, which is artificial. Because sea salt can be larger than 1 µm, when the retrieved R_{eff} of sea salt is close to 1 µm and sea salt is the dominant aerosol, the database of sea salt is extended to 2.5 µm and the retrieval is run again.

3.3.3 Wet Aerosol Scattering Properties Look-up Tables

Ji et al. (2023) describe a modified retrieval algorithm based on TCWRET (Richter et al., 2022) for retrieving aerosol composition. The primary difference are the databases for various emission sources, such as clouds (Richter et al., 2022) or dry (Ji et al., 2023) or activated aerosols (in this study). For activated aerosols, two activated aerosols databases are created following the steps described in Ji et al. (2023). When creating the new databases of activated aerosols, there is an additional step that takes into account the complex refraction index of wet aerosols and the particle size of hygroscopic particles as a function of RH. Therefore, the following parameterization method (Zieger et al., 2013; Petters and Kreidenweis, 2007) is applied:

$$\frac{r_{wet}(RH)}{r_{dry}} = \left(1 + \kappa \frac{RH}{1 - RH}\right)^{1/3} \tag{3.19}$$

where κ is the hygroscopic growth parameter of the particles.

To calculate the complex refractive index of wet aerosol, the volume fraction of dry aerosol (Chin et al., 2002), f_d, is used:

$$\begin{cases} R_{wet} = & f_d R_d + (1 - f_d) R_{water} \\ I_{wet} = & f_d I_d + (1 - f_d) I_{water} \end{cases} \tag{3.20}$$

where R_d and R_{water} mean the real part of dry particles and water respectively; I_d and I_{water} mean the imaginary part of dry particles and water respectively.

The deliquescence point is about 75% for sea salt and 85% for sulfate (Peng, Chen, and Tang, 2022). Therefore, when the aerosol layer's ambient RH is less than 75%, dry aerosol databases are used for retrieval. The activated sea salt particle database replaces the dry sea salt particle database when the ambient RH reaches 75% to 85%. Both the activated sulfate and sea salt databases are utilized when the ambient RH exceeds 85%.

3.3.4 Additional Data Used in TCWret-V2

The Raman-Lidar "KARL"

The aerosol height information is needed for aerosol composition retrieval. This data can be either gained from Lidar measurement or Cloudnet. Here, we use Raman-Lidar for a case study and for long time period retrieval, Cloudnet data is the source of aerosol height information.

In Ny-Ålesund, a Raman-Lidar "KARL" is operated to measure in 3 colors (355, 532, and 1064 nm) (Ritter et al., 2016). It is positioned about 10 meters away from NYAEM-FTS measurement also pointing skywards. Aerosol backscatter coefficients (in all three colors), extinction coefficients (355 and 532 nm), and depolarization (355 and 532 nm) are measured.

For Lidar products, the aerosol backscatter coefficient (β^{aer}), the aerosol depolarization (δ^{aer}) and the color ratio (CR) are used for aerosol optical property analysis. According to Freudenthaler et al. (2009), the definitions of those quantities are given

TABLE 3.2: Aerosol classification by Lidar measurements as given by Ritter et al. (2016)

Classes	$\beta_{532}^{aer}(Mm^{-1}sr^{-1})$	δ_{532}^{aer}	CR	Description
Clear day	$\beta < 0.4$	$\delta < 2.05\%$		Clear day
Clear depol.	β<0.4	$\delta \geq 2.05\%$		Clear day with polarized signal.
Spherical Aerosol	$0.4 \leq \beta < 1$	$\delta < 2.05\%$		Spherical fine particles, possibly from long-distance transportation, e.g. sulfate.
Depol. Aerosol	$0.4 \leq \beta < 1$	$\delta \geq 2.05\%$		Polarized fine particles with irregular shapes, e.g. dust.
Activated Aerosol	$1 \leq \beta \leq 3$	$\delta < 2.05\%$	$CR < 1.7$	Aerosol hygroscopic growth into larger size, e.g. sea salt, sulfates.
Dense Aerosol	$1 \leq \beta \leq 3$		$CR \geq 1.7$	Medium size aerosol, e.g. sea salt, dust.
Cloud	$\beta > 3$			Cloud

as follows:

$$\delta^{aer}(\lambda) = \frac{\beta_{\perp}^{aer}(\lambda)}{\beta_{\parallel}^{aer}(\lambda)} \tag{3.21}$$

$\beta_{\perp}^{aer}(\lambda)$ and $\beta_{\parallel}^{aer}(\lambda)$ are the backscatter coefficients of the vertical and parallel polarized light, respectively. The depolarization depends on the particles' shape, e.g. spherical particles do not show any depolarization in the backscatter.

$$CR(\lambda_1, \lambda_2) = \frac{\beta_{\lambda_1}^{aer}}{\beta_{\lambda_2}^{aer}} \tag{3.22}$$

β_{λ}^{aer} is the aerosol backscatter coefficient at wavelength λ. More details are given in Freudenthaler et al. (2009) and Ritter et al. (2016). Based on that, Ritter et al. (2016) distinguished six conditions for the aerosol classification using those Lidar quantities (compare Tab. 3.2).

Instruments Joint Observation Scheme

As previously indicated, it is difficult to distinguish between thin clouds and aerosols only relying on the NYAEM-FTS instrument. To select the spectra in aerosol-only scenarios, the measurements of the KARL Lidar are used.

The aerosol or cloud height is determined from the KARL Lidar measurement and provided to the retrieval algorithm, TCWRET (compare Sec. 3.3). For cloud-only observations, the first version of retrieval algorithm, Total Cloud Water retrieval (TCWRET-V1), is used to retrieve cloud parameters as described by Richter et al. (2022). For aerosol-only events, the modified version, TCWRET-V2, is used to do the aerosol components retrieval. For complex situations with simultaneous existence of clouds and aerosols, the concurrent NYAEM-FTS measurements will be excluded. The flow diagram of the joint observation scheme is found in Fig. 3.5a.

The flow diagram in TCWRET-V2 is given in Fig. 3.5b. As shown in Fig. 3.5b, there are several inputs for model simulations. Firstly, the databases for scattering coefficients of different aerosol types are calculated using Mie code (Mishchenko et

al., 1999) based on aerosol complex refractive index and aerosol size distribution. Secondly, the atmospheric state profile, which includes temperature, humidity, and pressure (referred to as THP), is obtained from ERA5 reanalysis data with a time resolution of 3 hours (Hersbach et al., 2018). The third input is the aerosol height information, which is provided by the KARL Lidar (Sec. 3.3.4). To obtain the temperature of the aerosol layer, the fourth input, the ERA5 temperature is interpolated to the altitude measured by the KARL Lidar. Furthermore, for all aerosol types, the a priori information of aerosol is fixed as AOD = 0.0001 and R_{eff} = 0.35 µm.

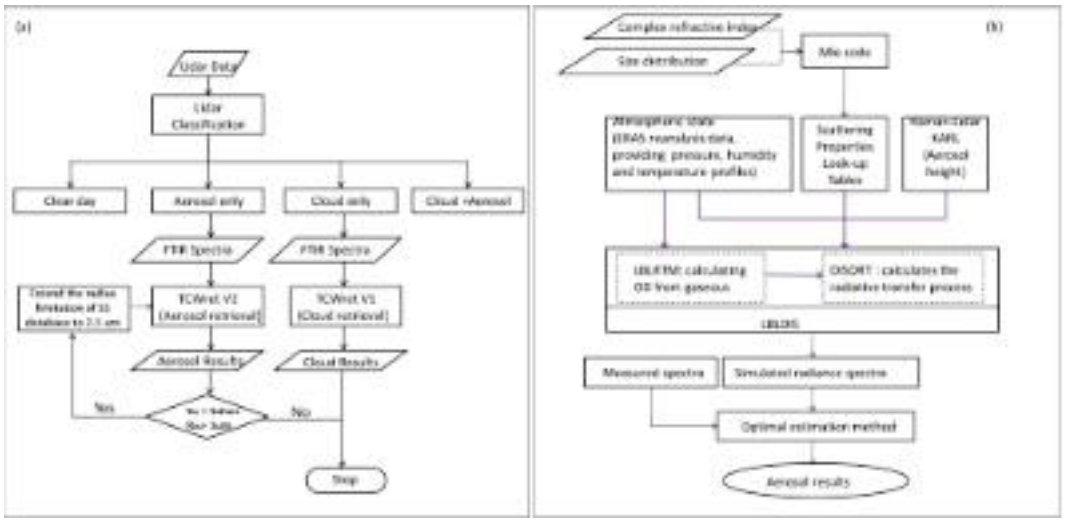

FIGURE 3.5: Instruments Joint Observation Scheme (a) and flow diagram of TCWRET-V2 (b).

3.3.5 Aerosol Data from AERONET and MERRA-2

The AErosol RObotic NETwork, commonly known as AERONET (Holben et al. (1998) and Giles et al. (2019); https://aeronet.gsfc.nasa.gov, last access: 24 May 2024), represents a comprehensive and globally distributed ground-based observational system specifically designed to measure and analyze aerosol optical properties in Earth's atmosphere. Established in the early 1990s, AERONET has since become a pivotal component of atmospheric research, offering critical data on aerosol particles and their impact on climate, air quality, and environmental processes.

AERONET consists of a network of sun photometers strategically positioned across various geographical locations worldwide. These sun photometers are equipped with high-precision instruments that capture direct sunlight, enabling the measurement of spectral aerosol optical depth (AOD) and other essential parameters like aerosol size distribution, and optical properties.

As mentioned previously (compare Sec.1.4), there is limited aerosol composition data available from direct observations, but the MERRA-2 dataset, based on model reanalysis, provides detailed information on aerosol composition.

The Modern-Era Retrospective analysis for Research and Applications version 2 (MERRA-2) stands as a comprehensive and widely utilized global atmospheric reanalysis dataset developed by NASA's Global Modeling and Assimilation Office (GMAO). MERRA-2 offers a detailed representation of various atmospheric parameters, including aerosol components, over an extensive temporal span from 1980 to the present day(Gelaro et al., 2017).

Among its rich collection of atmospheric data, MERRA-2 includes information specifically related to aerosols. This encompasses assimilated aerosol diagnostics such as column mass density for distinct aerosol constituents like black carbon (BC), dust, sea salt, sulfate, and organic carbon. Additionally, MERRA-2 provides surface mass concentration details for these aerosol components and comprehensive data on total extinction (and scattering) Aerosol Optical Depth (AOD) at 550 nm. An hourly time-averaged 2-dimensional data collection (M2T1NXAER) in MERRA-2 is used in this study.

3.3.6 Summary of Retrieval Algorithm

It is possible to invert the compositional information of aerosols using FTIR spectroscopy. Currently, the aerosol composition information that we can invert is sea salt, sulphate, black carbon, and sand and dust. The inversion algorithm also includes the wet growth process of aerosols. In addition, aerosol information from a single instrument is limited, so we have developed a joint observing programme using radar to provide more accurate a priori information and meteorological parameters for aerosol inversion. At present, the algorithm can be inverted only for the presence of aerosols in the atmosphere or only for the presence of clouds, and inversion for the more complex cases of multi-layer clouds and aerosols requires further development in the future.

3.4 Aerosol Composition Dataset from FTS

Following the method described in Sec.3.3, sulfate (dry or wet state), sea salt (dry or wet state), dust and BC is retrieved under different RH conditions. The retrieved aerosol composition data are from 2019 to 2022.

For continuous long-term observation of aerosols, Cloudnet (Ebell et al., 2023) is a better alternative to the "KARL" Lidar measurement due to its improved data continuity and inclusion of aerosol height data and cloud type information. The details of Cloudnet will be given in the next section (see Sec.3.5.1). With the Cloudnet dataset, aerosol-only situations can be distinguished and the corresponding spectra are retrieved using TCWRET-V2.

3.5 Infrared Radiation Effect of Aerosol ("ARE")

Arctic amplification (AA), characterized by the accelerated warming of the Arctic region compared to global averages, is a phenomenon of importance in climate change (Serreze and Barry, 2011; Wendisch et al., 2017; Peace et al., 2020). This amplified warming is particularly pronounced during the polar night, highlighting the need for a comprehensive understanding of its causes and consequences (Chung et al., 2021). To elucidate the underlying mechanisms driving AA, extensive research has focused on key processes such as temperature feedback, surface albedo feedback, and cloud and water vapor feedback (Bony et al., 2006; Soden and Held, 2006; Graversen, Langen, and Mauritsen, 2014; Taylor et al., 2013; Philipp, Stengel, and Ahrens, 2020). Among these, aerosols are an important factor in Arctic climate

dynamics, influencing various feedback mechanisms. For instance, dust and Black Carbon (BC) deposition on snow or ice surfaces reduce albedo, accelerating ice melt (Ming et al., 2009; Bond et al., 2013). Moreover, sea salt aerosols modify cloud properties, enhancing longwave downward radiation (LWD) and contributing to surface warming (Gong et al., 2023).

In the context of the Arctic energy budget, LWD constitutes a critical component, primarily governed by greenhouse gases (GHGs) in the global mean (Trenberth, Fasullo, and Kiehl, 2009; Wild et al., 2015; Tian et al., 2023). However, during the polar night when solar shortwave radiation is absent, the cooling effect of clouds and aerosols, arising from the scattering of solar radiation, becomes negligible (Cox et al., 2015). Therefore, LWD from clouds and aerosols assumes greater significance, particularly in maintaining the Arctic energy balance (Cox et al., 2015; Serreze and Barry, 2011; Lenaerts et al., 2017; Ebell et al., 2020). Compared with LWD from clouds (50 - 100 Wm^{-2} (Cox et al., 2015; Serreze and Barry, 2011; Lenaerts et al., 2017; Ebell et al., 2020)), previous studies show that the LWD caused by aerosols in dry condition is usually lower than 10 Wm^{-2} (Spänkuch, Döhler, and Güldner, 2000; Markowicz et al., 2003; Vogelmann et al., 2003; Lohmann et al., 2010). Dry aerosol particles contribute very limited LWD to the Arctic climate. However, LWD in the transition state (wet aerosols) between dry aerosols and cloud droplets is rarely mentioned.

Aerosols in the atmosphere, including sea salt and sulfates, possess hygroscopic properties, allowing them to absorb water vapor and undergo wet growth (Winkler, 1973). This process, known as aerosol wet growth, is accompanied by an increase in LWD (Mauritsen et al., 2011). The magnitude of this increase is influenced by factors such as aerosol composition, and ambient relative humidity (RH) (Peng, Chen, and Tang, 2022). Notably, the deliquescence point, at which hygroscopic aerosols abruptly increase in size, is a critical threshold determined by ambient RH (Tang and Munkelwitz, 1993; Winkler, 1973). For example, the sea salt and sulfate aerosols in this study have deliquescence points of about 75% and 85%, respectively (Peng, Chen, and Tang, 2022). This means that when the ambient humidity increases to 75%, the dry sea salt aerosol particles can absorb water vapor in the atmosphere and become larger. If the ambient humidity continues to increase, the sea salt wet particles will continue to absorb water and become sea salt solution droplets (still belonging to aerosols). This is the wet growth process of sea salt aerosols. Recent studies have shown an increase in Arctic water vapor content, attributed to enhanced poleward transport facilitated by atmospheric river pathways (Sato et al., 2022; Thandlam, Rutgersson, and Sahlee, 2022; Bresson et al., 2022). Moreover, sea salt aerosols have been identified as dominant contributors to Arctic aerosol composition during the winter season (Huang and Jaeglé, 2017; Kirpes et al., 2018). Therefore, the rise in coarse-mode aerosols, primarily originating from sea spray, and the increase of RH in the Arctic underscore the need to investigate the potential impact of aerosols on LWD and Arctic warming during their wet growth process (Heslin-Rees et al., 2020; Pernov et al., 2022).

Given the complex interplay between aerosols (especially aerosol composition), RH, and LWD, understanding the radiative effects of aerosol wet growth is crucial for understanding the role of aerosols in AA, particularly during the polar night. Considering the various factors contributing to atmospheric LWD, such as greenhouse gases, clouds, and aerosols, this study aims to explore the extra LWD introduced during aerosol wet growth. To achieve this, both model simulations and observational data will be utilized, defining the resulting additional LWD from aerosols as the Aerosol Infrared Radiation Effect (ARE). The following section provides an

overview of the datasets utilized, including Fourier-transform infrared spectroscopy (FTS) and Baseline Surface Radiation Network (BSRN) measurements. The FTS plays a crucial role in elucidating the relationship between aerosol composition and ARE, offering detailed insights into aerosol composition while quantifying ARE. However, the ARE from the FTS is the ARE within the atmospheric window region (AW, 690 - 1390 cm^{-1}; 7 - 14 µm). Conversely, the BSRN provides ARE data across the entire mid-infrared region (4.5 - 42 µm, (Maturilli, 2020)) but lacks the capability to characterize aerosol composition. Each dataset presents unique advantages and limitations. Furthermore, it is essential to account for the influences of other radiative sources, such as clouds and greenhouse gases, to accurately assess ARE. Therefore, the methodologies employed to derive ARE from LWD measurements (eliminating contribution from clouds and GHGs) are also presented in detail.

3.5.1 Extra Data Used in "ARE"

All observations and model simulations in this study are conducted in Ny-Ålesund (78.9 °N,11.5 °E), the world's northernmost year-round research station, facilitating and hosting research projects and long-term observation series. The surface radiation measurements, radiosonde launches, and all measurements by cloud radar, microwave radiometer, ceilometer, and FTS, are operated at the Atmosphere Observatory of the AWIPEV research base that is run jointly by the German Alfred Wegener Institute and the French Polar Institute.

Clouds and Aerosols Signals from Cloudnet

In order to identify cloud cases, the Cloudnet classification product is used (Illingworth et al., 2007). Cloudnet is operationally applied to the AWIPEV measurement (Nomokonova, Ritter, and Ebell, 2019; Ebell, Schnitt, and Krobot, 2023). Within the Cloudnet processing, information from a cloud radar, ceilometer, microwave radiometer and output from a numerical weather prediction model is combined and the backscattered signals by the radar and ceilometer classified in terms of the occurrence of "Aerosol & insects", "Insects", "Aerosols", "Melting & droplets", "Ice & droplets", "Ice", "Drizzle & droplets", "Drizzle or rain" and "Droplets". The classification profiles have a vertical resolution of 20 m and extend from 120 m to about 11 km height above the surface. The Cloudnet data used in this study are measured from 2017 to 2022, with temporal resolution of 30s. The application of this data to the FTS and BSRN is slightly different, and the specific methods are given in the respective sections (Sec.3.5.2 for FTS and Sec.3.5.2 for BSRN).

LWD in Atmospheric Window Measured from FTS

A Fourier Transform spectrometer, called NYAEM-FTS, for measuring down-welling emission in the thermal infrared was installed in Ny-Ålesund in summer 2019. The NYAEM-FTS consists of a Bruker Vertex 80 Fourier Transform Spectrometer, a SR800 blackbody, an automatically operated gold mirror to select the radiation source and an automatically operated hutch with shields the instrument from the environment.

It is situated in a temperature stabilized laboratory, at about 21 - 25 °C. The beamsplitter is a KBr beam splitter and the detector is an extended Mercury Cadmium Telluride (MCT) detector.

Therefore, the infrared spectra are measured by FTS. Since the infrared emission of aerosols is primarily concentrated in the atmospheric window (Ji et al., 2023), integrating the spectrum within this region provides the longwave radiation (LWD) data from the FTS. The FTS spectra used in this study are measured from 2019 to 2022. More details of emission FTS (NYAEM-FTS) can be found in Ji et al. (2023). The method of how to obtain the ARE from measured spectra is given in Sec.3.5.2.

LWD in Mid-infrared Range from BSRN

The radiation measurements, i.e. the LWD, at station Ny-Ålesund is from Maturilli (2020). The Baseline Surface Radiation Network (BSRN) is a global network of high-quality ground-based stations established to observe and record solar and atmospheric radiation, including direct solar radiation tracked using a pyrheliometer (Eppley NIP) on a solar tracker, diffuse, global, and reflected shortwave radiation measured by pyranometers (Kipp and Zonen CMP22), and upwelling and downwelling longwave radiation detected by pyrgeometers (Eppley PIR). All data are quality controlled. LWD ((4.5 - 42 μm)) measurements from BSRN are expected to have an uncertainty within $\pm$ 5 Wm^{-2} (Maturilli, Herber, and König-Langlo, 2015). The LWD data used in this study are measured in every winter (DJF) from 2017 to 2022, with temporal resolution of 1 min.

Water vapor Profiles from Radiosonde

As we mentioned before, LWD measured by BSRN includes the emitted radiation of GHGs, clouds and aerosols. Cloud cases can be identified by Cloudnet, while the contribution from GHGs should also be considered. The vertical profiles of temperature, pressure and RH (water vapor) are used from the radiosonde measurements (Maturilli and Dünschede, 2023). The Alfred Wegener Institute (AWI) has been performing radiosonde measurements at Ny-Ålesund since 1991, with regular daily 12 UTC launches since 1992. In order to extent this existing homogenized data record, the 2017 to 2022 Ny-Ålesund radiosonde data processed by the Global Climate Observing System (GCOS) Reference Upper-Air Network (GRUAN) have been interpolated on the according height resolution. The combined uncertainty given by the manufacturer is 4% for RH. The whole time period for a radiosonde ascent from the surface to 30 km takes about 90 minutes. The data from radiosonde in this study are measured in every winter (DJF) from 2017 to 2022, with temporal resolution of 1d.

3.5.2 Methods Applied in "ARE"

ARE_{AW} from FTS

The downwelling radiance emitted by the atmosphere, including aerosols or clouds, can be measured using FTS. For Emission FTS, the waveband that is sensitive to aerosols is the atmospheric window region. To distinguish the LWD and ARE measured by FTS (7 - 14 μm) from the later mentioned LWD and ARE from BSRN (4.5

- 42 µm), here we use the subscript 'AW' to denote the quantity measured by the FTS. Note that AW is part of the mid-infrared band (BSRN), so the radiation measured by FTS is not comparable to the radiation measured by BSRN. Additionally, in the atmospheric window, the contribution from greenhouse gases (GHGs) is negligible, making the cloud signal the only factor that needs consideration. The FTS conducts vertical observations, so ensuring cloud-free conditions vertically is sufficient. Specifically, when Cloudnet indicates only an aerosol signal in the total atmospheric column, the spectra from the FTS observations for that time period will be used, while spectra from other periods will be discarded. Besides, Cloudnet provides aerosol height information, then RH at the aerosol layer is obtained from ERA5 hourly data on pressure levels (Hersbach et al., 2018).

In order to calculate $\mathrm{ARE}_{\mathrm{AW}}$, the radiance measured by emission FTS has to be first considered to the broadband $\mathrm{LWD}_{\mathrm{AW}}$. The ARE in atmosphere window is given by:

$$\mathrm{ARE}_{\mathrm{AW}} = \mathrm{LWD}_{\mathrm{AW}} - \mathrm{LWD}_{\mathrm{AW\_clear}} \tag{3.23}$$

where $\mathrm{LWD}_{\mathrm{AW}}$ is the calculated LWD in AW range with the measurements of emission spectra by FTS; $\mathrm{LWD}_{\mathrm{AW\_clear}}$ is the emission flux from a clear atmosphere, which can be calculated using the LBLDIS model or observed by FTS under the ideal conditions of an environment without aerosols and clouds. Here, LBLDIS model simulations under clear sky is used. The equation for $\mathrm{LWD}_{\mathrm{AW}}$, from the spectral radiance I (in $\mathrm{Wm^{-2}cm^{-1}sr^{-1}}$) is given as follows:

$$\mathrm{LWD}_{\mathrm{AW}} = \iiint I(v, \mu, \phi)\mu d\mu d\phi dv \tag{3.24}$$

where I is the radiance, μ is the cosine of the zenith angle, ϕ is the azimuthal angle, and v is the wave number. Integrating the radiance over both the hemisphere and the wave number yields the $\mathrm{LWD}_{\mathrm{AW}}$. The wave number for atmospheric window (AW) ranges from 690 to 1390 $\mathrm{cm^{-1}}$ (7 - 14 µm) (Cox et al., 2015).

If the azimuthal symmetry and isotropic (homogenuity) assumptions are made, Equation (3.24) can be simplified to:

$$\mathrm{LWD}_{\mathrm{AW}} = 2\pi \iint I(v, \mu)\mu d\mu dv \tag{3.25}$$

According to Cox, Walden, and Rowe (2012), the radiation from thick clouds is isotropic, while that from thin clouds is not. The isotropic assumption does not apply to radiance emitted by aerosols as well. Therefore, similar to the method used in Cox, Walden, and Rowe (2012), the relationship between radiance and $\mathrm{LWD}_{\mathrm{AW}}$ is calculated using an exponential function assumption of radiance dependence on μ , as follows:

$$\int_{690cm^{-1}}^{1390cm^{-1}} I(v, \mu)dv = \int_{690cm^{-1}}^{1390cm^{-1}} I(v, \mu = 1) \cdot (a \cdot e^{-b \cdot \mu} + c)dv \tag{3.26}$$

For a more concise expression, we here abbreviate the wave number integral of radiance $\int_{690cm^{-1}}^{1390cm^{-1}} I(v, \mu = 1)dv$ as II_{AW}. Therefore, the final flux calculation function

could be written as follows:

$$\mathrm{LWD_{AW}} = 2\pi II_{\mathrm{AW}} \cdot \int_0^1 (a \cdot e^{-b\cdot\mu} + c)\mu d\mu \tag{3.27}$$

where a, b, and c are the fitted coefficients, which are given in appendix .A.

For isotropic assumptions, such as thick clouds, the integral of the second part will be a constant value, allowing the Equation (3.27) to be simplified to $\mathrm{LWD_{AW}} = \pi II_{\mathrm{AW}}$. In the case of non-isotropic emissions, such as aerosols, a correction coefficient C should be considered, and the Equation (3.27) is rewritten as follows:

$$\mathrm{LWD_{AW}} = C \cdot \pi \cdot II_{\mathrm{AW}}, \text{with } C = 2 \cdot \int_0^1 (a \cdot e^{-b\cdot\mu} + c)\mu d\mu. \tag{3.28}$$

C is the correction coefficient for non-isotropic emissions, which is variable for different emissions, such as aerosols, atmosphere in clear day and thin clouds. This correction coefficient C has been determined by LBLDIS model simulations and a value of 1.35 $\pm$0.05 for aerosols in the atmospheric window. The method of how to get this correction coefficient is given in Appendix .A.

The error of spectra measured by FTS is usually less than 1 $\mathrm{mWm^{-2}cm^{-1}sr^{-1}}$ in AW region (Ji et al., 2023), the uncertainty of the correction coefficient for non-isotropic emission from aerosol is about $\pm$ 0.05 here, therefore, the theoretical error of $\mathrm{LWD_{AW}}$ from FTS is $\sqrt{(\frac{\partial \mathrm{LWD_{AW}}}{\partial II_{\mathrm{AW}}} \cdot \Delta II_{\mathrm{AW}})^2 + (\frac{\partial \mathrm{LWD_{AW}}}{\partial C} \cdot \Delta C)^2}$, about 0.550 $\mathrm{Wm^{-2}}$.

$\mathrm{ARE_{AW}}$ from LBLDIS Model Simulation

To analyse the key parameters affecting the aerosol infrared radiation, we perform model simulations also in the atmospheric window. When considering model simulation of downwelling emission from the atmosphere, two radiative transfer models are coupled and used in this case, one is the Line-by-Line Radiative Transfer Model (LBLRTM) (Clough et al., 2005) for the gaseous contribution, another is the DIScrete Ordinate Radiative Transfer model (DISORT) (Stamnes et al., 1988) for calculation of water droplets and aerosol particles. The coupled model is called LBLDIS (Turner, 2005). This radiative transfer model is also used as a forward model in aerosol composition retrieval algorithm described in Ji et al. (2023).

The $\mathrm{ARE_{AW}}$ calculation method from simulated spectra using the LBLDIS model is similar to the method mentioned in Sec.3.5.2. ARE of two aerosols, sea salt and sulfate (Ammonium sulfate), are simulated by radiative transfer model (LBLDIS). Since the model setups for sea salt and sulfate are similar, only the parameters in the model for sea salt are described in detail here. Usually, aerosol sizes in the Arctic region are often below 1 µm, according to the measurements of aerosol size distribution in the Arctic (Asmi et al., 2016; Park et al., 2020; Boyer et al., 2022). Weinbruch et al. (2012) found that sea salt particles were most abundant in particles larger than 0.5 µm. Therefore, in dry conditions, it is assumed that the size of sea salt is fixed at 1 µm and has the shape of a sphere (Ji et al., 2023). The aerosol size distribution is assumed to be a uniform distribution. All aerosols are fixed at a height of 1000 meters above the ground, which means the temperature of aerosol layer is fixed.

Several model simulations are run under various RH conditions (65% as dry condition, 75% - 95% as wet conditions), with various aerosol number densities (50 cm^{-3} - 5000 cm^{-3}). As for sulfate, the size is assumed to be smaller (Pernov et al., 2022), 0.4 µm in model simulations in dry condition, and other settings are the same as those for the sea salt case. The input data for LBLDIS includes profiles of temperature, pressure, and humidity, which are sourced from ERA5 (Hersbach et al., 2018).

ARE in the Mid-infrared Range from BSRN

The measurement of LWD (4.5 - 42 µm) from the atmosphere is obtained from the BSRN. Since we are only focusing on the infrared radiative effects of aerosols (ARE) in this study, the radiation from clouds as well as GHGs needs to be eliminated.

To identify clouds conditions, we use the data from the Cloudnet to eliminate the BSRN observations with cloud cases. As we mentioned in Sec.3.5.1, there are several targets in the "Classification" product of Cloudnet. Within the altitude range (0 – 12 km) of the "Classification" product, an aerosol-only situation is selected when only "Aerosols" are present in all of the above targets. Then observations of the BSRN are selected that correspond to these times, resulting in aerosol-only BSRN observations. Note that, the LWD from BSRN is the downward radiation of the entire hemispheric atmosphere. This means that simply being cloud-free vertically is not enough to ensure that the entire sky is cloud-free. As the Radiosonde profile measurement starts at around 12:00 and lasts for about 90 minutes, the cloud-free time period is ensured to 3 hours around 12:00 (10:30 to 13:30).

Water vapor, the most important greenhouse gases (GHGs), contributes more significantly to LWD relative to other GHGs (Easterbrook, 2016). In addition, the water vapor content of the atmosphere is much more variable, which means that we need to remove the effect of water vapor in calculating ARE. Therefore, the next step is to eliminate the contribution of gases in the atmosphere to the LWD:

$$\mathrm{ARE} = \mathrm{LWD}_{\text{aerosol-only}} - \mathrm{LWD}_{\text{clear}} \tag{3.29}$$

where $\mathrm{LWD}_{\text{aerosol-only}}$ means LWD from BSRN under aerosol-only cases; $\mathrm{LWD}_{\text{clear}}$ means the infrared radiation flux of clear sky, which is given by the radiative transfer model simulation. Since LBLDIS is mainly used in the AW region, the radiative transfer model used to calculate $\mathrm{LWD}_{\text{clear}}$ in mid-infrared range (4.5 - 42 µm) is the SBDART (Santa Barbara DISORT Atmospheric Radiative Transfer, (Ricchiazzi et al., 1998)), a versatile software tool designed to calculate plane-parallel radiative transfer within the Earth's atmosphere, covering the entire mid-infrared waveband. Since we only need to calculate radiation under a clean atmosphere, the temperature, pressure, and humidity profiles from the sounding data act as inputs to SBDART to obtain $\mathrm{LWD}_{\text{clear}}$, as shown in Fig.3.6

To make the above-mentioned cloud-free data filtering and water vapor elimination process clearer, Fig.3.6 shows the schematic diagram of this data filtering and processing:

1. Firstly, with the help of Cloudnet Classification dataset, the LWD measured by BSRN during the cloud-free time period is selected, called $\mathrm{LWD}_{\text{aero-only}}$;

2. Secondly, the sounding data (Temperature, pressure, altitude and RH vertical profiles) are used as input data into SBDART for the clear sky LWD simulation, called LWD_{clear};

3. Following Equation (3.29), ARE is calculated from the difference between $LWD_{aero\text{-}only}$ and LWD_{clear}.

Note that the time resolution of the $LWD_{aero\text{-}only}$ data is 1 minute, while the time resolution of the sounding profiles is once per day, with each ground to high altitude (about 30 km) observation period lasting about 90 minutes. Therefore, the $LWD_{aero\text{-}only}$ measurements are averaged over the sounding time period (10:30 UTC - 13:30 UTC) to represent the ARE at that sounding time.

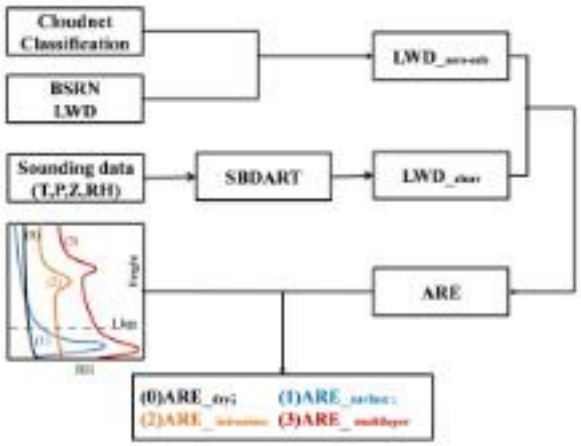

FIGURE 3.6: Schematic diagram of data filtering and processing. The "Classification" product of Cloudnet is applied to BSRN LWD measurements in cloud-free data filtering, see Sec.3.5.2. Using sounding data, LWD_{clear} is simulated by SBDART. The difference between $LWD_{aero\text{-}only}$ and LWD_{clear} is the ARE (see Equation .3.29). Finally, based on the profiles of water vapor from sounding data, ARE is divided into four scenarios based on the difference in the line shape of the RH profiles: ARE_{dry}, $ARE_{surface}$, $ARE_{intrusion}$ and $ARE_{multilayer}$.

In addition, RH is a key parameter in the aerosol wet growth process and there is no additional data indicating at which altitude hygroscopic aerosols are located. On one hand, air masses from the mid-latitudes transport both moisture and aerosols to the Arctic. On the other hand, aerosols are dispersed throughout the atmosphere and become activated at particular altitudes where the relative humidity reaches their deliquescence point. Therefore, we assume here that the peaks in the RH profiles, meaning the intrusion of water vapor, is the RH of the activated aerosols. Then, we classify the ARE into four scenarios based on the difference in the line shape of the RH profiles: ARE_{dry}, $ARE_{surface}$, $ARE_{intrusion}$ and $ARE_{multilayer}$. ARE_{dry} means that the entire atmosphere is in a dry state (RH < 60%); $ARE_{surface}$ means that there is a layer of high humidity (RH > 60%) near the ground (< 1 km); $ARE_{intrusion}$ represents the situation with a layer of high humidity intrusion (RH > 60%) at high altitude (> 1 km). $ARE_{multilayer}$ is the case that the atmosphere has multiple layers (2 layers in this study, one below 1 km and one above 1 km) of high humidity (RH > 60%). Then the peaks of the RH profiles can be regarded as the RH values at the level where the activated aerosols are located within each scenarios.

In summary, using these filters, a total of 100 cases are available, 15 cases in ARE_{dry}, 41 cases in $ARE_{surface}$, 5 cases in $ARE_{intrusion}$, and 39 cases in $ARE_{multilayer}$. The RH values are the peaks of the RH profiles according to different scenarios.

3.5.3 Summary of "ARE"

We usually consider the infrared radiation effect of aerosols to be small. This view needs to be updated when aerosol wet growth is considered. In the study of the infrared radiative effect of aerosols, we have also developed a coupling method between different observational datasets (BSRN, Cloudnet and Radiosonde measurement), and the results of the FTS observations will be validated against those of the BSRN and Cloudnet. This will provide the infrared radiative effect of wet growth aerosols.

3.6 Arctic Aerosol Transportation Pathways

Aerosols play a critical role in feedback mechanisms associated with Arctic Amplification, particularly through surface albedo and cloud feedback (Bony et al., 2006; Soden and Held, 2006; Stone et al., 2007; Taylor et al., 2013; Graversen, Langen, and Mauritsen, 2014; Philipp, Stengel, and Ahrens, 2020). These aerosols originate both within the Arctic and from distant regions, transported via atmospheric pathways (Schmale, Zieger, and Ekman, 2021). Recent research has underscored the significance of the eastern Atlantic pathway, which enables the fast transport of African dust aerosols to the Arctic (Francis et al., 2018; Francis et al., 2022) . This pathway, known as the Rapid Pathway (RP), significantly influences Arctic dust aerosol loads.

The RP is particularly crucial for the transport of large-sized aerosols. Given the varied lifetimes of aerosols, which can range from several days to months (Kristiansen et al., 2015), larger aerosols tend to settle more quickly due to heavy gravitational effects (Wake and Brown, 1991; Chao and Wan, 2006), making rapid transport essential. Dust aerosol is a major contributor of coarse particles in the atmosphere Adebiyi et al., 2023. Arctic dust aerosol primarily originates from natural sources such as desert regions, with approximately 65% from Africa (Sahara desert), 22% from Asian deserts, and 13% from other deserts (Kok et al., 2021; Breider et al., 2014). Arctic dust aerosol concentrations peak in spring when long-range transport from Africa and Asia is most efficient, while local sources become more prominent in autumn (Groot Zwaaftink et al., 2016b).

The transport of African dust aerosol to the Arctic occurs via four main pathways, including routes across North Europe, the Atlantic Ocean around the Azores High, Russia from Asian deserts, and the eastern Atlantic (Francis et al., 2018). Varga et al. (2021) analyzed 15 Sahara Desert dust aerosol intrusion events that reached the Arctic, 10 of which occurred between 2016 and 2020, which indicates the contribution of African region on Arctic dust load has become increasingly important in recent years. Furthermore, dust particles play a significant role in ice cloud nucleation (IN) (DeMott et al., 2003), highlighting their importance in studies of Arctic Amplification. However, existing studies have predominantly focused on short time events (several days) and have not thoroughly described the RP's characteristics, including its seasonal and inter-annual variations.

This part of work aims to investigate the inter-annual changes in the RP for African dust aerosol transport to the Arctic, enhancing our understanding of potential shifts in wind field due to global warming. We employ GEOS-Chem model simulations to provide a detailed description of the RP, revealing that African dust can reach the Arctic in about one week. Secondly, we use dust aerosol optical depth (AOD) data from the MERRA-2 Reanalysis dataset to examine the RP's inter-annual variability from 1980 to 2022 for different months. Our findings indicate a significant shift in dust transport pathways post-2000, with an increased transport via the central North Atlantic (RP region) and minimal changes in the European land transport route. ERA5 wind field data further reveal significant positive anomalies in poleward winds over the North Atlantic in March and April post-2000, facilitating northward dust transport through the RP, while negative wind anomalies over Europe suggest a diminished role for the European pathway in Arctic dust transport.

3.6.1 Dust Simulation by GEOS-Chem

Model simulations restrict dust emissions solely to the African region, with emissions from other areas set to zero. This setup allows for the analysis of the proportion of African-origin dust entering the Arctic via the RP, facilitating the study of the pathway's significance in dust transport. We employ GEOS-Chem model simulations to quantify the Arctic aerosol load of dust originating from Africa via the RP. GEOS-Chem is a global 3-D atmospheric chemistry model driven by meteorological data from the Goddard Earth Observing System (GEOS) of NASA's Global Modeling and Assimilation Office Bey et al., 2001. In this study, we use version 13.4.0 of GEOS-Chem, driven by meteorological data from the MERRA-2 Gelaro et al., 2017, with a spatial resolution of $2^\circ \times 2.5^\circ$ and 47 vertical levels for global simulations. The aerosol-only module is used for dust aerosol simulation, and the aerosol simulations were conducted from January 1, 2021, to May 31, 2022. The model simulation for 2021 is treated as spin-up run, and the data used in this study is the January 1, 2022, to May 31, 2022.

The dust aerosol simulation employs an online approach for dust emission calculation, using the Dust Entrainment and Deposition (DEAD) mobilization scheme Zender, Bian, and Newman, 2003, augmented by the source function employed in the Goddard Chemistry Aerosol Radiation and Transport (GOCART) model Chin et al., 2004; Ginoux et al., 2001. To isolate the transport of dust originating in Africa, we conduct an Africa-only dust simulation, confining dust emissions to a zonal range of 20°W - 54°E and a meridional range of 37°S - 40°N, representing the African region. Since the dust is only emitted in the African region in the model, the increase in dust concentration in the Arctic should correlate with that in the emission area, with a certain time lag. Therefore, we analyze the correlation between the Arctic dust AOD and source region dust AOD with a time lag. The number of lag days corresponding to the maximum correlation coefficient represents the approximate transport time of dust from the source region to the Arctic region.

3.6.2 Dust AOD from MERRA-2

The presence of dust aerosol in the Eastern Atlantic and Arctic regions is connected to the status of the RP. Using dust aerosol optical depth (AOD) data from the MERRA-2 Reanalysis dataset Gelaro et al., 2017, we examined the inter-annual variability of

the RP. Annual and monthly fluctuations in dust emissions from source regions introduce variability that direct time series analyses cannot account for. To address this, we use the maximum value of dust AOD in the source emission region for each month to scale the dust AOD across that longitude to obtain the normalized dust AOD. In other words, the scaled dust AOD assumes constant source emissions at a value of 1, effectively eliminating the impact of variable emissions and allowing for a clearer analysis of dust transport dynamics to the Arctic.

3.6.3 Wind Field from ERA5

The AOD of dust derived from the MERRA-2 Reanalysis reflects global dust emissions, not only African emissions. Hence, assessing variations in the wind field from Africa to the Arctic via the RP provides a more nuanced understanding of African dust influx into the Arctic region. The ERA5 monthly averaged dataset provides comprehensive atmospheric data across various pressure levels, spanning from 1940 to the present (Hersbach et al., 2023). In this study, we utilize monthly averaged wind field data at 700 hPa from 1980 to 2022. Typically, the u-component of wind predominates in monthly averaged wind fields compared to the v-component, owing to the influence of large-scale climatology circulation patterns such as the Iceland Low in high latitudes, prevailing westerlies in mid-latitudes, and the Azores High in subtropical regions. As the RP is driven by synoptic-scale systems lasting only a few days to weeks, fluctuations in the u and v components of wind due to synoptic-scale systems are more pronounced in the v component, hereafter referred to as the "poleward wind."

Chapter 4

Results

4.1 Aerosol Composition Retrieved Using FTS

4.1.1 Artificial Spectra from LBLDIS

When considering down-welling emission from the atmosphere on a clear day, the main contribution to emission in the thermal infrared band are from the greenhouse gases, i.e. CO_2, H_2O, N_2O, CO, CH_4 and O_3. If there is a cloud or aerosol layer, its broad band emissions can be observed as well (compare Fig. 4.1).

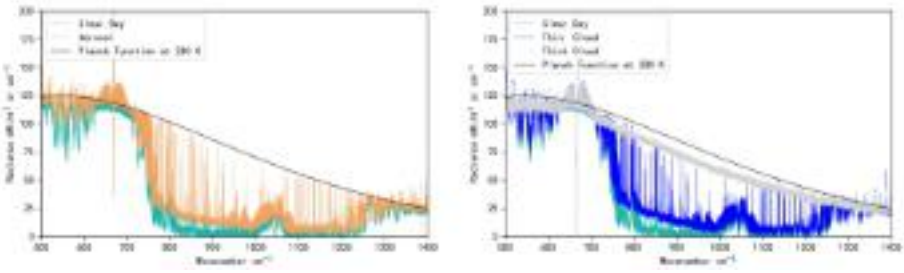

FIGURE 4.1: Four different emission spectra measured by NYAEM-FTS in clear sky (green), aerosol (yellow, left), thin cloud (blue, right) and thick cloud (gray, right) event respectively. The radiance calculated using Planck function at 280 K (black line) is presented in this figure. Note: the emission around 650 cm^{-1} originates in ambient CO_2 from the laboratory air, this signal is mentioned before (see Sec.3.2.2).

Several thermal infrared emission spectra from the LBLDIS model are shown in Fig. 4.2. Under the same number density, different aerosol types exhibit unique characteristics in the infrared emission spectra, shown in Fig. 4.2a. Among those aerosols, the radiance emitted from sea salt is lowest, due to its smallest light absorbing capability compared to other aerosols. When the number density is fixed in model simulation, the radiance from sea salt increases with the size of particles (Fig. 4.2b). Using the same number density, the radiance from sea salt with the same size as other aerosols is significantly lower; only when sea salt has a large particle size compared to the other aerosols, are the radiances comparable. Figure 4.2c shows

the thermal infrared emission spectra of atmospheric gases (clear sky) and different aerosols within atmosphere. According to Fig. 4.2c, in some wavebands, the gas emission dominates over the aerosol signal. Those bands are not considered for the retrieval, e.g. CO_2 in 640 - 690 cm^{-1} and O_3 in 1000 - 1100 cm^{-1}. Aerosol windows (compare Tab. 3.1) are chosen in the region in 500 - 600 cm^{-1}, 800 - 1000 cm^{-1}, and 1100 - 1200 cm^{-1}, which are selected as retrieval micro-windows (vertical lines in Fig. 4.2c). Those micro windows are similar with that in Richter et al. (2022) in cloud parameters retrieval using a similar instrument. The spectra in Fig. 4.2d are shown in the form of the difference between the aerosol and clear sky in those micro-windows . Based on that, the emission spectra in aerosol events are different from each other, which means the emission from aerosols can be measured and aerosol types can be retrieved using the emission FTS. The reason for avoiding the gas emissions is the dependency of the gas emissions on the temperature distribution in the atmosphere.

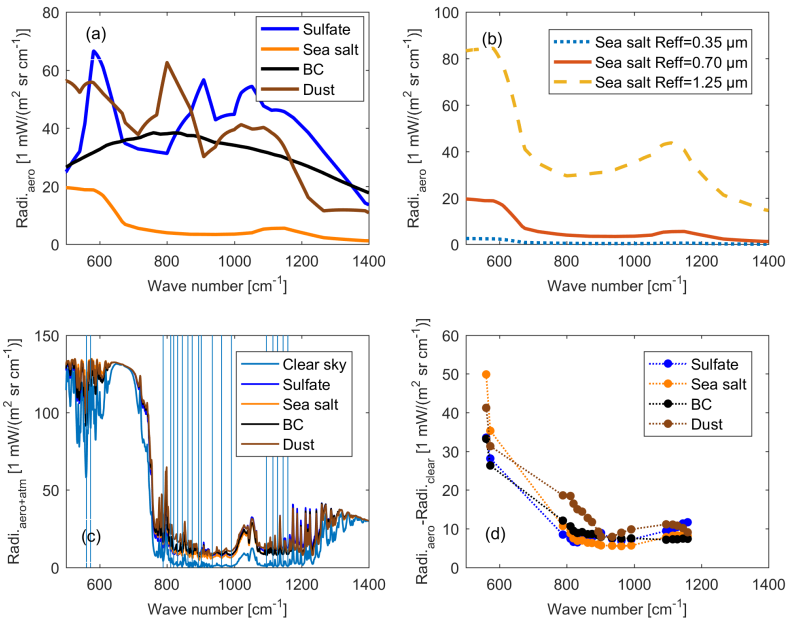

FIGURE 4.2: The emission spectra of small aerosol particles (dust in brown, sulfate in blue, sea salt in orange, BC in black) with Reff = 0.35 μm and number density = 2000 cm^{-3} (a); The emission spectra of sea salt with different particle sizes (b); The emission spectra of aerosols ($AOD_{900\ cm^{-1}}$ = 0.1) with atmosphere gases and clear sky case (c); The difference between total emission spectra of aerosol and clear sky case in micro windows (d). The vertical blue lines in (c) show the mid-values of micro windows selected for retrieval. The emission spectra are simulated from LBLDIS with the resolution of 1 cm^{-1}.

4.1.2 Sensitivity Study

In order to investigate the precision of the retrieved values, artificial spectra simulated from LBLDIS are used to explore the performance of TCWRET-V2 in the retrieval of aerosol types. Artificial spectra with preset values of AOD as well as R_{eff} are created using LBLDIS and then act as measured spectra retrieved by the algorithm. Specifically, we assume that all particles are concentrated on a single level,

2000 m above surface ground. The AOD's of sea salt, sulfate, dust and BC are set 0.1, respectively, with R_{eff} of 0.7 µm. The retrieval results suffer from several uncertainty sources:

- Uncertainty of the aerosol height, which is similar to the error of aerosol layer temperature. In this study, the aerosol height is given by Lidar measurement.
- Uncertainty of the humidity profile has a significant signal on the far-infrared emission spectrum, at about 1500 - 2000 cm^{-1}. Thus, the water vapor profile could change the radiance of emission spectrum, which might affect the results of retrieval.
- Calibration uncertainty in the measured spectra is also an important uncertainty in the retrieval, which could be caused by misreading of the blackbody temperature. In this study, the total power calibration method (Revercomb et al., 1988) is used to calibrate the spectra. Assuming the accuracy of the blackbody temperature is $\Delta T_{BB} = \pm 1K$. The propagation of this error into radiance is

$$\Delta L = \sqrt{(\frac{\partial L_{atm}}{\partial T_{BB}} \cdot 1K)^2} \tag{4.1}$$

  According to Richter et al. (2022), the partial derivative $\frac{\partial L_{atm}}{\partial T_{BB}}$ can be estimated using:

$$L_{atm} = B(T_{amb}) + 0.2 \cdot (B(T_{hot}) - B(T_{amb})) \tag{4.2}$$

  where $B(T_{hot})$ means hot blackbody temperature and $B(T_{amb})$ means surface air temperature.
  With $T_{hot} = 100\ ^\circ C$ and $T_{amb} = 0\ ^\circ C$, $\frac{\partial L_{atm}}{\partial T_{BB}} \cdot 1K = 0.41\ mWsr^{-1}m^{-2}cm^{-1}$ is an average for the spectral interval between 500 and 2000 cm^{-1}.
- Measurement uncertainty. The noise on the spectrum is assumed to be white in space and time.
- Database uncertainty could be caused by uncertainty of aerosol complex refractive index. Both the real and imaginary part could have an influence on the accuracy of aerosol scattering properties look-up tables, as we mentioned in Sec. 3.3.2.

The artificial spectra with modifications are performed according Tab. 4.1. Compared with preset values, one can then compute the difference between retrieved values with preset values by perturbing each parameter.

TABLE 4.1: Parameter errors and modifications in artificial spectra

Parameters	Modifications
Height of aerosol	+10% (200 m)
Water vapor profiles	-10%
Calibration error	+1 mW/sr*m2*cm-1
Measurement error	Normally distributed noise with mean value of 0 and variance of 1
Complex refractive index (real part)	-10%
Complex refractive index (imaginary part)	-10%

4.1.3 Uncertainty Study

As we mentioned in Sec. 4.1.2, the artificial spectra are given by forward model with preset values (compare Tab. 4.1). The retrieved results of those artificial spectra can be obtained by using the artificial spectra as the observed spectra in the retrieval algorithm. The difference between retrieved values with preset values by perturbing each parameter by 10% (see Tab.4.1) is shown in Fig. 4.3.

Fig. 4.3 shows that the original case, without any modifications is close to the preset values. The difference of AOD retrieved in the original case with preset values are less than 0.005 at 900 cm^{-1}, leading to convincing results using this retrieval algorithm. Noise in the measurements and water vapor profiles have small effects on the retrieval, causing about 0.0006 in AOD retrieval error. The most important parameter is the database error, caused by the uncertainty of the complex refractive index. A decrease of 10% in the real part of the complex refractive index will cause about 7% positive errors in AOD of sulfate, dust and BC, except for AOD of sea salt, which shows 18% negative error. While the 10% decrease of the imaginary part of the complex refractive index will cause about 4% negative errors in AOD of sulfate, dust and BC and 1% negative error in AOD of sea salt. Following the databases errors, the second most important error is the calibration error, e.g. 1 K misreading of the temperature of the blackbody will cause a change in radiance of about 0.47 $mWsr^{-1}m^{-2}cm^{-1}$. An offset of radiance by 1 $mWsr^{-1}m^{-2}cm^{-1}$ causes an error in all aerosol AOD retrieval of about 4% overestimation in the results. The temperature error of the aerosol layer is the third most important effects in the aerosol AOD retrieval.

Organic carbon (OC) is one of the major components in tropospheric aerosols. It is not considered because there are no data of the complex refractive index in the infrared waveband of OC. There are also many types of OC, each of them has a different spectral signature. The missing database for OC can be considered as an error in the scattering database. As we mentioned before, a 10% database error causes up to 18% AOD retrieval error. Therefore, if the OC does exist, but due to the missing database will cause up to 18% error in the retrieval of the other aerosol AOD.

In conclusion, when aerosol is present in the atmosphere, the emission from aerosol can be measured by FTS. According to forward model simulations, different aerosol types show their own features. Using artificial spectra with preset values, error estimations caused by the retrieval could be calculated.

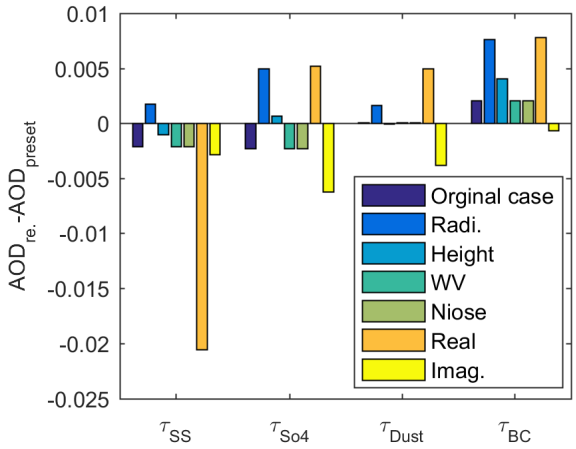

FIGURE 4.3: The difference between retrieved AOD in original case and several possible perturbing scenery (compare Table 4.1) with preset values.

4.1.4 Aerosol-only Retrieval

On the 10th of June 2020 there was an aerosol event in Ny-Ålesund (compare Fig. 4.4, showing the aerosol distribution derived using the KARL Lidar). This aerosol event is chosen as our aerosol-only case. Figure 4.5 presents the four different aerosol classes and cloud based on the Lidar classification method (compare Sec.3.3.4). During this day, aerosols are mainly distributed below 1500 m (compare Fig. 4.4). From 7:00 to 11:00, the thickness of a coarse aerosol layer (dense aerosol in Lidar classification method in Sec. 3.3.4) near the surface decreases, while in the afternoon, this aerosol load increases and splits into two layers, one near the surface and another, activated aerosol, appears at the height of about 500 m. At around 8:00 clouds are present in a height of 3500 m, which has been screened out in the aerosol-only FTS retrieval.

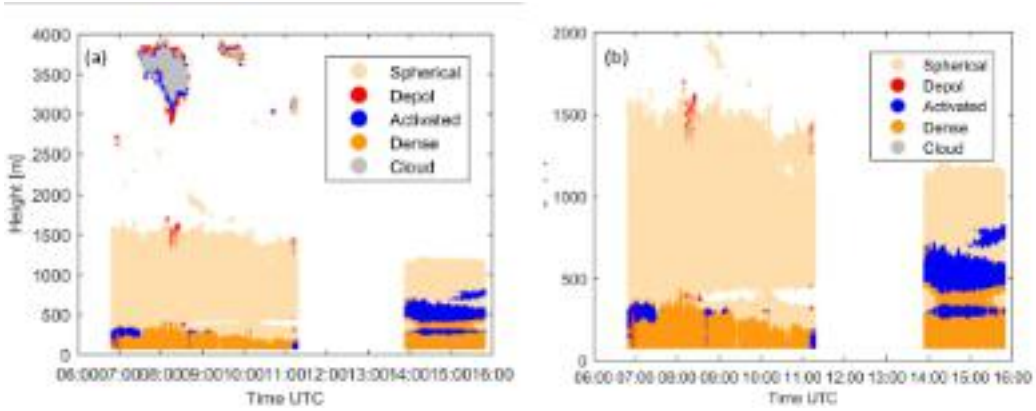

FIGURE 4.4: Four different aerosol classes (spherical particles in light yellow, depolarization particles in red, activated particles in blue, and dense particles in deep yellow) and cloud (gray) based on Lidar classification method on 10th of June 2020. Figure (b) is a zoomed-in view of figure (a) (height range 0 - 2000m).

Figure 4.5 shows the results retrieved from the FTS. From Fig. 4.5a, the dominant aerosol is sulfate above Ny-Ålesund, about AOD = 0.007 $\pm$ 0.0027 in daily average. Dust also exists but lower than sulfate for most of the time, about AOD = 0.0039 $\pm$ 0.0029 for daily average. The AOD of BC and sea salt are much lower than the reliable range of AOD, therefore, the retrieved values of BC and sea salt are not presented. From 9:00 to 11:00, the AOD of sulfate decreases with time. After that, it increases slowly from 12:00 to 14:00, about 0.0135 at 14:00. From Fig. 4.5b, both sulfate and dust are small in size, 0.25 $\pm$ 0.03 µm and 0.30 $\pm$ 0.06 µm, respectively. The retrieved values of each aerosol composition and uncertainty on 10th of June 2020 are given in Tab.4.2.

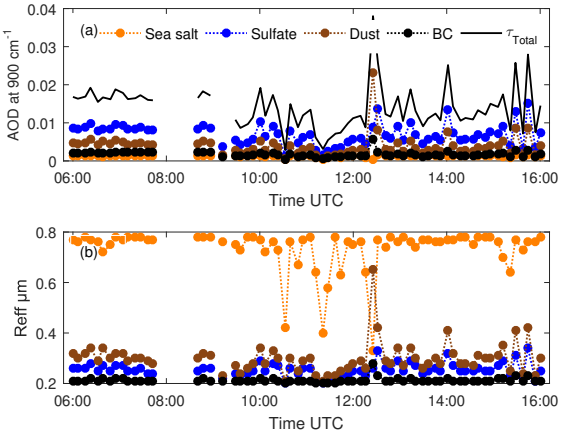

FIGURE 4.5: AOD of sulfate (blue), dust (brown), sea salt (yellow), and BC (black) retrieved from emission FTS measurements (a) and R_{eff} results with same color information (b) on 10th of June 2020.

TABLE 4.2: The retrieved values of each aerosol composition and uncertainty on 10th of June 2020.

Aerosol composition	sea salt	Sulfate	BC	Dust
AOD	0.0012	0.0070	0.0039	0.0017
Uncertainty of AOD	0.0002	0.0027	0.0028	0.0007
Effective Radius (Reff,um)	0.7354	0.2547	0.2992	0.2129
Uncertainty of Reff	0.0866	0.0268	0.0616	0.0103

Figure 4.6 shows the AOD from the FTS, AERONET and MERRA-2. In this analysis, the AOD from FTS will be called AOD_{IR}, the AOD from AERONET AOD_{AERO} and the AOD from MERRA-2 will be written as $AOD_{MERRA\text{-}2}$. From the measurement of the Sun-photometer (AERONET), as shown in Fig. 4.6a, the AOD_{AERO} (blue line for 500 nm and red line for 780 nm) decreases from 8:00 to 11:00 and increases after 14:24. Compared with AERONET, AOD_{IR} (black line) shows similar daily variation, while the minimum in $AOD_{MERRA\text{-}2}$ (orange line) is at 08:00, about 3 hours earlier than AOD_{IR} and AOD_{AERO}. According to MERRA-2 reanalysis data, as shown

in Fig. 4.6b, the first two major aerosol components are sulfate and dust, which is consistent with AOD_{IR} in Fig. 4.6. Furthermore, the daily variation of $AOD_{MERRA\text{-}2}$ on the 10^{th} of June 2020 is mainly caused by sulfate and sea salt. Apart from sea salt, which shows limited signal in the infrared waveband, the daily variation of sulfate in MERRA-2 is also similar to the FTS measurement, but the turning point in MERRA-2 is about 3 hours earlier than the one in the observations. In conclusion, the agreement of daily variation between FTS measurements and sun-photometer shows the good quality in the retrieval results of FTS.

Additionally, in the afternoon, from Lidar measurement (compare Fig. 4.4), there are indications of activated aerosol at the height of about 500 m. In the FTS retrieval algorithm, the databases of aerosol do not include liquid water or activated particles, which means only dry particles are considered in our retrieval. The appearance of an activated aerosol signal indicates that hygroscopic growth of aerosol needs to be considered in the aerosol scattering properties look-up tables, which will be the focus of future research.

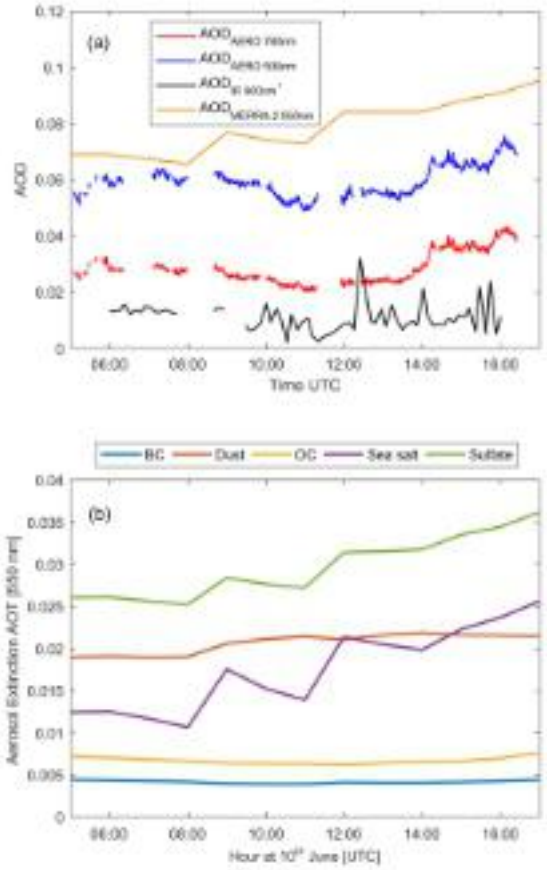

FIGURE 4.6: AOD measured by Sun-photometer (AERONET, 500 nm in blue and 780 nm in red), AOD measured by FTS (900 cm^{-1} in black) and AOD from MERRA-2 reanalysis data (550 nm) in Ny-Ålesund on 10^{th} of June 2020 (a); AOD of different aerosol components in MERRA-2 reanalysis datain Ny-Ålesund on 10^{th} of June 2020 (b). AERONET data from: https://www.mdpi.com/2072-4292/11/11/1362; MERRA-2 data from: https://goldsmr4.gesdisc.eosdis.nasa.gov/data/MERRA2/M2T1NXAER.5.12.4/.

4.1.5 Aerosol Composition Dataset from FTS

Following the method described in Sec.3.3, sulfate (dry or wet state), sea salt (dry or wet state), dust and BC is retrieved under different RH conditions. The retrieved aerosol composition data are from 2019 to 2022. An example of the retrieved values of each aerosol composition and uncertainty on 10^{th} of June 2020 is given in Tab.4.2. The results of longtime measurements are presented in Fig. 4.7. The dominant aerosol type varies from April to August and is not fixed. For sulfate, it is often present in the Arctic, higher during Spring time and lower in Summer. Similarly, BC is also frequently observed in the Arctic, with less obvious seasonal variations than that of sulfate. A BC outburst event is observed in each Spring and Summer. In Spring, sulfate and BC are significant while sea salt and dust are lower. In addition,

a sea salt enhancement event is observed in Summer, which might be emitted from open water nearby.

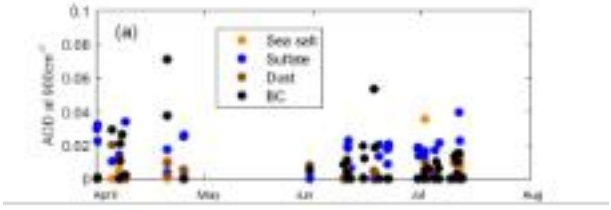

FIGURE 4.7: Long time period observation using FTS from April to August in 2020.

4.1.6 Summary about TCWRET-V2

Normally, the optical properties of aerosols is provided in the visible wavelength band, such as 550 nm. FTS gives us a different kind of information about the aerosol, i.e. the composition of the aerosol. This part of study shows that it is possible to use infrared emission FTS for aerosol composition retrieval. Besides, it is also important to note that it is difficult to obtain complete aerosol information using a single instrument. Therefore, I developed a joint radar observing schema that exploits the advantages of both instruments. Currently, TCWRET-V2 can provide total column information of aerosols, while aerosol profile retrieval is not possible now.

4.2 ARE in the longwave range during Winter

As mentioned in Sec.3.5, during the aerosol wet growth process, the ARE may be growing more than we previously knew. In this study, the FTS can be used to observe aerosol composition and the algorithm also includes the process of aerosol wet growth. During the observations, we found that the infrared radiation from the aerosol wet growth process is higher than the values observed in previous studies (compare Sec.3.5). In order to obtain more specific values and possible influencing factors of ARE, we then combined various observations and models to investigate the ARE during the aerosol wet growth process. This part of work is being submitted for publication.

4.2.1 Seasonal Variation of Aerosol Composition from MERRA-2

Understanding aerosol composition is crucial for studying aerosol Atmospheric Radiative Effects (ARE). Using MERRA-2 reanalysis data to analyze the seasonal variations of individual aerosol compositions in the Ny-Ålesund enhances our comprehension of the infrared radiative effects of aerosols prior to actual observations.

Figure 4.8 illustrates the monthly variation in Aerosol Optical Depth (AOD) at 550 nm for different aerosol components (sulfate, sea salt, organic carbon (OC), dust, and black carbon (BC)) over a year, based on MERRA-2 reanalysis data over a 20-year period. There is a notable spring peak in sulfate and dust aerosols, a summer

peak in organic carbon, and a significant winter peak in sea salt aerosols. These seasonal variations highlight the distinct sources and atmospheric processes driving aerosol concentrations. The spring peak in sulfate and dust underscores the importance of long-range dust transport, while the summer peak in organic carbon suggests increased biomass burning or biogenic emissions. Notably, sea salt aerosols exhibit significant variations throughout the year, with minor peaks in late autumn and a pronounced increase during the winter months (December to January). This wintertime elevation in sea salt AOD is likely due to enhanced wind speeds, which facilitate the production of sea salt aerosols from blowing snow to the atmosphere.

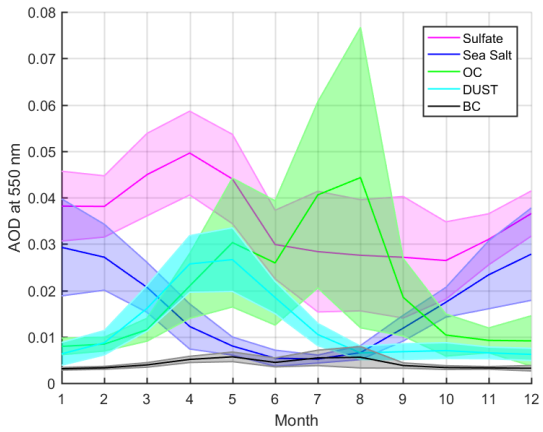

FIGURE 4.8: Seasonal variation of sulfate, sea salt, OC, dust and BC from MERRA-2 reanalysis data averaged from 2002 to 2021 with one standard deviation (shaded area) in Ny-Ålesund.

4.2.2 Warming Effect of Aerosols during Wet Growth

When examining the relationship between ARE_{AW} and RH in the model simulation (Sec.3.5.2), as shown in Fig.4.9a, a sharp increase in ARE_{AW} is predicted as RH rises. This abrupt enhancement in ARE_{AW} corresponds to the aerosol's deliquescence point. Specifically, the transition point of ARE_{AW} is mainly determined by aerosol composition. For example, the ARE_{AW} associated with sea salt aerosols, characterized by a number density of 500 cm^{-3} (depicted as the solid black line in Fig. 4.9a), suddenly increases to 10 Wm^{-2} at an RH level of 75%, which is about 5 times higher than that in dry conditions (about 2 Wm^{-2}). The magnitude of this number concentration (500 cm^{-3}) is within the measurable range at NY-Ålesund (Jung et al., 2018; Pasquier et al., 2022). In contrast, sulfate aerosols exhibit the transition point of ARE_{AW} at 85% as the deliquescence RH of sulfate values at 85% (Peng, Chen, and Tang, 2022) (indicated by the dashed black line in Fig. 4.9a).

Figure 4.9b depicts the ARE_{AW} measurements under varying ambient RH (Cloudnet is used to determine the altitude at which the aerosol was located, and then the RH value for that altitude is obtained from the ERA5). conditions for different dominant aerosol composition in Ny-Ålesund based on FTS measurements. When the dominant aerosol is sea salt and sulfate, the ARE_{AW} from the FTS observation also increases as RH rises. The corresponding RH of sudden enhancement of ARE_{AW} in sea salt dominated cases is about 80% - 85%, while that in sulfate dominated cases is around 90%. Among all the observations, three cases with ARE_{AW} exceeded 30

Wm^{-2}, and these cases were characterized by sea salt aerosols. Conversely, for non-hygroscopic aerosols, such as dust and black carbon, the ARE_{AW} is about 1.45 ± 2.00 Wm^{-2} and doesn't change with RH.

BSRN measurements give the ARE in the mid-infrared range, as shown in Fig.4.9c. The analysis in Fig.4.9c considers the ARE in three distinct scenarios: ARE_{dry}, $ARE_{surface}$, and $ARE_{intrusion}$, each representing single-layer high RH scenarios based on water vapor profiles from radiosonde (methods see sec.3.5.2). Overall, we observe the trending that ARE increases with rising RH. Specifically, under dry conditions (RH < 60%), the ARE remains a low value of about 1.1 ± 4.4 Wm^{-2} and does not vary with RH, which is consistent with previous findings (see Fig.4.9a and b). As RH increases to between 60% and 80%, the ARE shows a significant increase. Specifically, in the cases of $ARE_{surface}$, the mean ARE averaged between 60% to 80% RH is approximately 19.3 ± 12.0 Wm^{-2}. As RH exceeds 80%, the ARE escalates rapidly from about 40 Wm^{-2} at 80% RH to approximately 100 Wm^{-2} at 90% RH. Besides, in all five $ARE_{intrusion}$ scenario cases, there are three cases of high water vapor intrusion, but the values of ARE does not increase with RH, and only other two cases show an enhancement of ARE at 70% RH. It's important to note that even under very high ambient humidity conditions (RH > 90%), we still observe low ARE values, which is due to the presence of non-hygroscopic aerosols (dust or BC) from FTS measurements. Furthermore, within high RH conditions (RH > 90%), there are no intermediate ARE values, with transitions primarily occurring within the RH range of 70% to 80%. This indicates that prevalent hygroscopic aerosols in Ny-Ålesund undergo a transformation from a dry to a wet state within this RH range.

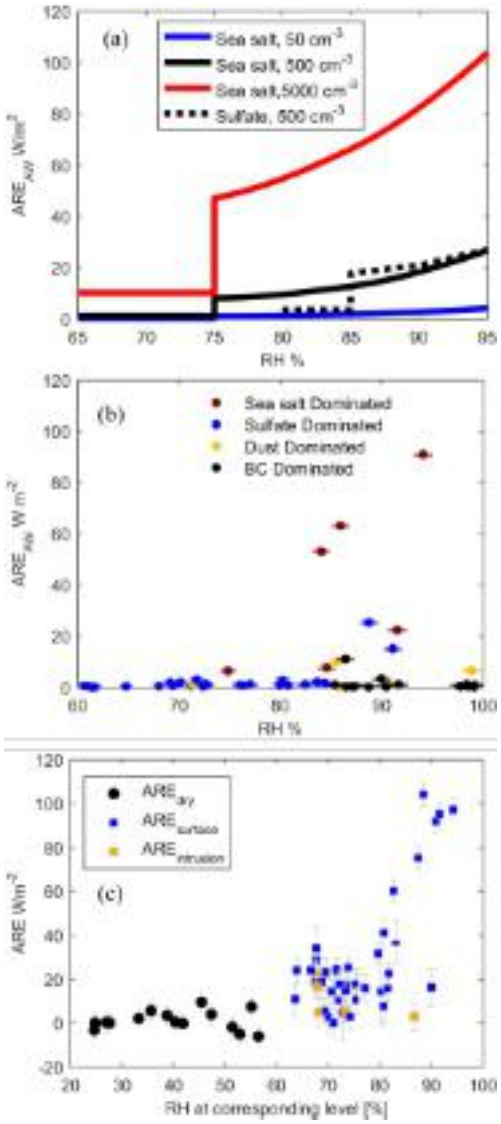

FIGURE 4.9: (a) Aerosol Radiation Effect (ARE_{AW}) of sea salt (red, black and blue lines) and sulfate (black dotted line) as a function of RH, simulated by LBLDIS with different number density cases; (b) The ARE_{AW} of sea salt(brown), sulfate (blue), dust(yellow) and BC (black) dominant cases measured by emission FTS (NYAEM-FTS). The aerosol composition retrieval method is given in Sec.3.3.3 and the methods is given by Ji et al. (2023); (c) ARE under different RH profile scenarios: ARE_{Dry} (black) means that the entire atmosphere is in a dry state (RH < 60%); $ARE_{surface}$ (blue) means that there is a layer of high humidity (RH > 60%) near the ground (< 1 km); $ARE_{intrusion}$ (yellow) represents the situation with a layer of high humidity intrusion (RH > 60%) at high altitude (> 1 km). The error bars represent one standard deviation of the ARE calculated over a 3-hour period (10:30 - 13:30). Note: ARE_{AW} in this figure (a) refers to simulations and (b) refers to measurements by NYAEM-FTS in the AW region, and ARE in figure c refers to the results of measurements (BSRN) in the mid-infrared range.

4.2.3 RH, Temperature, and Sea Salt AOD Changes in the Arctic

To depict the humidity conditions in the Arctic, Figure 4.10a presents the difference of RH between 2000 - 2022 and 1980 - 2000 in the Arctic at 900 hPa in winter (DJF). In the region around Ny-Ålesund, RH has significantly increased, showing a rise of approximately 2 - 6% compared to pre-2000 levels. Typically, as Arctic warming, rising temperatures often lead to a decrease in RH. However, the notable increase in RH at Ny-Ålesund suggests that specific humidity is increasing more rapidly in this region compared to other parts of the Arctic. This anomaly points to unique local atmospheric conditions or processes that are enhancing moisture content more effectively than elsewhere in the Arctic.

MERRA2 reanalysis data, illustrated in Figure 4.10b, indicate a general decrease in sea salt AOD across the Arctic compared to the pre-2000 period. However, there is a notable increase in sea salt AOD in Ny-Ålesund and nearby area. The difference in sea salt AOD between 2000-2022 and 1980-2000 reveals a statistically significant positive anomaly near Ny-Ålesund, approximately +0.005.

When combining the changes in RH and sea salt AOD anomaly, we observe that regions with high humidity and positive sea salt AOD anomalies coincide with areas experiencing large positive temperature anomalies, as shown in Figure 4.10c. Specifically, these regions exhibit temperature anomalies around +3 ^{o}C. These findings highlight the significant role of aerosol wet growth in the Arctic. The suitable RH conditions in Ny-Ålesund have likely facilitated the wet growth of sea salt aerosols, contributing to the observed positive temperature anomalies.

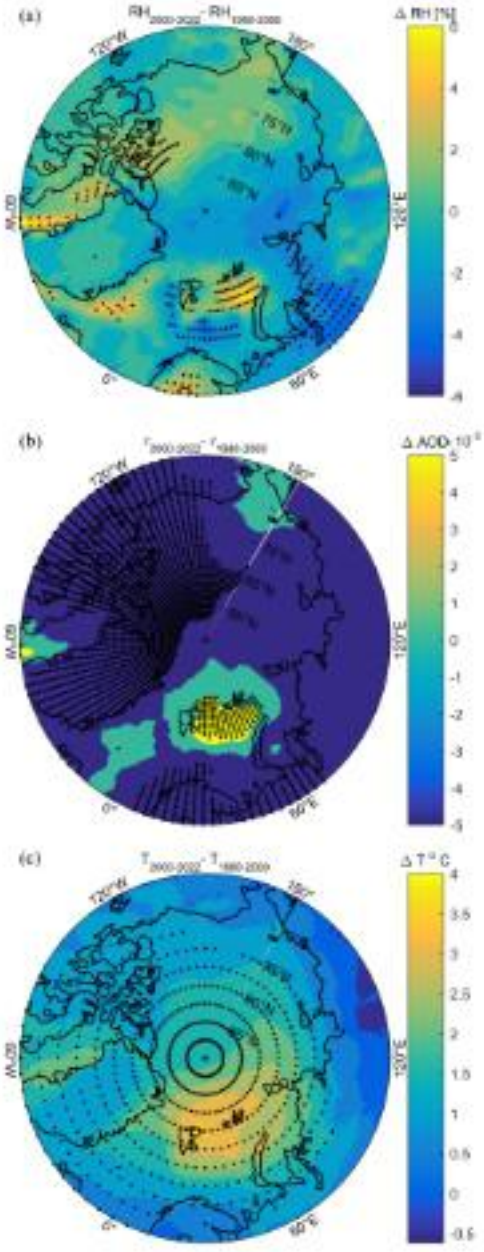

FIGURE 4.10: (a) The difference of RH between 2000 - 2022 and 1980 - 2000 in the Arctic at 900 hPa in winter (DJF), data from ERA5 (Hersbach et al., 2023); (b) The difference of Sea salt aerosol optical depth between 2000 - 2022 and 1980 - 2000, data from Merra-2 reanalysis data (Gelaro et al., 2017); (c) The difference of temperature between 2000 - 2022 and 1980 - 2000 in the Arctic at 900 hPa in winter (DJF), data from ERA5 (Hersbach et al., 2023). The black dots in (a), (b), and (c) mean the difference of this grid passes the significance test (95%).

4.2.4 Summary about ARE

In this study, based on the data measured from BSRN, Cloudnet, radiosonde data and FTS, the infrared radiative effect of aerosols during wet growth process has

been investigated. Under dry conditions (RH < 60%), the ARE in the whole mid-infrared range remains consistently below 10 Wm^{-2}, consistent with previous studies (Markowicz et al., 2003; Vogelmann et al., 2003; Lohmann et al., 2010). However, as RH increases, a significant increase in ARE is observed. Between RH levels of 60% and 80%, the average ARE is about 19.3 $\pm$ 12.0 Wm^{-2}, with peaks of about 36 Wm^{-2} at RH levels of 70% and 80%, respectively.

Moreover, in cases where the aerosol layer becomes more humid (RH > 80%), the ARE can further increase from about 36 to about 92.7 $\pm$10.7 Wm^{-2}. Under such conditions, the growth of wet aerosols is rapid, and the additional infrared radiation caused by wet aerosols is very close to that from clouds. In fact, the cloud radar used in Cloudnet may not effectively detect very small cloud droplets, potentially leading to misjudgement of these cloud droplets as aerosols, especially at high RH conditions (> 90%) here. This possible misjudgement, which represents a transition state between wet aerosols and cloud droplets, underscores the reliability of ARE values ranging from 0 to 36 Wm^{-2} for RH levels between 60% and 80% compared to those observed at higher RH conditions (> 90%). Therefore, the maximum ARE value can be estimated to be around 40 Wm^{-2}; values surpassing this threshold may be attributed to cloud droplets. On the other hand, based on the results of this study, when an instrument can not accurately differentiate between particle sizes of aerosols and cloud droplets, utilizing the ARE or LWD to distinguish between aerosols and clouds could be a potential method to achieve this distinction.

This part of study focuses on the infrared radiative effects of wet aerosols in winter, but it should be noted that such phenomena can also occur in other seasons. In these seasons, however, the presence of solar radiation from the Sun introduces additional complexities. In addition to emitting additional infrared radiation, wet aerosols also contribute to the scattering of solar shortwave radiation. Consequently, addressing the energy budget implications of aerosols during the wet growth process in other seasons requires further research and in-depth exploration.

4.3 A New Poleward Rapid Pathway for African Dust Transport to the Arctic

4.3.1 The Detailed Description of Rapid Pathway

The rapid pathway, first proposed by Francis et al. (2018), for African dust transport, generally defined as direct movement across the North Atlantic from Africa to the Arctic, is not well characterized, requiring further investigation of the contribution of African dust to the Arctic dust load via this pathway. To address this, we use GEOS-Chem model simulations. A specific dust enhancement in March 2022, is given in Fig.4.11a. A dust plume originating in North Africa crosses the Iberian Peninsula on March 14, 2022, enters the Arctic Circle on March 19, 2022, and finally reaches Ny-Ålesund (79 $^\circ$ N, 12 $^\circ$ E) on March 20, 2022, before retreating a day later. This dust intrusion is consistent with the one-week duration characteristic of the RP.

In this model simulation, dust emissions are fixed in the African region, meaning that dust in any part of the world originates from Africa. Consequently, there is a lagged linear correlation between dust AOD in any location and the source emission region; when the source emission dust AOD is high, other locations will also have

high AOD after several days. Based on this, we averaged the meridional dust AOD data in the Arctic between latitudes 66 to 80 ° N (white dashed box area in Fig.4.11a) to obtain time series data of dust AOD for each longitude. By performing a lagged correlation between this data and the dust AOD time series from the source region (red box area in Fig.4.11a), we determine that the lag days corresponding to the maximum correlation coefficient represent the time required for dust to be transported from the source region to the Arctic.

Based on the above method, lagged days are available for the dust AOD and source emission regions at each longitude in the Arctic, which can be categorized into four distinct regions: the RP region (30 ° W - 0 - 50 ° E) with a one-week delay; the Western North Atlantic region (60 ° W - 30 ° W) with a 13-day delay; the Europe and Siberia region (50 ° E - 120 ° E) with a 12-day delay; and Asia, Bering Strait, and North America region (120 ° E - 180 - 60 ° W) with a delay of three weeks, as shown in Fig.4.11b. This figure shows the average number of lag days within the four regions. The smaller the absolute value of the number of lagged days, the faster the dust is transported from Africa to the Arctic. When the RP is open, the African dust enters the Arctic via the RP region faster than others, indicating the importance of the RP for the Arctic dust load.

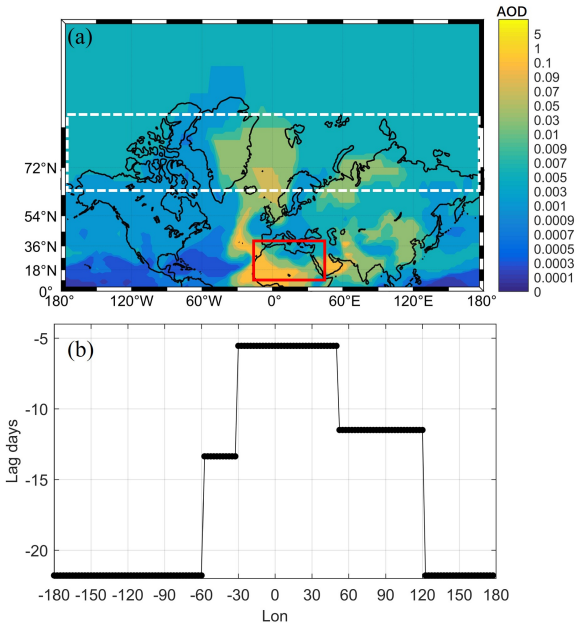

FIGURE 4.11: (a) GEOS-Chem model simulated dust AOD only with African dust emission on March 21, 2022. The white dashed box area is the latitude band between 66 - 80° N; the red box area represents the dust emission area (15 - 40 ° N, 15° W - 45 ° E). (b) Using the GEOS-Chem model simulated dust AOD only with African dust emission, on a daily mean basis, the Arctic region is segmented based on the lagged correlation coefficients of dust AOD between the Arctic area (66 - 80 ° N, white dashed box area in figure a) and that of the dust emission area (red box region). The days with the highest correlation coefficients vary across different longitudes, leading to the classification of the Arctic into four regions according to longitude: Rapid pathway (RP) region (30° W - 50 ° E); Europe and Siberian region (50° E - 120 ° E); the Asian, Bering Strait and North American region (120° E - 0 - 60 ° W); and the western North Atlantic region (60° W - 30 ° W).

4.3.2 Enhanced Dust Transport via the Rapid Pathway Region

Based on the specific definitions given by the GEOS-Chem model, we select two regions of African dust transport: one is the RP region (the blue area in Fig.4.12a), and the other is the European land transport region (the brown area in Fig.4.12a). The shaded region in the figure is the response region in the Arctic affected by the RP as we defined in Sec.4.3.1.

As we mentioned before, directly using reanalysis data does not eliminate the impact of source emissions; therefore, we scaled the dust AOD to obtain the scaled dust AOD, as shown in Fig.4.12b and c. From Fig.4.12b and c, the scaled dust AOD in the source emission area is a unit for each month (Here is an example in March.) of the year. As the dust is transported away from Africa, the scaled dust AOD gradually decreases poleward. Compared to the pre-2000 period, there is little change in the northward dust transport through continent after 2000. However, dust transport strengthens in the central North Atlantic, the RP region, after 2000. This is particularly evident in the difference between pre- and post-2000, as shown in Fig.4.12d: the Atlantic pathway in RP region shows a peak in dust AOD in the central North Atlantic (45 - 60 $^{\circ}$ N) that continues to transport dust northwards, bringing more dust to the Arctic. This analysis for April is similar to that in March, while other months show little variation over time, as shown in Fig.4.13.

Overall, by scaling dust AOD, the transport of Saharan dust to the Arctic is tracked, specifically highlighting the increasing along the RP region (the central North Atlantic) in recent decades after the year 2000.

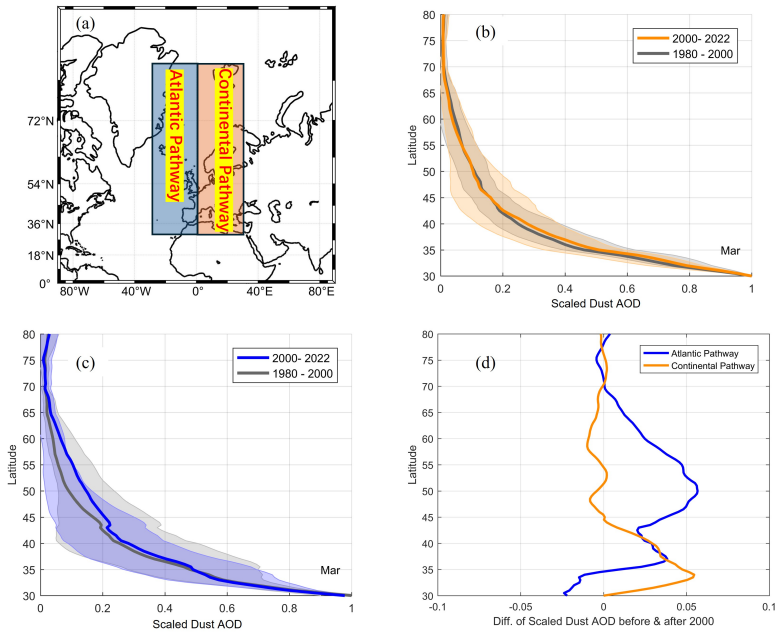

FIGURE 4.12: (a) Two regions of African dust transport: one is the RP region (the blue area in Fig.4.12a, noted as Atlantic pathway), and the other is the continental pathway (the orange area in Fig.4.12a). (b) The scaled dust AOD averaged in orange area before (the gray line with one standard deviation as shaded) and after 2000 (the orange line with one standard deviation as shaded) in March. (c) Similar to (b), but averaged over the RP region. (d) The difference in scaled dust AOD between the time period before and after 2000 in March ($AOD_{2000\_2022} - AOD_{1980\_2000}$), the blue line is the Atlantic pathway, and the orange line is the continental pathway.

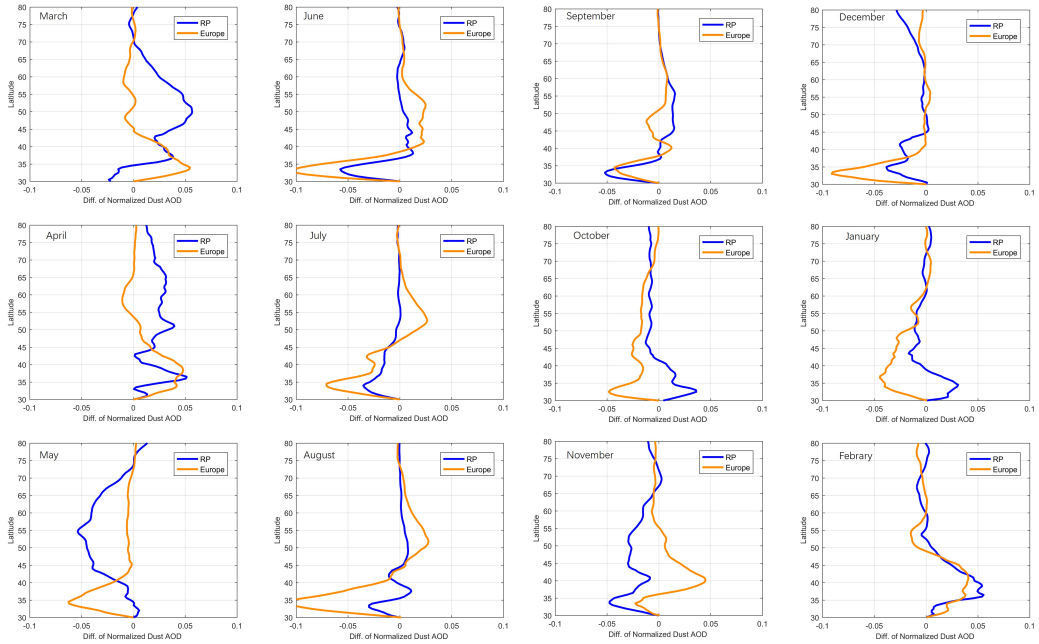

FIGURE 4.13: The difference in scaled dust AOD between the time period before and after 2000 in all months ($AOD_{2000\_2022} - AOD_{1980\_2000}$), the blue line is the Atlantic pathway, and the orange line is the continental pathway.

4.3.3 Poleward Wind: Shifting Saharan Dust Pathways from Land to Ocean for Arctic Transport

The rapid pathway acts as a important corridor for the transport of materials and energy to the Arctic, which may contribute to Arctic warming. To investigate this potential linkage, the poleward wind and surface temperature anomalies are analyzed in the specific region within the Arctic that exhibit a response to the rapid pathway.

Figure 4.14a and b depict the difference of the poleward wind (700 hPa) between pre-2000 and after-2000 in March and April, respectively. In March, significant positive poleward wind anomalies extended across the North Atlantic, stretching from northwestern Africa to southwestern Greenland, while significant negative anomalies were observed from east of Greenland to Svalbard. This pattern of poleward wind anomalies suggests the presence of an anticyclonic anomalous near Iceland, indicating a weaker Iceland Low from 2000-2022 compared to 1980-2000. Therefore, this weakening Iceland Low leads to a more meandering atmospheric circulation between mid-latitude and the Arctic, favoring the RP transport of dust into the Arctic. Similarly, in April, the anomalous wind patterns shift slightly clockwise, pushing the positive polar wind anomalies further north. Both March and April show evidence of an anticyclonic anomalous around Iceland, indicating weakening Iceland Low after 2000. Overall, the poleward transport of African dust via the RP region's is significant in March and April. In contrast, over the European continent, the poleward winds consistently show a negative anomaly, resulting in a preference for dust transport across the North Atlantic to the Arctic rather than through Europe.

Figures 4.14 c and d illustrate the differences in surface temperature (at 1000 hPa) between the pre-2000 and post-2000 periods for March and April, respectively. In March, significant warming is observed in the southwest region of Greenland, while in April, the warming shifts to the area east of Svalbard. Both regions of pronounced warming correspond to areas identified as responsive to the rapid pathway in the Arctic. Furthermore, the warming patterns align with the poleward wind directions during March and April (compare Fig.4.14a and b, with winds favoring Greenland in March and shifting toward Svalbard in April. These observations suggest a strong potential link between the rapid pathway and the observed Arctic warming.

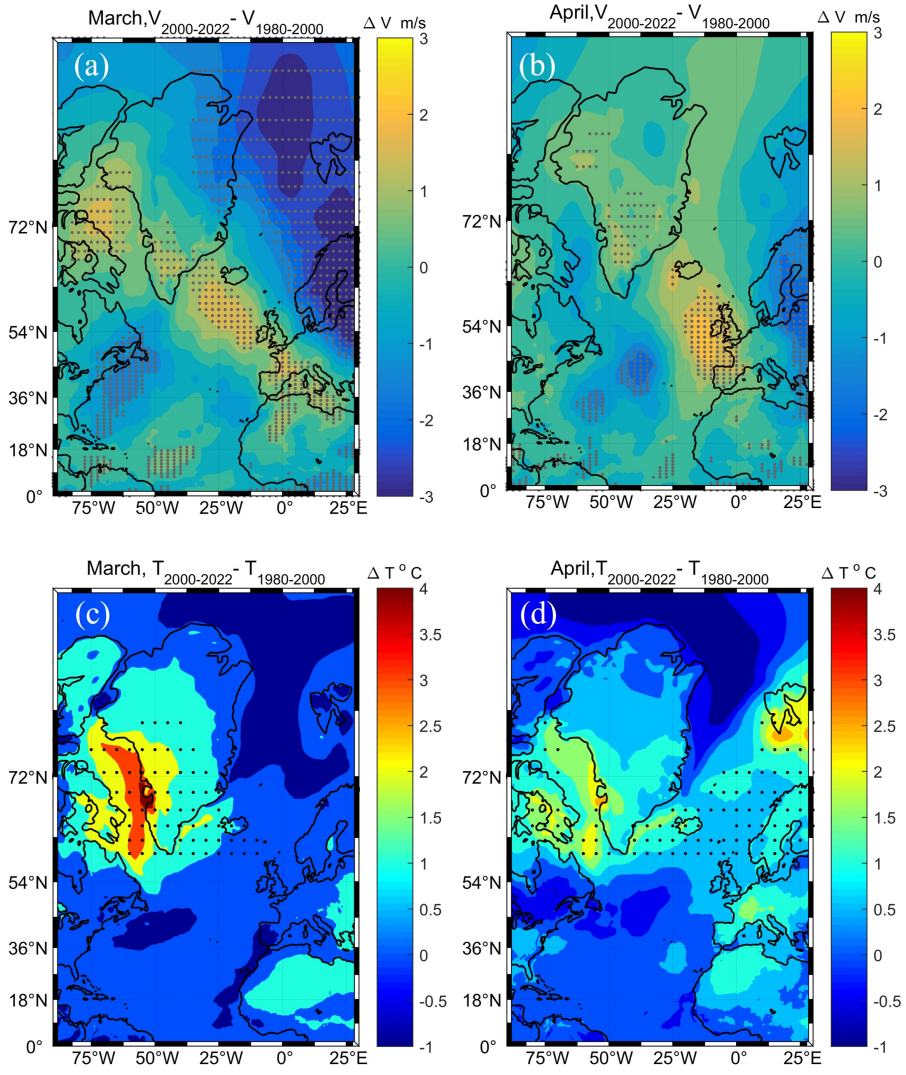

FIGURE 4.14: (a) The difference of the poleward wind (700 hPa) averaged for all years between pre-2000 and after-2000 in March ($V_{2000\_2022} - V_{1980\_2000}$). The black dots mean the difference between the two time period passed the 95% significance test; (b) is similar to that in (a), but in April. (c) The difference of the surface temperature (1000 hPa) averaged for all years between pre-2000 and after-2000 in March ($T_{2000\_2022} - T_{1980\_2000}$). The black dots mean the difference between the two time period passed the 95% significance test; (d) is same as (c) but in April.

4.3.4 Summary of Rapid pathway

This part of work gives a specific description of the Rapid Pathway (RP). Based on that, we investigate the temporal variation of the influx of African dust into the Arctic via RP. Using GEOS-Chem model simulations, we demonstrate its enhanced effectiveness in accelerating the transport of African dust within approximately one week, in contrast to other regions. Our analysis reveals a significant shift in African dust transport pathways to the Arctic after the year 2000. Specifically, there is a notable increase in dust transport via the central North Atlantic, RP region, while the European land transport route shows minimal change. The RP region exhibits a peak in dust AOD between 45° N and 60 ° N, indicating a strengthened transport of African dust towards the Arctic. This enhancement is particularly evident in March and April, with the scaled dust AOD decreasing progressively as it moves poleward. The ERA5 wind field data show significant positive anomalies in poleward winds over the North Atlantic in March and April after 2000. These anomalies facilitate the northward transport of dust through the RP region. In contrast, negative wind anomalies over Europe suggest a reduced role of the European pathway in dust transport to the Arctic.

As the Arctic experiences rapid warming, the meridional temperature gradient decreases, which leads to a weakening of the upper tropospheric jet stream pattern (Alizadeh and Lin, 2021). This rapid Arctic warming has caused the Northern Hemisphere circulation to exhibit more meridional characteristics (Francis and Skific, 2015). These changes in atmospheric circulation are likely responsible for altering the transport pathway of African dust to the Arctic, as shown in this study. Besides, recent observations indicate significant changes in the aerosol composition in the Arctic. Sulfate aerosols, historically prevalent due to industrial emissions from Europe and North America, have shown a marked decrease, which is attributed to enhanced pollution control measures and stricter emission regulations implemented in these regions over the past few decades (Manktelow et al., 2007; Yang et al., 2019; Westervelt et al., 2021). Concurrently, there has been a significant increase in sea salt aerosols, driven by changing atmospheric circulation patterns and reduced sea ice extent (Frey et al., 2019; Confer et al., 2023; Browse et al., 2014). From our results, the transportation of air mass from mid latitude to the Arctic is changing from the European continent to the North Atlantic over time, particularly via the rapid pathway. This shift is bringing more dust to the Arctic, and potentially leading to more sea salt aerosols to the Arctic.

Overall, these findings underscore the increasing influence of global warming and Arctic amplification on atmospheric circulation patterns, leading to more frequent poleward transport of material and energy, and thereby maintaining the RP of African dust open in the foreseeable future. Therefore, it is crucial for predicting and mitigating the impacts of dust aerosol on the Arctic climate and ecosystems. In addition, as shown in the model simulation, Ny-Ålesund, located in this RP, is a suitable site to observe aerosol transportation. Therefore, continued measurements of aerosols in the Ny-Ålesund are helpful to further investigate the RP and its impact on the climate system, specifically Arctic amplification.

4.4 Conclusions for the Effect of Aerosol Wet Growth and Rapid Pathway

Based on the FTS measurements and LBLDIS model simulations, there are three parameters that influence the infrared radiation of wet aerosols: ambient RH of the aerosol layer, aerosol composition and aerosol number density. RH and aerosol composition are the most important factors influencing ARE_{AW}. The measurement of aerosol composition, especially by remote sensing method, is still challenging. In this study, we applied a FTS retrieval algorithm to retrieve an aerosol composition measurement for all RH conditions, which is a complement to the previous method in Ji et al. (2023). In addition, if FTS instrument is not available, another method for observing aerosol infrared radiation effects that combines multiple observations is also investigated in this study. The method is based on BSRN observations and uses cloud radar, sounding data, and combined models to obtain ARE step by step. Considering that the sudden increase in ARE with RH is closely related to the deliquescence point of the aerosol, it is possible that the corresponding RH of the sudden increase in ARE (BSRN) can provide some information about the main composition of the aerosol. For example, the deliquescence point of mixed and land source aerosols was found to vary significantly, from around 60% to 85%, while that of marine aerosols was rather consistent at around 80% (Liu et al., 2022). Compared with the sudden increase of ARE in Fig.4.9c, the corresponding RH is about 80%, which suggests that aerosol composition of hygroscopic aerosol in Ny-Ålesund is likely to be marine aerosols, e.g. sea salt. From FTS measurements, the contribution of sea salt is more prominent compared to other aerosol compositions. Therefore, in the Arctic, the contribution of sea salt, or marine aerosols, to infrared radiation in winter is important.

Our measurements, yielding high ARE of hygroscopic aerosols and very low ARE of non-hygroscopic aerosols, indicates sea salt aerosols are very import for the Arctic warming in winter. MERRA-2 reanalysis data, as shown in Fig. 4.8, confirms our results that in Ny-Ålesund, sea salt and sulfate aerosols are significantly dominant than other aerosol components in winter. As spring arrives, sea salt AOD begins to decline while dust AOD gradually increases. This trend continues into summer, when sea salt levels reach their lowest point. Given that sea salt is a major component of winter aerosols, its contribution to Arctic winter warming requires further investigation in the future.

Several studies have shown that Arctic water vapor content is increasing, primarily due to enhanced poleward transport from mid-latitudes via atmospheric river pathways (Sato et al., 2022; Thandlam, Rutgersson, and Sahlee, 2022; Bresson et al., 2022). ERA5 reanalysis data, as presented in the Sec.4.2.3, shows the 23-year mean relative humidity (RH) in the Arctic at 900 hPa during winter (DJF) (Fig. 4.10a). This data indicates that Ny-Ålesund has high water vapor levels during winter, providing suitable ambient RH conditions for aerosol wet growth. MERRA-2 reanalysis data further reveals a positive anomaly in sea salt aerosol optical depth (AOD) in the area around Ny-Ålesund after 2000 (Fig.4.10b). Combining the changes in RH and the sea salt aerosol AOD anomaly, the region of high humidity with positive sea salt AOD anomalies overlaps the regions with the large positive temperature anomalies (see Fig.4.10c). Based on these findings, it is crucial to consider the warming effect of aerosols under high humidity conditions when studying Arctic amplification. The

greenhouse effect of water vapor intensifies surface warming, leading to higher humidity levels in the Arctic (Beer and Eisenman, 2022), which facilitates aerosol wet growth. Increased aerosols in a wet state further warm the Arctic atmosphere, potentially leading to more water vapor and creating a positive feedback loop in Arctic amplification. Therefore, studying the longwave radiation (LWD) contributions from both water vapor and aerosols together is essential.

Although the area of positive sea salt AOD anomalies is very limited in the Arctic, the differences in the deliquescence and efflorescence points during aerosol wet growth process can have the potential to expand the warming effect of aerosols throughout the whole polar regions. Wet aerosols can maintain their hydrated state until they either develop into cloud droplets in supersaturated conditions or revert to dry particles in drier environments, typically below the efflorescence point (Lillard et al., 2009b). For instance, sodium chloride (NaCl) has a deliquescence point of approximately 75% RH and an efflorescence point of around 46% RH (Peng, Chen, and Tang, 2022). Consequently, NaCl remains in a wet state after activation until ambient RH drops below the efflorescence point (e.g. 45% RH). Therefore, the Ny-Ålesund region can act as a "refueling station" for the wet growth of the hygroscopic aerosols, specifically the sea salt aerosols, resulting in a warming effect. Here, these aerosols are activated, and after leaving the region, they can remain activated and travel throughout the Arctic, carrying high values of ARE as long as the ambient humidity is higher than the efflorescence point.

Additionally, the observed shift of the rapid aerosol transport pathway from land to ocean in March and April suggests that with the progression of global warming and Arctic amplification, the mid-latitude North Atlantic region will increasingly transport both more water vapor and a greater quantity of marine aerosols, including sea salts, to the Arctic. This shift has important implications for the Arctic's climate system. Therefore, future studies using Fourier Transform Spectrometers (FTS) to observe aerosol composition, particularly in terms of sea salts and sulfates, will be essential in better understanding how these aerosols contribute to Arctic amplification.

Chapter 5

Conclusions and Outlooks

5.1 Conclusion

Arctic amplification, the phenomenon where the Arctic is warming faster than the global average, remains incompletely understood. Key processes such as temperature feedback, surface albedo feedback, and cloud and water vapor feedback are important to this understanding. Among these, aerosols play a crucial role in Arctic climate by exerting both direct and indirect influences on these feedback mechanisms. The varied climate effects of different aerosol compositions necessitate precise measurements of aerosol components. Since 2019, a Fourier-Transform Infrared Spectrometer (FTS) for measuring down-welling emission, alongside a Raman-Lidar, has been operational at the AWIPEV research base in Ny-Ålesund, Spitsbergen (79 °N, 12 °E) to achieve this goal.

To retrieve aerosol data from FTS measurements, a retrieval algorithm based on the Line-by-Line Radiative Transfer Model and DIScrete Ordinate Radiative Transfer model (LBLDIS) is developed in this study. This algorithm is designed for different aerosol composition (dust, sea salt, black carbon, and sulfate). The data measured on a case study, 10^{th} of June 2020, shows good agreement with MERRA-2 reanalysis data and comparable daily AOD variations to sun-photometer (AERONET) data. Emission FTS is capable of observing downward infrared radiation from the atmosphere without relying on sunlight, making it suitable for year-round observations, even during the polar night. From the observations, it is evident that hygroscopic aerosols, particularly sulfates and sea salts, are predominant in winter. The presence of sea salts is especially significant, as they may play a crucial role in Arctic amplification.

Besides, aerosols under different relative humidity (RH) conditions emit varying levels of infrared radiation. Hygroscopic aerosols, such as sea salt and sulfate particles, absorb atmospheric water vapor, undergo wet growth, and subsequently emit additional longwave downward radiation (LWD). By incorporating the aerosol wet growth process, the magnitude and key factors influencing LWD enhancement using radiance measurements from the emission FTS, Baseline Surface Radiation Network (BSRN), Cloudnet data, and radiosonde data are investigated. The analysis indicates that wet aerosols enhance LWD by an average of 19.3 ± 12.0 Wm^{-2} between RH levels of 60% and 80% during the winter season (DJF) from 2017 to 2022 in the Arctic. Key factors affecting LWD enhancement include aerosol composition, number density, and ambient RH. A significant increase in LWD is observed when RH reaches

the aerosol deliquescence point (approximately 80%), with sea salt aerosols playing a predominant role based on FTS measurements. These findings highlight the importance of aerosol properties, particularly composition, in influencing the Arctic energy balance and suggest a potential positive feedback mechanism for Arctic amplification.

The wet growth process of aerosols highlights the importance of considering aerosol trajectories. Recently, a new pathway for African dust transport to the Arctic was identified. This study investigates the temporal patterns and factors behind African dust influx into the Arctic via the Rapid Pathway (RP). Geos-Chem model simulations delineate the RP region, showing its efficiency in transporting African dust within about one week. Analysis of MERRA-2 data reveals an increase in African dust transport to the Arctic via the RP post-2000, peaking in March and April. RA5 wind field data reveal significant positive anomalies in poleward winds over the North Atlantic in March and April after 2000, facilitating northward dust transport via the RP region. In contrast, negative wind anomalies over Europe suggest a diminished role for the European pathway in Arctic dust transport. This study introduces a novel aerosol composition retrieval method using emission FTS. Results indicate that aerosol wet growth can increase infrared radiation, potentially contributing to a positive feedback mechanism in Arctic amplification. As Arctic warming continues, the atmosphere's increased meandering may enhance direct poleward aerosol transport, such as African dust, further impacting the region's climate.

5.2 Outlook

Aerosol measurements in the Arctic are crucial for understanding the effects of aerosol in the atmosphere, which significantly impacts climate processes such as radiative forcing and cloud formation. These measurements can be obtained through satellite observations, ground-based instruments, and aircraft-based campaigns. However, each method comes with its own set of challenges, particularly in the Arctic.

Satellite observations, such as those from the Moderate Resolution Imaging Spectroradiometer (MODIS, https://modis.gsfc.nasa.gov/about/) and the Atmospheric Infrared Sounder (AIRS, https://airs.jpl.nasa.gov/), provide global AOD data. MODIS, for instance, offers valuable insights but faces difficulties due to the high surface reflectance from snow and ice, which can interfere with accurate aerosol detection. Ground-based observations are another critical method for measuring AOD in the Arctic. The Aerosol Robotic Network (AERONET, https://aeronet.gsfc.nasa.gov/) deploys sun photometers to collect high-quality AOD data. However, the network's coverage in the Arctic is sparse due to the challenging environmental conditions. Aircraft-based measurements offer a more flexible approach, allowing researchers to gather data during specific research campaigns. While these measurements provide valuable insights, they are episodic and geographically limited, lacking the continuous coverage necessary for comprehensive understanding.

The limited network of measurement stations in the Arctic affects the representativeness of the data. Persistent cloud cover can obscure both satellite and ground-based measurements, complicating the differentiation of aerosols from clouds. Seasonal variations, such as the occurrence of Arctic haze, necessitate continuous, long-term observations to capture accurate temporal changes. Ensuring the accurate calibration of instruments in extreme conditions is also a significant challenge, as is the

validation of satellite data with ground-based measurements.

Despite these challenges, advancements in satellite technology, the expansion of ground-based networks, and comprehensive field campaigns are essential to improving aerosol observations in the Arctic. These efforts will enhance our understanding of aerosol impacts on the region's climate, contributing to more accurate climate models and better predictions of future changes in the Arctic environment.

This study introduces a novel aerosol composition retrieval method using emission FTS. Results indicate that aerosol wet growth can increase infrared radiation, potentially contributing to a positive feedback mechanism in Arctic amplification. As Arctic warming continues, the atmosphere's increased meandering may enhance direct poleward aerosol transport, such as African dust, further impacting the region's climate.

Based on the current algorithm, future work will aim to refine and enhance the aerosol retrieval algorithm for improved accuracy and reliability. For example, by integrating more comprehensive datasets and advanced machine learning techniques, the algorithm might be optimized to provide more precise aerosol characterizations.

To achieve a more detailed understanding of aerosol-cloud interactions and their impact on Arctic amplification, it is crucial to integrate data from multiple instruments. Future research will focus on combining measurements from the Fourier-Transform Infrared Spectrometer (FTS), Raman-Lidar, sun photometers, and other relevant instruments. This multi-instrument approach will enable cross-validation of results and provide a more robust dataset for analysis, improving the accuracy of aerosol and cloud property retrievals. Establishing long-term monitoring programs at key Arctic locations, such as Ny-Ålesund, will be essential for tracking changes in aerosol properties over time. This will involve setting up permanent measurement stations equipped with advanced sensors and ensuring continuous data collection. Long-term datasets will be invaluable for identifying trends, understanding seasonal variations, and assessing the long-term impacts of aerosols on Arctic climate dynamics. Therefore, future studies will delve deeper into the interactions between aerosols and clouds, with a focus on understanding how these interactions influence cloud formation, properties, and lifetime. This will involve detailed analysis of the microphysical processes governing aerosol-cloud interactions, using both observational data and high-resolution numerical simulations. Special attention will be given to mixed-phase and ice clouds, which play a significant role in Arctic climate processes.

Building on the discovery of the Rapid Pathway (RP) for African dust transport to the Arctic, further research will explore additional aerosol transport pathways. This will involve using advanced atmospheric models to simulate and identify potential new pathways and analyzing how changes in atmospheric circulation patterns may influence these pathways. Understanding these transport mechanisms is crucial for predicting future aerosol influxes and their climatic impacts. Investigating how ongoing and projected climate changes will affect aerosol dynamics in the Arctic would be helpful for studying AA. This will include studying the effects of warming temperatures, changing precipitation patterns, and shifting atmospheric circulation on aerosol sources, transport, and deposition. By integrating climate models with aerosol dynamics models, researchers can better predict future scenarios and develop strategies to mitigate adverse impacts.

By addressing these areas, future research will significantly advance our understanding of aerosols in the Arctic environment, their interactions with clouds, and their contributions to Arctic amplification. This knowledge will be critical for developing effective strategies to mitigate the impacts of climate change in this vulnerable

region.

Appendix A

supplementary

A.1 Non-isotropic emissions correction coefficient

The relationship between integral calculation of radiance in the AW region, II_{AW}, with the cosine of the zenith angle, μ , is assumed as exponent. Figure A.1 presents the relationship II_{AW} with μ. The integral of the fitted function with μ could be calculated as the correction coefficient in Equation 3.28 after getting the fitted function (black dotted lines), and the flux in the unit of Wm^{-2} could then be obtained. In this figure, the aerosol type is dry sea salt with a 1 µm (diameter). The method of aerosol hygroscopic growth mentioned in Sec.3.3.3 is used to calculate the wet particles. The varied colors indicate the various number densities of sea salt, while the black line stands for a clear sky scenario. Four cases from the LBLDIS simulation at four RH conditions (65%, 75%, 85%, and 95%) are provided as well. When the aerosol number density is low, between 50 and 500 cm^{-3}, the ratio of $II_{AW}(\mu)$ to $II_{AW}(\mu = 1)$ at various u remains relatively constant. With a sharper relationship in dry conditions and a progressive flattening with an increase in RH, this phenomenon occurs in all RH cases. Furthermore, the differences in the equations at higher relative humidity levels (75%, 85%, and 95%) are not apparent, suggesting that the correction coefficient for non-isotropic aerosol scenarios may be similar under wet conditions. Additionally, such a relationship dramatically flattens as RH rises in the presence of heavy aerosol pollution, such as that present in the case of 5000 cm-3, and tends to be isotropic in high RH as in the case of RH=95%. We anticipate that under high RH condition, a significant number of aerosols will progressively activate and develop into a thick cloud in the atmosphere that emits isotropic radiation.

Following the simulation of the sea salt, the sulfate aerosol is also calculated by LBLDIS. Table .A.1 displays the whole results, including the atmosphere on a clear day. The correction coefficient for a clear atmosphere is approximately 1.08. For a clear sky, the light from atmosphere emission could be very nearly isotropic. While for aerosols, sea salt has a correction coefficient of 1.40 in dry state and roughly 1.35 in wet, which is considerably different from clear day. Although the activated RH for sulfate aerosol and sea salt is different (75% for sea salt and 85% for sulfate), both exhibit similar correction coefficient values when they are activated.

In conclusion, non-isotropic radiance emission from aerosols should be taken into account while doing flux calculation for a moderate aerosol event, which frequently occurs in the Arctic. In dry conditions, aerosols have a different correction

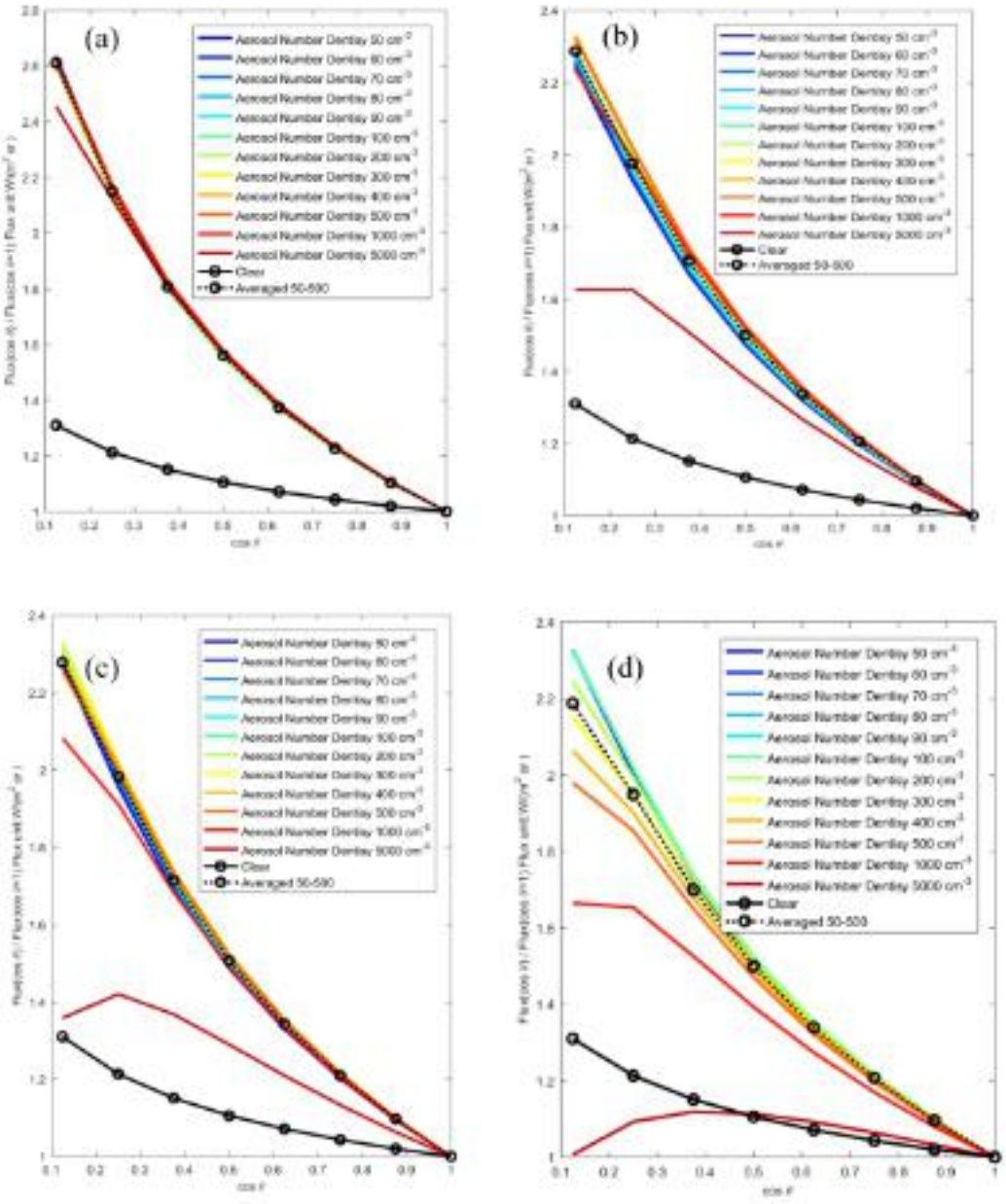

FIGURE A.1: (a)The relationship between II_{AW} with μ. The varied colors indicate the various number densities of sea salt, while the black line stands for a clear sky scenario. The black dotted lines is the averaged from 50 cm^{-3} to 500 cm^{-3}. Four cases from the LBLDIS simulation at four RH conditions (65% in (a), 75% in (b), 85% in (c), and 95% in (d)) are provided as well.

coefficient than they do in wet conditions. It is not very varied for various aerosol types.

TABLE A.1: The correction coefficient for atmosphere, sea salt and sulfate at different RH.

RH	<75%	75%	85%	95%
C_Atmos	1.08	1.08	1.08	1.08
C_sea salt	1.40	1.35	1.35	1.35
C_sulfate	1.36	1.36	1.37	1.33

A.2 Publication

The retrieval algorithm described in first part of Chapter 3, see Sec.3.3, was published. The information about this publication is as follows:

Ji, D., Palm, M., Ritter, C., Richter, P., Sun, X., Buschmann, M., and Notholt, J.: Ground-based remote sensing of aerosol properties using high-resolution infrared emission and lidar observations in the High Arctic, Atmos. Meas. Tech., 16, 1865–1879, https://doi.org/10.5194/amt-16-1865-2023, 2023.

The results (figures and text content) in section 4.1 in Chapter 4 is mainly based on this paper. And the author contributions is described below: PR implemented TCWRET and DJ developed it into the retrieval of aerosol parameters using TCWRET. MP designed and built the measurement setup, performed measurements and gave advice in the development of TCWRET. CR performed Lidar measurements and gave advice in using the Lidar data and the sun-photometer data. XS gave the advice in forward model simulation. MB gave the advice of calibration processes. JN gave advice in the setup of the measurement and the development of TCWRET. All authors contributed to manuscript revisions.

Bibliography

Adebiyi, Adeyemi et al. (2023). "A review of coarse mineral dust in the Earth system". In: *Aeolian Research* 60, p. 100849. ISSN: 1875-9637. DOI: https://doi.org/10.1016/j.aeolia.2022.100849. URL: https://www.sciencedirect.com/science/article/pii/S1875963722000799.

Albrecht, Bruce A. (1989). "Aerosols, Cloud Microphysics, and Fractional Cloudiness". In: *Science* 245.4923, pp. 1227–1230. ISSN: 00368075, 10959203. URL: http://www.jstor.org/stable/1704234 (visited on 02/07/2024).

Alduchov, Oleg A. and Robert E. Eskridge (1996). "Improved Magnus Form Approximation of Saturation Vapor Pressure". In: *Journal of Applied Meteorology and Climatology* 35.4, pp. 601 –609. DOI: 10.1175/1520-0450(1996)035<0601:IMFAOS>2.0.CO;2. URL: https://journals.ametsoc.org/view/journals/apme/35/4/1520-0450_1996_035_0601_imfaos_2_0_co_2.xml.

Alizadeh, O. and Zhaohui Lin (2021). "Rapid Arctic warming and its link to the waviness and strength of the westerly jet stream over West Asia". In: *Global and Planetary Change* 199, p. 103447. DOI: 10.1016/J.GLOPLACHA.2021.103447.

Ansari, Asif S and Spyros N Pandis (1999). "Prediction of multicomponent inorganic atmospheric aerosol behavior". In: *Atmospheric Environment* 33.5, pp. 745–757. DOI: https://doi.org/10.1016/S1352-2310(98)00221-0.

Asmi, E. et al. (2016). "Aerosol size distribution seasonal characteristics measured in Tiksi, Russian Arctic". In: *Atmos. Chem. Phys.* 16.3, pp. 1271–1287. DOI: 10.5194/acp-16-1271-2016.

Barber, D. G. et al. (2008). "The Changing Climate of the Arctic". In: *Arctic* 61, pp. 7–26. ISSN: 00040843. DOI: 10.1038/s43017-021-00240-1. URL: http://www.jstor.org/stable/40513353 (visited on 12/27/2023).

Beer, Emma and Ian Eisenman (2022). "Revisiting the Role of the Water Vapor and Lapse Rate Feedbacks in the Arctic Amplification of Climate Change". In: *Journal of Climate* 35.10, pp. 2975 –2988. DOI: https://doi.org/10.1175/JCLI-D-21-0814.1.

Bellouin, Nicolas and Hongbin Yu (2022). "Chapter 11 - Aerosol–radiation interactions". In: *Aerosols and Climate*. Ed. by Ken S. Carslaw. Elsevier, pp. 445–487. ISBN: 978-0-12-819766-0. DOI: https://doi.org/10.1016/B978-0-12-819766-0.00004-3. URL: https://www.sciencedirect.com/science/article/pii/B9780128197660000043.

Bergeron, Tor (1935). "On the physics of clouds and precipitation". In: *Proc. 5th Assembly UGGI, Lisbon, Portugal, 1935*, pp. 156–180.

Bey, Isabelle et al. (2001). "Global modeling of tropospheric chemistry with assimilated meteorology: Model description and evaluation". In: *Journal of Geophysical Research: Atmospheres* 106.D19, pp. 23073–23095. DOI: https://doi.org/10.1029/2001JD000807. URL: https://agupubs.onlinelibrary.wiley.com/doi/abs/10.1029/2001JD000807.

Bond, Tami C et al. (2013). "Bounding the role of black carbon in the climate system: A scientific assessment". In: *J. Geophys. Res.: Atmos.* 118.11, pp. 5380–5552. DOI: 10.1002/jgrd.50171. URL: https://doi.org/10.1002/jgrd.50171.

Bony, Sandrine et al. (2006). "How Well Do We Understand and Evaluate Climate Change Feedback Processes?" In: *J. Clim.* 19.15, pp. 3445 –3482. DOI: 10.1175/JCLI3819.1. URL: https://journals.ametsoc.org/view/journals/clim/19/15/jcli3819.1.xml.

Boucher, Olivier (1998). "On Aerosol Direct Shortwave Forcing and the Henyey–Greenstein Phase Function". In: *Journal of the Atmospheric Sciences* 55.1, pp. 128 –134. DOI: https://doi.org/10.1175/1520-0469(1998)055<0128:OADSFA>2.0.CO;2. URL: https://journals.ametsoc.org/view/journals/atsc/55/1/1520-0469_1998_055_0128_oadsfa_2.0.co_2.xml.

Box, Jason E et al. (2019). "Key indicators of Arctic climate change: 1971–2017". In: *Environmental Research Letters* 14.4, p. 045010. DOI: 10.1088/1748-9326/aafc1b. URL: https://dx.doi.org/10.1088/1748-9326/aafc1b.

Boyer, M. et al. (2022). "A full year of aerosol size distribution data from the central Arctic under an extreme positive Arctic Oscillation: Insights from the MOSAiC expedition". In: *Atmos. Chem. Phys. Discuss.* 2022, pp. 1–45. DOI: 10.5194/acp-2022-591.

Bozem, H. et al. (2019). "Characterization of transport regimes and the polar dome during Arctic spring and summer using in situ aircraft measurements". In: *Atmospheric Chemistry and Physics* 19.23, pp. 15049–15071. DOI: 10.5194/acp-19-15049-2019. URL: https://acp.copernicus.org/articles/19/15049/2019/.

Breider, Thomas J. et al. (2014). "Annual distributions and sources of Arctic aerosol components, aerosol optical depth, and aerosol absorption". In: *Journal of Geophysical Research: Atmospheres* 119.7, pp. 4107–4124. DOI: https://doi.org/10.1002/2013JD020996.

Bresson, H. et al. (2022). "Case study of a moisture intrusion over the Arctic with the ICOsahedral Non-hydrostatic (ICON) model: resolution dependence of its

representation". In: *Atmospheric Chemistry and Physics* 22.1, pp. 173–196. DOI: 10.5194/acp-22-173-2022.

Browse, J. et al. (2014). "The complex response of Arctic aerosol to sea-ice retreat". In: *Atmospheric Chemistry and Physics* 14, pp. 7543–7557. DOI: 10.5194/ACP-14-7543-2014.

Butler, A. H. et al. (2017). "A sudden stratospheric warming compendium". In: *Earth System Science Data* 9.1, pp. 63–76. DOI: 10.5194/essd-9-63-2017. URL: https://essd.copernicus.org/articles/9/63/2017/.

Candelone, Jean-Pierre et al. (1995). "Post-Industrial Revolution changes in large-scale atmospheric pollution of the northern hemisphere by heavy metals as documented in central Greenland snow and ice". In: *Journal of Geophysical Research: Atmospheres* 100.D8, pp. 16605–16616. DOI: https://doi.org/10.1029/95JD00989. URL: https://agupubs.onlinelibrary.wiley.com/doi/abs/10.1029/95JD00989.

Ceccherini, S. and M. Ridolfi (2010). "Technical Note: Variance-covariance matrix and averaging kernels for the Levenberg-Marquardt solution of the retrieval of atmospheric vertical profiles". In: *Atmos. Chem. Phys.* 10.6, pp. 3131–3139. DOI: 10.5194/acp-10-3131-2010. URL: https://acp.copernicus.org/articles/10/3131/2010/.

Chang, Hsueh-chia and TT Charalampopoulos (1990). "Determination of the wavelength dependence of refractive indices of flame soot". In: *Proc. R. Soc. London, Ser. A* 430.1880, pp. 577–591. URL: https://doi.org/10.1098/rspa.1990.0107.

Chao, Christopher Yu Hang and Man Pun Wan (2006). "A study of the dispersion of expiratory aerosols in unidirectional downward and ceiling-return type airflows using a multiphase approach." In: *Indoor air* 16 4, pp. 296–312. DOI: 10.1111/J.1600-0668.2006.00426.X.

Charlton, Andrew J. and Lorenzo M. Polvani (2007). "A New Look at Stratospheric Sudden Warmings. Part I: Climatology and Modeling Benchmarks". In: *Journal of Climate* 20.3, pp. 449 –469. DOI: 10.1175/JCLI3996.1. URL: https://journals.ametsoc.org/view/journals/clim/20/3/jcli3996.1.xml.

Chin, Mian et al. (2002). "Tropospheric Aerosol Optical Thickness from the GOCART Model and Comparisons with Satellite and Sun Photometer Measurements". In: *Journal of the Atmospheric Sciences* 59.3, pp. 461 –483. DOI: https://doi.org/10.1175/1520-0469(2002)059<0461:TAOTFT>2.0.CO;2.

Chin, Mian et al. (2004). "Aerosol distribution in the Northern Hemisphere during ACE-Asia: Results from global model, satellite observations, and Sun photometer measurements". In: *Journal of Geophysical Research: Atmospheres* 109.D23. DOI: https://doi.org/10.1029/2004JD004829. URL: https://agupubs.onlinelibrary.wiley.com/doi/abs/10.1029/2004JD004829.

Chung, Eui-Seok et al. (2021). "Cold-season Arctic amplification driven by Arctic ocean-mediated seasonal energy transfer". In: *Earth's Future* 9.2, e2020EF001898. DOI: https://doi.org/10.1029/2020EF001898.

Climate Change (IPCC), Intergovernmental Panel on (2023). "Short-lived Climate Forcers". In: *Climate Change 2021 – The Physical Science Basis: Working Group I Contribution to the Sixth Assessment Report of the Intergovernmental Panel on Climate Change*. Cambridge University Press, 817–922. DOI: 10.1017/9781009157896.008.

Clough, S.A. et al. (2005). "Atmospheric radiative transfer modeling: a summary of the AER codes". In: *J. Quant. Spectrosc. Radiat. Transfer* 91.2, pp. 233–244. ISSN: 0022-4073. DOI: https://doi.org/10.1016/j.jqsrt.2004.05.058.

Confer, K. et al. (2023). "Impact of Changing Arctic Sea Ice Extent, Sea Ice Age, and Snow Depth on Sea Salt Aerosol From Blowing Snow and the Open Ocean for

1980–2017". In: *Journal of Geophysical Research: Atmospheres* 128. DOI: 10.1029/2022JD037667.

Cox, Christopher J., Von P. Walden, and Penny M. Rowe (2012). "A comparison of the atmospheric conditions at Eureka, Canada, and Barrow, Alaska (2006–2008)". In: *Journal of Geophysical Research: Atmospheres* 117.D12. DOI: https://doi.org/10.1029/2011JD017164. URL: https://agupubs.onlinelibrary.wiley.com/doi/abs/10.1029/2011JD017164.

Cox, Christopher J et al. (2015). "Humidity trends imply increased sensitivity to clouds in a warming Arctic". In: *Nature Communications* 6.1, p. 10117. DOI: 10.1038/ncomms10117.

Cruz, Celia N and Spyros N Pandis (2000). "Deliquescence and hygroscopic growth of mixed inorganic- organic atmospheric aerosol". In: *Environmental Science & Technology* 34.20, pp. 4313–4319. DOI: 10.1021/es9907109.

Cziczo, DJ and JPD Abbatt (1999). "Deliquescence, efflorescence, and supercooling of ammonium sulfate aerosols at low temperature: Implications for cirrus cloud formation and aerosol phase in the atmosphere". In: *Journal of Geophysical Research: Atmospheres* 104.D11, pp. 13781–13790. DOI: https://doi.org/10.1029/1999JD900112.

Davis, Sumner P, Mark C Abrams, and James W Brault (2001). *Fourier transform spectrometry*. Elsevier.

De Mazière, M. et al. (2018). "The Network for the Detection of Atmospheric Composition Change (NDACC): history, status and perspectives". In: *Atmospheric Chemistry and Physics* 18.7, pp. 4935–4964. DOI: 10.5194/acp-18-4935-2018. URL: https://acp.copernicus.org/articles/18/4935/2018/.

DeMott, P. et al. (2003). "African dust aerosols as atmospheric ice nuclei". In: *Geophysical Research Letters* 30. DOI: 10.1029/2003GL017410.

Descamps, Sébastien et al. (2017). "Climate change impacts on wildlife in a High Arctic archipelago – Svalbard, Norway". In: *Global Change Biology* 23.2, pp. 490–502. DOI: https://doi.org/10.1111/gcb.13381. eprint: https://onlinelibrary.wiley.com/doi/pdf/10.1111/gcb.13381. URL: https://onlinelibrary.wiley.com/doi/abs/10.1111/gcb.13381.

Dimdore-Miles, O. et al. (2022). "Interactions between the stratospheric polar vortex and Atlantic circulation on seasonal to multi-decadal timescales". In: *Atmospheric Chemistry and Physics* 22.7, pp. 4867–4893. DOI: 10.5194/acp-22-4867-2022. URL: https://acp.copernicus.org/articles/22/4867/2022/.

Domine, F. et al. (2004). "The origin of sea salt in snow on Arctic sea ice and in coastal regions". In: *Atmos. Chem. Phys.* 4.9/10, pp. 2259–2271. DOI: 10.5194/acp-4-2259-2004. URL: https://acp.copernicus.org/articles/4/2259/2004/.

Donth, T. et al. (2020). "Combining atmospheric and snow radiative transfer models to assess the solar radiative effects of black carbon in the Arctic". In: *Atmos. Chem. Phys.* 20.13, pp. 8139–8156. DOI: 10.5194/acp-20-8139-2020. URL: https://acp.copernicus.org/articles/20/8139/2020/.

Durant, Adam J., Costanza Bonadonna, and Claire J. Horwell (Aug. 2010). "Atmospheric and Environmental Impacts of Volcanic Particulates". In: *Elements* 6.4, pp. 235–240. ISSN: 1811-5209. DOI: 10.2113/gselements.6.4.235.

Easterbrook, D.J. (2016). "Chapter 9 - Greenhouse Gases". In: *Evidence-Based Climate Science (Second Edition)*. Ed. by Don J. Easterbrook. Second Edition. Elsevier, pp. 163–173. ISBN: 978-0-12-804588-6. DOI: https://doi.org/10.1016/B978-0-12-804588-6.00009-4.

Ebell, K. et al. (2023). "Custom collection of classification data from Ny-Ålesund between 10 Jun 2016 and 31 Dec 2022". In: *ACTRIS Cloud remote sensing data centre unit (CLU)*. DOI: https://doi.org/10.60656/0f41eadb2ec84e4d.

Ebell, Kerstin, Sabrina Schnitt, and Pavel Krobot (2023). "Precipitation amount of Pluvio rain gauge at AWIPEV, Ny-Ålesund (2019)". In: In: Ebell, K et al. (2023): Precipitation amount of Pluvio rain gauge at AWIPEV, Ny-Ålesund (2017-2021). PANGAEA, https://doi.org/10.1594/PANGAEA.957612. PANGAEA. DOI: 10.1594/PANGAEA.957615. URL: https://doi.org/10.1594/PANGAEA.957615.

Ebell, Kerstin et al. (2020). "Radiative Effect of Clouds at Ny-Ålesund, Svalbard, as Inferred from Ground-Based Remote Sensing Observations". In: *Journal of Applied Meteorology and Climatology* 59.1, pp. 3 –22. DOI: 10.1175/JAMC-D-19-0080.1. URL: https://journals.ametsoc.org/view/journals/apme/59/1/jamc-d-19-0080.1.xml.

Eldridge, J.E. and Edward D. Palik (1997). "- Sodium Chloride (NaCl)". In: *Handbook of Optical Constants of Solids*. Ed. by Edward D. Palik. Burlington: Academic Press, pp. 775–793. ISBN: 978-0-12-544415-6. DOI: https://doi.org/10.1016/B978-012544415-6.50041-8. URL: https://www.sciencedirect.com/science/article/pii/B9780125444156500418.

Eliassen, Arnt (1961). "On the transfer of energy in stationary mountain waves." In: *Geofys. Publ.* 22, pp. 1–23.

Estillore, Armando D et al. (2017). "Linking hygroscopicity and the surface microstructure of model inorganic salts, simple and complex carbohydrates, and authentic sea spray aerosol particles". In: *Physical Chemistry Chemical Physics* 19.31, pp. 21101–21111. DOI: 10.1039/C7CP04051B.

Fairbridge, Rhodes W. (2005). "Ferrel Cell". In: *Encyclopedia of World Climatology*. Ed. by John E. Oliver. Dordrecht: Springer Netherlands, pp. 378–378. ISBN: 978-1-4020-3266-0. DOI: 10.1007/1-4020-3266-8_81. URL: https://doi.org/10.1007/1-4020-3266-8_81.

Fan, Jiwen et al. (2016). "Review of Aerosol–Cloud Interactions: Mechanisms, Significance, and Challenges". In: *J. Atmos. Sci.* 73.11, pp. 4221 –4252. DOI: 10.1175/JAS-D-16-0037.1. URL: https://journals.ametsoc.org/view/journals/atsc/73/11/jas-d-16-0037.1.xml.

Fandry, C. B. and L. M. Leslie (1984). "A Two-Layer Quasi-Geostrophic Model of Summer Trough Formation in the Australian Subtropical Easterlies". In: *Journal of Atmospheric Sciences* 41.5, pp. 807 –818. DOI: https://doi.org/10.1175/1520-0469(1984)041<0807:ATLQGM>2.0.CO;2. URL: https://journals.ametsoc.org/view/journals/atsc/41/5/1520-0469_1984_041_0807_atlqgm_2_0_co_2.xml.

Findeisen, Z (1938). "Kolloid meteorologische vorgange bei neiderschlags-bildung". In: *Meteorologische Zeitschrift* 55, p. 121.

Francis, D. et al. (2019). "A meandering polar jet caused the development of a Saharan cyclone and the transport of dust toward Greenland". In: *Advances in Science and Research* 16, pp. 49–56. DOI: 10.5194/asr-16-49-2019. URL: https://asr.copernicus.org/articles/16/49/2019/.

Francis, Diana et al. (2018). "Polar jet associated circulation triggered a Saharan cyclone and derived the poleward transport of the African dust generated by the cyclone". In: *J. Geophys. Res.: Atmos.* 123.21, pp. 11–899. DOI: 10.1029/2018JD029095. URL: https://doi.org/10.1029/2018JD029095.

Francis, Diana et al. (2022). "Atmospheric rivers drive exceptional Saharan dust transport towards Europe". In: *Atmospheric Research* 266, p. 105959. ISSN: 0169-8095. DOI: https://doi.org/10.1016/j.atmosres.2021.105959. URL: https://www.sciencedirect.com/science/article/pii/S0169809521005159.

Francis, Jennifer and Natasa Skific (2015). "Evidence linking rapid Arctic warming to mid-latitude weather patterns". In: *Philosophical Transactions of the Royal Society A: Mathematical, Physical and Engineering Sciences* 373.2045, p. 20140170.

Freudenthaler, Volker et al. (2009). "Depolarization ratio profiling at several wavelengths in pure Saharan dust during SAMUM 2006". In: *Tellus B* 61.1, pp. 165–179. DOI: 10.1111/j.1600-0889.2008.00396.x. URL: https://doi.org/10.1111/j.1600-0889.2008.00396.x.

Frey, L., F. A.-M. Bender, and G. Svensson (2017). "Cloud albedo changes in response to anthropogenic sulfate and non-sulfate aerosol forcings in CMIP5 models". In: *Atmospheric Chemistry and Physics* 17.14, pp. 9145–9162. DOI: 10.5194/acp-17-9145-2017. URL: https://acp.copernicus.org/articles/17/9145/2017/.

Frey, M. et al. (2019). "First direct observation of sea salt aerosol production from blowing snow above sea ice". In: *Atmospheric Chemistry and Physics*. DOI: 10.5194/acp-2019-259.

Frey, M. M. et al. (2020). "First direct observation of sea salt aerosol production from blowing snow above sea ice". In: *Atmospheric Chemistry and Physics* 20.4, pp. 2549–2578. DOI: 10.5194/acp-20-2549-2020. URL: https://acp.copernicus.org/articles/20/2549/2020/.

Fung, K. M. et al. (2022). "Exploring dimethyl sulfide (DMS) oxidation and implications for global aerosol radiative forcing". In: *Atmospheric Chemistry and Physics* 22.2, pp. 1549–1573. DOI: 10.5194/acp-22-1549-2022. URL: https://acp.copernicus.org/articles/22/1549/2022/.

Gascard, J.-C., J. Zhang, and M. Rafizadeh (2019). "Rapid decline of Arctic sea ice volume: Causes and consequences". In: *The Cryosphere Discussions* 2019, pp. 1–29. DOI: 10.5194/tc-2019-2. URL: https://tc.copernicus.org/preprints/tc-2019-2/.

Ge, Zhaozhu, Anthony S Wexler, and Murray V Johnston (1998). "Deliquescence behavior of multicomponent aerosols". In: *The Journal of Physical Chemistry A* 102.1, pp. 173–180. DOI: 10.1021/jp972396f.

Gelaro, Ronald et al. (2017). "The Modern-Era Retrospective Analysis for Research and Applications, Version 2 (MERRA-2)". In: *J. Clim.* 30.14, pp. 5419 –5454. DOI: 10.1175/JCLI-D-16-0758.1. URL: https://journals.ametsoc.org/view/journals/clim/30/14/jcli-d-16-0758.1.xml.

Giles, D. M. et al. (2019). "Advancements in the Aerosol Robotic Network (AERONET) Version 3 database – automated near-real-time quality control algorithm with improved cloud screening for Sun photometer aerosol optical depth (AOD) measurements". In: *Atmospheric Measurement Techniques* 12.1, pp. 169–209. DOI: 10.5194/amt-12-169-2019. URL: https://amt.copernicus.org/articles/12/169/2019/.

Ginoux, Paul et al. (2001). "Sources and distributions of dust aerosols simulated with the GOCART model". In: *Journal of Geophysical Research: Atmospheres* 106.D17, pp. 20255–20273. DOI: https://doi.org/10.1029/2000JD000053. URL: https://agupubs.onlinelibrary.wiley.com/doi/abs/10.1029/2000JD000053.

Gong, Xianda et al. (2023). "Arctic warming by abundant fine sea salt aerosols from blowing snow". In: *Nature Geoscience* 16.9, pp. 768–774. ISSN: 1752-0908. DOI: 10.1038/s41561-023-01254-8.

Gralton, Jan et al. (2011). "The role of particle size in aerosolised pathogen transmission: a review". In: *Journal of infection* 62.1, pp. 1–13. DOI: 10.1016/j.jinf.2010.11.010.

Graney, Christopher M. (Aug. 2011). "Coriolis effect, two centuries before Coriolis". In: *Physics Today* 64.8, pp. 8–9. ISSN: 0031-9228. DOI: 10.1063/PT.3.1195. eprint: https://pubs.aip.org/physicstoday/article-pdf/64/8/8/10093931/8_2_online.pdf. URL: https://doi.org/10.1063/PT.3.1195.

Graversen, Rune G., Peter L. Langen, and Thorsten Mauritsen (2014). "Polar Amplification in CCSM4: Contributions from the Lapse Rate and Surface Albedo

Feedbacks". In: *J. Clim.* 27.12, pp. 4433 –4450. DOI: 10.1175/JCLI-D-13-00551.1. URL: https://journals.ametsoc.org/view/journals/clim/27/12/jcli-d-13-00551.1.xml.

Groot Zwaaftink, C. D. et al. (2016a). "Substantial contribution of northern high-latitude sources to mineral dust in the Arctic". In: *Journal of Geophysical Research: Atmospheres* 121.22, pp. 13,678–13,697. DOI: https://doi.org/10.1002/2016JD025482. URL: https://agupubs.onlinelibrary.wiley.com/doi/abs/10.1002/2016JD025482.

— (2016b). "Substantial contribution of northern high-latitude sources to mineral dust in the Arctic". In: *J. Geophys. Res.: Atmos.* 121.22, pp. 13,678–13,697. DOI: https://doi.org/10.1002/2016JD025482. eprint: https://agupubs.onlinelibrary.wiley.com/doi/pdf/10.1002/2016JD025482. URL: https://agupubs.onlinelibrary.wiley.com/doi/abs/10.1002/2016JD025482.

Hadley, George (1735). "VI. Concerning the cause of the general trade-winds". In: *Philosophical Transactions of the Royal Society of London* 39.437, pp. 58–62. DOI: 10.1098/rstl.1735.0014. URL: https://royalsocietypublishing.org/doi/abs/10.1098/rstl.1735.0014.

Hand, J. L. et al. (2012). "Particulate sulfate ion concentration and SO_2 emission trends in the United States from the early 1990s through 2010". In: *Atmospheric Chemistry and Physics* 12.21, pp. 10353–10365. DOI: 10.5194/acp-12-10353-2012. URL: https://acp.copernicus.org/articles/12/10353/2012/.

Hansen, Brage B et al. (2014). "Warmer and wetter winters: characteristics and implications of an extreme weather event in the High Arctic". In: *Environmental Research Letters* 9.11, p. 114021. DOI: 10.1088/1748-9326/9/11/114021. URL: https://dx.doi.org/10.1088/1748-9326/9/11/114021.

Hartog, Jeroen J. de et al. (2005). "Relationship between different size classes of particulate matter and meteorology in three European cities". In: *J. Environ. Monit.* 7 (4), pp. 302–310. DOI: 10.1039/B415153D. URL: http://dx.doi.org/10.1039/B415153D.

Haywood, James and Olivier Boucher (2000). "Estimates of the direct and indirect radiative forcing due to tropospheric aerosols: A review". In: *Reviews of Geophysics* 38.4, pp. 513–543. DOI: https://doi.org/10.1029/1999RG000078.

Hersbach, H et al. (2018). "ERA5 hourly data on pressure levels from 1979 to present". In: *Copernicus climate change service (c3s) climate data store (cds). (Accessed on < 01-12-2022 >)* 10. DOI: 10.24381/cds.bd0915c6.

Hersbach, H. et al. (2023). "ERA5 monthly mean data on pressure levels from 1940 to present". In: *Copernicus climate change service (c3s) climate data store (cds). (Accessed on < 01-12-2022 >)* 10. DOI: 10.24381/cds.6860a573.

Heslin-Rees, D. et al. (2020). "From a polar to a marine environment: has the changing Arctic led to a shift in aerosol light scattering properties?" In: *Atmospheric Chemistry and Physics* 20.21, pp. 13671–13686. DOI: 10.5194/acp-20-13671-2020.

Hinds, William C and Yifang Zhu (2022). *Aerosol technology: properties, behavior, and measurement of airborne particles*. John Wiley & Sons.

Holben, B.N. et al. (1998). "AERONET—A Federated Instrument Network and Data Archive for Aerosol Characterization". In: *Remote Sensing of Environment* 66.1, pp. 1–16. ISSN: 0034-4257. DOI: https://doi.org/10.1016/S0034-4257(98)00031-5. URL: https://www.sciencedirect.com/science/article/pii/S0034425798000315.

Horowitz, Hannah M. et al. (2020). "Effects of Sea Salt Aerosol Emissions for Marine Cloud Brightening on Atmospheric Chemistry: Implications for Radiative Forcing". In: *Geophysical Research Letters* 47.4, e2019GL085838. DOI: https://doi.

org/10.1029/2019GL085838. URL: https://agupubs.onlinelibrary.wiley.com/doi/abs/10.1029/2019GL085838.

Hosseini, Sayyed Mohammad, Abdolreza Kashki, and Mokhtar Karami (2022). "Analysis of the North Atlantic Oscillation Index and rainfall in Iran". In: *Modeling Earth Systems and Environment*, pp. 1–10. DOI: 10.1007/s40808-021-01309-y.

Huang, J. and L. Jaeglé (2017). "Wintertime enhancements of sea salt aerosol in polar regions consistent with a sea ice source from blowing snow". In: *Atmospheric Chemistry and Physics* 17.5, pp. 3699–3712. DOI: 10.5194/acp-17-3699-2017.

Hurrell, James W. et al. (2003). "An Overview of the North Atlantic Oscillation". In: *The North Atlantic Oscillation: Climatic Significance and Environmental Impact*. American Geophysical Union (AGU), pp. 1–35. ISBN: 9781118669037. DOI: https://doi.org/10.1029/134GM01. eprint: https://agupubs.onlinelibrary.wiley.com/doi/pdf/10.1029/134GM01. URL: https://agupubs.onlinelibrary.wiley.com/doi/abs/10.1029/134GM01.

Hussein, Tareq et al. (2004). "Urban aerosol number size distributions". In: *Atmospheric Chemistry and Physics* 4.2, pp. 391–411.

Illingworth, AJ et al. (2007). "Cloudnet: Continuous evaluation of cloud profiles in seven operational models using ground-based observations". In: *Bulletin of the American Meteorological Society* 88.6, pp. 883–898. DOI: https://doi.org/10.1175/BAMS-88-6-883.

Ji, Denghui et al. (2023). "Ground-based remote sensing of aerosol properties using high-resolution infrared emission and lidar observations in the High Arctic." In: *Atmospheric Measurement Techniques* 16.7. DOI: 10.5194/amt-16-1865-2023.

Jung, Chang Hoon et al. (2018). "The seasonal characteristics of cloud condensation nuclei (CCN) in the arctic lower troposphere". In: *Tellus B: Chemical and Physical Meteorology* 70.1, pp. 1–13. DOI: 10.1080/16000889.2018.1513291.

Kim, Dongchul et al. (2014). "The responses of cloudiness to the direct radiative effect of sulfate and carbonaceous aerosols". In: *Journal of Geophysical Research: Atmospheres* 119.3, pp. 1172–1185. DOI: https://doi.org/10.1002/2013JD020529. URL: https://agupubs.onlinelibrary.wiley.com/doi/abs/10.1002/2013JD020529.

King, Andrew D. et al. (2019). "Observed Relationships Between Sudden Stratospheric Warmings and European Climate Extremes". In: *Journal of Geophysical Research: Atmospheres* 124.24, pp. 13943–13961. DOI: https://doi.org/10.1029/2019JD030480. URL: https://agupubs.onlinelibrary.wiley.com/doi/abs/10.1029/2019JD030480.

Kirpes, R. M. et al. (2018). "Secondary sulfate is internally mixed with sea spray aerosol and organic aerosol in the winter Arctic". In: *Atmospheric Chemistry and Physics* 18.6, pp. 3937–3949. DOI: 10.5194/acp-18-3937-2018.

Knoblauch, Christian et al. (2018). "Methane production as key to the greenhouse gas budget of thawing permafrost". In: *Nature Climate Change* 8.4, pp. 309–312. DOI: 10.1038/s41558-018-0095-z.

Koch, Dorothy et al. (2011). "Coupled Aerosol-Chemistry–Climate Twentieth-Century Transient Model Investigation: Trends in Short-Lived Species and Climate Responses". In: *J. Clim.* 24.11, pp. 2693 –2714. DOI: 10.1175/2011JCLI3582.1. URL: https://journals.ametsoc.org/view/journals/clim/24/11/2011jcli3582.1.xml.

Kodros, J. K. et al. (2018). "Size-resolved mixing state of black carbon in the Canadian high Arctic and implications for simulated direct radiative effect". In: *Atmos. Chem. Phys.* 18.15, pp. 11345–11361. DOI: 10.5194/acp-18-11345-2018. URL: https://acp.copernicus.org/articles/18/11345/2018/.

Koehler, K. A. et al. (2010). "Laboratory investigations of the impact of mineral dust aerosol on cold cloud formation". In: *Atmospheric Chemistry and Physics* 10.23, pp. 11955–11968. DOI: 10.5194/acp-10-11955-2010. URL: https://acp.copernicus.org/articles/10/11955/2010/.

Kok, J. F. et al. (2021). "Contribution of the world's main dust source regions to the global cycle of desert dust". In: *Atmospheric Chemistry and Physics* 21.10, pp. 8169–8193. DOI: 10.5194/acp-21-8169-2021. URL: https://acp.copernicus.org/articles/21/8169/2021/.

Krinner, Gerhard, Olivier Boucher, and Yves Balkanski (2006). "Ice-free glacial northern Asia due to dust deposition on snow". In: *Climate Dynamics* 27.6, pp. 613–625. DOI: 10.1007/s00382-006-0159-z. URL: https://doi.org/10.1007/s00382-006-0159-z.

Kristiansen, N. et al. (2015). "Evaluation of observed and modelled aerosol lifetimes using radioactive tracers of opportunity and an ensemble of 19 global models". In: *Atmospheric Chemistry and Physics* 16, pp. 3525–3561. DOI: 10.5194/ACP-16-3525-2016.

Lang, Kenneth R. (2013). "Light of the Sun". In: *The Life and Death of Stars*. Cambridge University Press, 1–17. DOI: 10.1017/CBO9781139061025.002.

Lee, Sang-Moo et al. (2021). "Winter Snow Depth on Arctic Sea Ice From Satellite Radiometer Measurements (2003–2020): Regional Patterns and Trends". In: *Geophys. Res. Lett.* 48.15. e2021GL094541 2021GL094541, e2021GL094541. DOI: https://doi.org/10.1029/2021GL094541. eprint: https://agupubs.onlinelibrary.wiley.com/doi/pdf/10.1029/2021GL094541. URL: https://agupubs.onlinelibrary.wiley.com/doi/abs/10.1029/2021GL094541.

Lee, Simon H., Lorenzo M. Polvani, and Bin Guan (2022). "Modulation of Atmospheric Rivers by the Arctic Stratospheric Polar Vortex". In: *Geophysical Research*

Letters 49.18. e2022GL100381 2022GL100381, e2022GL100381. DOI: https://doi.org/10.1029/2022GL100381. eprint: https://agupubs.onlinelibrary.wiley.com/doi/pdf/10.1029/2022GL100381. URL: https://agupubs.onlinelibrary.wiley.com/doi/abs/10.1029/2022GL100381.

Lenaerts, Jan TM et al. (2017). "Polar clouds and radiation in satellite observations, reanalyses, and climate models". In: *Geophysical Research Letters* 44.7, pp. 3355–3364. DOI: https://doi.org/10.1002/2016GL072242.

Lewis, Ernie R and Stephen E Schwartz (2004). *Sea salt aerosol production: mechanisms, methods, measurements, and models*. Vol. 152. American geophysical union.

Li, Jing et al. (2022). "Scattering and absorbing aerosols in the climate system". In: *Nature Reviews Earth & Environment* 3.6, pp. 363–379. DOI: 10.1038/s43017-022-00296-7.

Lillard, R. S. et al. (Mar. 2009a). "Assessment of Corrosion-Based Failure in Stainless Steel Containers Used for the Long-Term Storage of Plutonium-Based Salts". In: *Corrosion* 65.3, pp. 175–186. ISSN: 0010-9312. DOI: 10.5006/1.3319126.

— (Mar. 2009b). "Assessment of Corrosion-Based Failure in Stainless Steel Containers Used for the Long-Term Storage of Plutonium-Based Salts". In: *Corrosion* 65.3, pp. 175–186. ISSN: 0010-9312. DOI: 10.5006/1.3319126.

Lim, Eun-Pa et al. (2021). "The 2019 Southern Hemisphere Stratospheric Polar Vortex Weakening and Its Impacts". In: *Bulletin of the American Meteorological Society* 102.6, E1150 –E1171. DOI: https://doi.org/10.1175/BAMS-D-20-0112.1. URL: https://journals.ametsoc.org/view/journals/bams/102/6/BAMS-D-20-0112.1.xml.

Liu, Nana et al. (2022). "Characteristics of Aerosol Extinction Hygroscopic Growth in the Typical Coastal City of Qingdao, China". In: *Remote. Sens.* 14, p. 6288. DOI: 10.3390/rs14246288.

Lohmann, U. and J. Feichter (2005). "Global indirect aerosol effects: a review". In: *Atmospheric Chemistry and Physics* 5.3, pp. 715–737. DOI: 10.5194/acp-5-715-2005. URL: https://acp.copernicus.org/articles/5/715/2005/.

Lohmann, Ulrike et al. (2010). "Total aerosol effect: radiative forcing or radiative flux perturbation?" In: *Atmospheric Chemistry and Physics* 10.7, pp. 3235–3246. DOI: 10.5194/acp-10-3235-2010.

Lorenz, Louis (1890). *Lysbevægelsen i og uden for en af plane Lysbølger belyst Kugle*. na.

Lourakis, Manolis IA et al. (2005). "A brief description of the Levenberg-Marquardt algorithm implemented by levmar". In: *Foundation of Research and Technology* 4.1, pp. 1–6.

Ma, Shuaishuai et al. (2021). "A review of efflorescence kinetics studies on atmospherically relevant particles". In: *Chemosphere* 277, p. 130320. ISSN: 0045-6535. DOI: https://doi.org/10.1016/j.chemosphere.2021.130320. URL: https://www.sciencedirect.com/science/article/pii/S0045653521007906.

Mahmood, R. et al. (2019). "Sensitivity of Arctic sulfate aerosol and clouds to changes in future surface seawater dimethylsulfide concentrations". In: *Atmospheric Chemistry and Physics* 19.9, pp. 6419–6435. DOI: 10.5194/acp-19-6419-2019. URL: https://acp.copernicus.org/articles/19/6419/2019/.

Manktelow, P. et al. (2007). "Regional and global trends in sulfate aerosol since the 1980s". In: *Geophysical Research Letters* 34. DOI: 10.1029/2006GL028668.

Markowicz, Krzysztof M. et al. (2003). "Clear-sky infrared aerosol radiative forcing at the surface and the top of the atmosphere". In: *Quarterly Journal of the Royal Meteorological Society* 129.594, pp. 2927–2947. DOI: https://doi.org/10.1256/qj.02.224.

Marquardt, Donald W (1963). "An algorithm for least-squares estimation of non-linear parameters". In: *Journal of the society for Industrial and Applied Mathematics* 11.2, pp. 431–441. DOI: 10.1137/0111030.

Martin, Scot T (2000). "Phase transitions of aqueous atmospheric particles". In: *Chemical Reviews* 100.9, pp. 3403–3454. DOI: https://doi.org/10.1021/cr990034t.

Maturilli, Marion (2020). *Basic and other measurements of radiation at station Ny-Ålesund (2006-05 et seq)*. data set. Alfred Wegener Institute - Research Unit Potsdam. DOI: 10.1594/PANGAEA.914927. URL: https://doi.org/10.1594/PANGAEA.914927.

Maturilli, Marion and Erik Dünschede (2023). *Homogenized radiosonde record at station Ny-Ålesund, Spitsbergen, 2017-2022*. data set. DOI: 10.1594/PANGAEA.961203. URL: https://doi.org/10.1594/PANGAEA.961203.

Maturilli, Marion, Andreas Herber, and Gert König-Langlo (2015). "Surface radiation climatology for Ny-Ålesund, Svalbard (78.9 N), basic observations for trend detection". In: *Theoretical and Applied Climatology* 120, pp. 331–339. DOI: 10.1007/s00704-014-1173-4.

Mauritsen, Thorsten et al. (2011). "An Arctic CCN-limited cloud-aerosol regime". In: *Atmospheric Chemistry and Physics* 11.1, pp. 165–173. DOI: 10.5194/acp-11-165-2011.

May, NW et al. (2016). "Multiyear study of the dependence of sea salt aerosol on wind speed and sea ice conditions in the coastal Arctic". In: *J. Geophys. Res.: Atmos.* 121.15, pp. 9208–9219. DOI: 10.1002/2016JD025273. URL: https://doi.org/10.1002/2016JD025273.

Mészáros, Agnes and K Vissy (1974). "Concentration, size distribution and chemical nature of atmospheric aerosol particles in remote oceanic areas". In: *Journal of Aerosol Science* 5.1, pp. 101–109.

Michelson, Albert A (1891). "XXVIII. Visibility of interference-fringes in the focus of a telescope". In: *The London, Edinburgh, and Dublin Philosophical Magazine and Journal of Science* 31.190, pp. 256–259.

Mie, Gustav (1908). "Beiträge zur Optik trüber Medien, speziell kolloidaler Metallösungen". In: *Annalen der Physik* 330.3, pp. 377–445. DOI: https://doi.org/10.1002/andp.19083300302. eprint: https://onlinelibrary.wiley.com/doi/pdf/10.1002/andp.19083300302. URL: https://onlinelibrary.wiley.com/doi/abs/10.1002/andp.19083300302.

Ming, Jing et al. (2009). "Black Carbon (BC) in the snow of glaciers in west China and its potential effects on albedos". In: *Atmos. Res.* 92.1, pp. 114–123. ISSN: 0169-8095. DOI: https://doi.org/10.1016/j.atmosres.2008.09.007. URL: https://www.sciencedirect.com/science/article/pii/S0169809508002445.

Mishchenko, Michael I. et al. (1999). "Bidirectional reflectance of flat, optically thick particulate layers: an efficient radiative transfer solution and applications to snow and soil surfaces". In: *Journal of Quantitative Spectroscopy and Radiative Transfer* 63.2, pp. 409–432. ISSN: 0022-4073. DOI: https://doi.org/10.1016/S0022-4073(99)00028-X. URL: https://www.sciencedirect.com/science/article/pii/S002240739900028X.

Ning, Liang and Raymond S. Bradley (2015). "Winter Climate Extremes over the Northeastern United States and Southeastern Canada and Teleconnections with Large-Scale Modes of Climate Variability". In: *Journal of Climate* 28.6, pp. 2475–2493. DOI: 10.1175/JCLI-D-13-00750.1. URL: https://journals.ametsoc.org/view/journals/clim/28/6/jcli-d-13-00750.1.xml.

Nomokonova, Tatiana, Christoph Ritter, and Kerstin Ebell (2019). *HATPRO microwave radiometer measurements at AWIPEV, Ny-Ålesund (2016-2018)*. data set. DOI: 10.1594/PANGAEA.902183. URL: https://doi.org/10.1594/PANGAEA.902183.

Onasch, Timothy B et al. (1999). "Infrared spectroscopic study of the deliquescence and efflorescence of ammonium sulfate aerosol as a function of temperature". In: *Journal of Geophysical Research: Atmospheres* 104.D17, pp. 21317–21326. DOI: https://doi.org/10.1029/1999JD900384.

Palik, Edward D. (1997). "- Gallium Arsenide (GaAs)". In: *Handbook of Optical Constants of Solids*. Ed. by Edward D. Palik. Burlington: Academic Press, pp. 429–443. ISBN: 978-0-12-544415-6. DOI: https://doi.org/10.1016/B978-012544415-6.50018-2. URL: https://www.sciencedirect.com/science/article/pii/B9780125444156500182.

Park, J. et al. (2020). "Shipborne observations reveal contrasting Arctic marine, Arctic terrestrial and Pacific marine aerosol properties". In: *Atmos. Chem. Phys.* 20.9, pp. 5573–5590. DOI: 10.5194/acp-20-5573-2020. URL: https://acp.copernicus.org/articles/20/5573/2020/.

Pasquier, J. T. et al. (2022). "The Ny-Ålesund Aerosol Cloud Experiment (NASCENT): Overview and First Results". In: *Bulletin of the American Meteorological Society* 103.11, E2533 –E2558. DOI: 10.1175/BAMS-D-21-0034.1. URL: https://journals.ametsoc.org/view/journals/bams/103/11/BAMS-D-21-0034.1.xml.

Pateraki, St. et al. (2012). "The role of meteorology on different sized aerosol fractions (PM10, PM2.5, PM2.5–10)". In: *Science of The Total Environment* 419, pp. 124–135. ISSN: 0048-9697. DOI: https://doi.org/10.1016/j.scitotenv.2011.12.064. URL: https://www.sciencedirect.com/science/article/pii/S0048969711015300.

Peace, AH et al. (2020). "Effect of aerosol radiative forcing uncertainty on projected exceedance year of a 1.5° C global temperature rise". In: *Environmental Research Letters* 15.9, 0940a6. DOI: 10.1088/1748-9326/aba20c.

Peng, Chao, Lanxiadi Chen, and Mingjin Tang (2022). "A database for deliquescence and efflorescence relative humidities of compounds with atmospheric relevance". In: *Fundamental Research* 2.4, pp. 578–587. ISSN: 2667-3258. DOI: https://doi.org/10.1016/j.fmre.2021.11.021.

Pernov, Jakob Boyd et al. (2022). "Increased aerosol concentrations in the High Arctic attributable to changing atmospheric transport patterns". In: *npj Climate and Atmospheric Science* 5.1, p. 62. DOI: 10.1038/s41612-022-00286-y.

Petters, M. D. and S. M. Kreidenweis (2007). "A single parameter representation of hygroscopic growth and cloud condensation nucleus activity". In: *Atmospheric Chemistry and Physics* 7.8, pp. 1961–1971. DOI: 10.5194/acp-7-1961-2007.

Philipp, Daniel, Martin Stengel, and Bodo Ahrens (2020). "Analyzing the Arctic Feedback Mechanism between Sea Ice and Low-Level Clouds Using 34 Years of Satellite Observations". In: *J. Clim.* 33.17, pp. 7479 –7501. DOI: 10.1175/JCLI-D-19-0895.1. URL: https://journals.ametsoc.org/view/journals/clim/33/17/jcliD190895.xml.

Previdi, Michael, Karen L Smith, and Lorenzo M Polvani (2021). "Arctic amplification of climate change: a review of underlying mechanisms". In: *Environ. Res. Lett.* 16.9, p. 093003. DOI: 10.1088/1748-9326/ac1c29.

Raoult, F-M (1889). "Recherches expérimentales sur les tensions de vapeur des dissolutions". In: *J. Phys. Theor. Appl.* 8.1, pp. 5–20. DOI: 10.1051/jphystap:0188900800500.

Raoult, Francois-Marie (1887). "Loi générale des tensions de vapeur des dissolvants". In: *CR Hebd. Seances Acad. Sci* 104, pp. 1430–1433.

Rap, Alexandru et al. (2013). "Natural aerosol direct and indirect radiative effects". In: *Geophysical Research Letters* 40.12, pp. 3297–3301. DOI: https://doi.org/10.1002/grl.50441. eprint: https://agupubs.onlinelibrary.wiley.com/doi/

pdf/10.1002/grl.50441. URL: https://agupubs.onlinelibrary.wiley.com/doi/abs/10.1002/grl.50441.

Read, P.L. (2011). "Dynamics and circulation regimes of terrestrial planets". In: *Planetary and Space Science* 59.10. Comparative Planetology: Venus-Earth-Mars, pp. 900–914. ISSN: 0032-0633. DOI: https://doi.org/10.1016/j.pss.2010.04.024. URL: https://www.sciencedirect.com/science/article/pii/S0032063310001364.

Ren, L. et al. (2020). "Source attribution of Arctic black carbon and sulfate aerosols and associated Arctic surface warming during 1980–2018". In: *Atmos. Chem. Phys.* 20.14, pp. 9067–9085. DOI: 10.5194/acp-20-9067-2020. URL: https://acp.copernicus.org/articles/20/9067/2020/.

Revercomb, Henry E. et al. (Aug. 1988). "Radiometric calibration of IR Fourier transform spectrometers: solution to a problem with the High-Resolution Interferometer Sounder". In: *Appl. Opt.* 27.15, pp. 3210–3218. DOI: 10.1364/AO.27.003210. URL: http://opg.optica.org/ao/abstract.cfm?URI=ao-27-15-3210.

Ricchiazzi, Paul et al. (1998). "SBDART: A Research and Teaching Software Tool for Plane-Parallel Radiative Transfer in the Earth's Atmosphere". In: *Bulletin of the American Meteorological Society* 79.10, pp. 2101 –2114. DOI: https://doi.org/10.1175/1520-0477(1998)079<2101:SARATS>2.0.CO;2.

Richter, P. et al. (2022). "A dataset of microphysical cloud parameters, retrieved from Fourier-transform infrared (FTIR) emission spectra measured in Arctic summer 2017". In: *Earth Syst. Sci. Data* 14.6, pp. 2767–2784. DOI: 10.5194/essd-14-2767-2022. URL: https://essd.copernicus.org/articles/14/2767/2022/.

Ritter, C. et al. (2016). "2014 iAREA campaign on aerosol in Spitsbergen – Part 2: Optical properties from Raman-lidar and in-situ observations at Ny-Ålesund". In: *Atmospheric Environment* 141, pp. 1–19. ISSN: 1352-2310. DOI: https://doi.

org/10.1016/j.atmosenv.2016.05.053. URL: https://www.sciencedirect.com/science/article/pii/S1352231016304010.

Rodda, C., U. Harlander, and M. Vincze (2022). "Jet stream variability in a polar warming scenario – a laboratory perspective". In: *Weather and Climate Dynamics* 3.3, pp. 937–950. DOI: 10.5194/wcd-3-937-2022. URL: https://wcd.copernicus.org/articles/3/937/2022/.

Rodgers, Clive D (2000). *Inverse methods for atmospheric sounding: theory and practice*. Vol. 2. World scientific.

Rowe, P. M., S. Neshyba, and V. P. Walden (2013). "Radiative consequences of low-temperature infrared refractive indices for supercooled water clouds". In: *Atmos. Chem. Phys.* 13.23, pp. 11925–11933. DOI: 10.5194/acp-13-11925-2013. URL: https://acp.copernicus.org/articles/13/11925/2013/.

Sato, Tomonori et al. (2022). "Enhanced Arctic moisture transport toward Siberia in autumn revealed by tagged moisture transport model experiment". In: *npj Climate and Atmospheric Science* 5.1, p. 91. DOI: 10.1038/s41612-022-00310-1.

Schmale, Julia, Paul Zieger, and Annica ML Ekman (2021). "Aerosols in current and future Arctic climate". In: *Nat. Clim. Change* 11.2, pp. 95–105. DOI: 10.1038/s41558-020-00969-5. URL: https://doi.org/10.1038/s41558-020-00969-5.

Schmeisser, L. et al. (2018). "Seasonality of aerosol optical properties in the Arctic". In: *Atmos. Chem. Phys.* 18.16, pp. 11599–11622. DOI: 10.5194/acp-18-11599-2018. URL: https://acp.copernicus.org/articles/18/11599/2018/.

Schulz, H. et al. (2019). "High Arctic aircraft measurements characterising black carbon vertical variability in spring and summer". In: *Atmos. Chem. Phys.* 19.4, pp. 2361–2384. DOI: 10.5194/acp-19-2361-2019. URL: https://acp.copernicus.org/articles/19/2361/2019/.

Serreze, Mark C. and Roger G. Barry (2011). "Processes and impacts of Arctic amplification: A research synthesis". In: *Global and Planetary Change* 77.1, pp. 85–96. ISSN: 0921-8181. DOI: https://doi.org/10.1016/j.gloplacha.2011.03.004. URL: https://www.sciencedirect.com/science/article/pii/S0921818111000397.

Shaw, Glenn E. (1995). "The Arctic Haze Phenomenon". In: *Bull. Am. Meteorol. Soc.* 76.12, pp. 2403 –2414. DOI: 10.1175/1520-0477(1995)076<2403:TAHP>2.0.CO;2. URL: https://journals.ametsoc.org/view/journals/bams/76/12/1520-0477_1995_076_2403_tahp_2_0_co_2.xml.

Soden, Brian J. and Isaac M. Held (2006). "An Assessment of Climate Feedbacks in Coupled Ocean–Atmosphere Models". In: *J. Clim.* 19.14, pp. 3354 –3360. DOI: 10.1175/JCLI3799.1. URL: https://journals.ametsoc.org/view/journals/clim/19/14/jcli3799.1.xml.

Spänkuch, D, W Döhler, and J Güldner (2000). "Effect of coarse biogenic aerosol on downwelling infrared flux at the surface". In: *Journal of Geophysical Research: Atmospheres* 105.D13, pp. 17341–17350. DOI: https://doi.org/10.1029/2000JD900173.

Stamnes, Knut et al. (June 1988). "Numerically stable algorithm for discrete-ordinate-method radiative transfer in multiple scattering and emitting layered media". In: *Appl. Opt.* 27.12, pp. 2502–2509. DOI: 10.1364/AO.27.002502. URL: http://opg.optica.org/ao/abstract.cfm?URI=ao-27-12-2502.

Stevenson, David S. (2019). "Atmospheric Circulation and Climate". In: *Red Dwarfs: Their Geological, Chemical, and Biological Potential for Life*. Cham: Springer International Publishing, pp. 171–218. ISBN: 978-3-030-25550-3. DOI: 10.1007/978-3-030-25550-3_5. URL: https://doi.org/10.1007/978-3-030-25550-3_5.

Stone, R. S. et al. (2007). "Incursions and radiative impact of Asian dust in northern Alaska". In: *Geophysical Research Letters* 34.14. DOI: https://doi.org/10.1029/2007GL029878.

Struthers, H. et al. (2011). "The effect of sea ice loss on sea salt aerosol concentrations and the radiative balance in the Arctic". In: *Atmos. Chem. Phys.* 11.7, pp. 3459–3477. DOI: 10.5194/acp-11-3459-2011. URL: https://acp.copernicus.org/articles/11/3459/2011/.

Sun, Jiming and Parisa A. Ariya (2006). "Atmospheric organic and bio-aerosols as cloud condensation nuclei (CCN): A review". In: *Atmospheric Environment* 40.5, pp. 795–820. ISSN: 1352-2310. DOI: https://doi.org/10.1016/j.atmosenv.2005.05.052. URL: https://www.sciencedirect.com/science/article/pii/S135223100500498X.

Tang, Ignatius N. and Harry R. Munkelwitz (1993). "Composition and temperature dependence of the deliquescence properties of hygroscopic aerosols". In: *Atmospheric Environment. Part A. General Topics* 27.4, pp. 467–473. ISSN: 0960-1686. DOI: https://doi.org/10.1016/0960-1686(93)90204-C.

Taylor, Patrick C. et al. (2013). "A Decomposition of Feedback Contributions to Polar Warming Amplification". In: *J. Clim.* 26.18, pp. 7023 –7043. DOI: 10.1175/JCLI-D-12-00696.1. URL: https://journals.ametsoc.org/view/journals/clim/26/18/jcli-d-12-00696.1.xml.

Thandlam, Venugopal, Anna Rutgersson, and Erik Sahlee (2022). "Spatio-temporal variability of atmospheric rivers and associated atmospheric parameters in the Euro-Atlantic region". In: *Theoretical and Applied Climatology*, pp. 1–21. DOI: 10.1007/s00704-021-03776-w.

Theophanides, Theophile (2012). "Introduction to infrared spectroscopy". In: *Infrared Spectroscopy-Materials Science, Engineering and Technology*, pp. 1–10.

Thomson, William (1872). "On the equilibrium of vapour at a curved surface of liquid". In: *Proceedings of the Royal Society of Edinburgh* 7, pp. 63–68.

Thornhill, G. D. et al. (2021). "Effective radiative forcing from emissions of reactive gases and aerosols – a multi-model comparison". In: *Atmospheric Chemistry and Physics* 21.2, pp. 853–874. DOI: 10.5194/acp-21-853-2021. URL: https://acp.copernicus.org/articles/21/853/2021/.

Tian, Y. et al. (2023). "Understanding variations in downwelling longwave radiation using Brutsaert's equation". In: *Earth System Dynamics* 14.6, pp. 1363–1374. DOI: 10.5194/esd-14-1363-2023. URL: https://esd.copernicus.org/articles/14/1363/2023/.

Tomasi, Claudio and Angelo Lupi (2017). "Primary and Secondary Sources of Atmospheric Aerosol". In: *Atmospheric Aerosols*. John Wiley & Sons, Ltd. Chap. 1, pp. 1–86. ISBN: 9783527336449. DOI: https://doi.org/10.1002/9783527336449.ch1. eprint: https://onlinelibrary.wiley.com/doi/pdf/10.1002/9783527336449.ch1. URL: https://onlinelibrary.wiley.com/doi/abs/10.1002/9783527336449.ch1.

Trenberth, Kevin E., John T. Fasullo, and Jeffrey Kiehl (2009). "Earth's Global Energy Budget". In: *Bulletin of the American Meteorological Society* 90.3, pp. 311 –324. DOI: 10.1175/2008BAMS2634.1. URL: https://journals.ametsoc.org/view/journals/bams/90/3/2008bams2634_1.xml.

Turner, D. D. (2005). "Arctic Mixed-Phase Cloud Properties from AERI Lidar Observations: Algorithm and Results from SHEBA". In: *J. Appl. Meteorol.* 44.4, pp. 427 –444. DOI: 10.1175/JAM2208.1. URL: https://journals.ametsoc.org/view/journals/apme/44/4/jam2208.1.xml.

Twomey, S. (1977). "The Influence of Pollution on the Shortwave Albedo of Clouds". In: *Journal of Atmospheric Sciences* 34.7, pp. 1149 –1152. DOI: 10.1175/1520-

0469(1977)034<1149:TIOPOT>2.0.CO;2. URL: https://journals.ametsoc.org/view/journals/atsc/34/7/1520-0469_1977_034_1149_tiopot_2_0_co_2.xml.

Varga, György et al. (2021). "Saharan dust and giant quartz particle transport towards Iceland". In: *Scientific reports* 11.1, p. 11891. DOI: 10.1038/s41598-021-91481-z.

Vavrus, Stephen J. et al. (2017). "Changes in North American Atmospheric Circulation and Extreme Weather: Influence of Arctic Amplification and Northern Hemisphere Snow Cover". In: *Journal of Climate* 30.11, pp. 4317 –4333. DOI: 10.1175/JCLI-D-16-0762.1. URL: https://journals.ametsoc.org/view/journals/clim/30/11/jcli-d-16-0762.1.xml.

Vincent, Warwick F. (2020). "Arctic Climate Change: Local Impacts, Global Consequences, and Policy Implications". In: *The Palgrave Handbook of Arctic Policy and Politics*. Ed. by Ken S. Coates and Carin Holroyd. Cham: Springer International Publishing, pp. 507–526. ISBN: 978-3-030-20557-7. DOI: 10.1007/978-3-030-20557-7_31. URL: https://doi.org/10.1007/978-3-030-20557-7_31.

Vogelmann, Andrew M et al. (2003). "Observations of large aerosol infrared forcing at the surface". In: *Geophysical research letters* 30.12. DOI: https://doi.org/10.1029/2002GL016829.

Wagner, Robert et al. (2018). "Heterogeneous Ice Nucleation Ability of NaCl and Sea Salt Aerosol Particles at Cirrus Temperatures". In: *J. Geophys. Res.: Atmos.* 123.5, pp. 2841–2860. DOI: https://doi.org/10.1002/2017JD027864. eprint: https://agupubs.onlinelibrary.wiley.com/doi/pdf/10.1002/2017JD027864. URL: https://agupubs.onlinelibrary.wiley.com/doi/abs/10.1002/2017JD027864.

Wake, D. and R. Brown (1991). "Filtration of monodisperse aerosols and polydisperse dusts by porous foam filters". In: *Journal of Aerosol Science* 22, pp. 693–706. DOI: 10.1016/0021-8502(91)90063-N.

Walsh, John E. et al. (2020). "Extreme weather and climate events in northern areas: A review". In: *Earth-Science Reviews* 209, p. 103324. ISSN: 0012-8252. DOI: https://doi.org/10.1016/j.earscirev.2020.103324. URL: https://www.sciencedirect.com/science/article/pii/S0012825220303706.

Wang, Zongliang et al. (2020). "Spatial and Temporal Variations of Arctic Sea Ice From 2002 to 2017". In: *Earth and Space Science* 7.9. e2020EA001278 2020EA001278, e2020EA001278. DOI: https://doi.org/10.1029/2020EA001278. eprint: https://agupubs.onlinelibrary.wiley.com/doi/pdf/10.1029/2020EA001278. URL: https://agupubs.onlinelibrary.wiley.com/doi/abs/10.1029/2020EA001278.

Wegener, Alfred (1911). *Thermodynamik der atmosphäre*. JA Barth.

Weinbruch, Stephan et al. (2012). "Chemical composition and sources of aerosol particles at Zeppelin Mountain (Ny Ålesund, Svalbard): An electron microscopy study". In: *Atmospheric Environment* 49, pp. 142–150. ISSN: 1352-2310. DOI: https://doi.org/10.1016/j.atmosenv.2011.12.008.

Wendisch, Manfred et al. (2017). "Understanding causes and effects of rapid warming in the Arctic". In: *Eos* 98. DOI: 10.1029/2017EO064803. URL: https://doi.org/10.1029/2017EO064803.

Westervelt, D. et al. (2021). "Impact of regional Northern Hemisphere mid-latitude anthropogenic sulfur dioxide emissions on local and remote tropospheric oxidants". In: *Atmospheric Chemistry and Physics* 21, pp. 6799–6810. DOI: 10.5194/ACP-21-6799-2021.

Wild, Martin et al. (2015). "The energy balance over land and oceans: an assessment based on direct observations and CMIP5 climate models". In: *Climate Dynamics* 44, pp. 3393–3429. DOI: 10.1007/s00382-014-2430-z.

Winkler, Peter (1973). "The growth of atmospheric aerosol particles as a function of the relative humidity—II. An improved concept of mixed nuclei". In: *Journal of Aerosol Science* 4.5, pp. 373–387. ISSN: 0021-8502. DOI: https://doi.org/10.1016/0021-8502(73)90027-X.

Wise, Matthew E et al. (2007). "Hygroscopic behavior of NaCl-bearing natural aerosol particles using environmental transmission electron microscopy". In: *Journal of Geophysical Research: Atmospheres* 112.D10. DOI: https://doi.org/10.1029/2006JD007678.

Wunch, Debra et al. (2011). "The Total Carbon Column Observing Network". In: *Philosophical Transactions of the Royal Society A: Mathematical, Physical and Engineering Sciences* 369.1943, pp. 2087–2112. DOI: 10.1098/rsta.2010.0240.

Xu, Li, Lynn M. Russell, and Susannah M. Burrows (2016). "Potential sea salt aerosol sources from frost flowers in the pan-Arctic region". In: *Journal of Geophysical Research: Atmospheres* 121.18, pp. 10,840–10,856. DOI: https://doi.org/10.1002/2015JD024713. URL: https://agupubs.onlinelibrary.wiley.com/doi/abs/10.1002/2015JD024713.

Yang, Yang et al. (2019). "Trends and source apportionment of aerosols in Europe during 1980–2018". In: *Atmospheric Chemistry and Physics*. DOI: 10.5194/acp-2019-778.

Yin, Yan et al. (2002). "Interactions of mineral dust particles and clouds: Effects on precipitation and cloud optical properties". In: *Journal of Geophysical Research: Atmospheres* 107.D23, AAC 19–1–AAC 19–14. DOI: https://doi.org/10.1029/

2001JD001544. URL: https://agupubs.onlinelibrary.wiley.com/doi/abs/10.1029/2001JD001544.

Yu, Qiurun and Yi Huang (2023). "Distributions and Trends of the Aerosol Direct Radiative Effect in the 21st Century: Aerosol and Environmental Contributions". In: *Journal of Geophysical Research: Atmospheres* 128.4, e2022JD037716. DOI: https://doi.org/10.1029/2022JD037716.

Zanatta, M. et al. (2018). "Effects of mixing state on optical and radiative properties of black carbon in the European Arctic". In: *Atmos. Chem. Phys.* 18.19, pp. 14037–14057. DOI: 10.5194/acp-18-14037-2018. URL: https://acp.copernicus.org/articles/18/14037/2018/.

Zender, Charles S., Huisheng Bian, and David Newman (2003). "Mineral Dust Entrainment and Deposition (DEAD) model: Description and 1990s dust climatology". In: *Journal of Geophysical Research: Atmospheres* 108.D14. DOI: https://doi.org/10.1029/2002JD002775. URL: https://agupubs.onlinelibrary.wiley.com/doi/abs/10.1029/2002JD002775.

Zieger, P. et al. (2013). "Effects of relative humidity on aerosol light scattering: results from different European sites". In: *Atmospheric Chemistry and Physics* 13.21, pp. 10609–10631. DOI: 10.5194/acp-13-10609-2013.